The Relationship Between the Density Wave, Molecular Gas and Star Formation in M51

Thesis by

Richard J. Rand

In Partial Fulfillment of the Requirements
for the Degree of
Doctor of Philosophy

California Institute of Technology
Pasadena, California
1991

(Submitted September 21, 1990)

Acknowledgements

It's all Blaise Canzian's fault. He was the one who convinced me to come to Caltech in the first place. So blame him!

After five years in Pasadena, I've been paroled. I've breathed as much smog as I can take, I've cursed too many clueless drivers, and I've eaten as many Dodger Dogs as I can eat. But I will certainly miss softball, volleyball, soccer, P. J. trips, concerts and clubs, beer-making (always followed by beer-drinking), and cheering against the Dodgers.

I would first like to thank my parents, who have always been supportive but have allowed me to find my own way. I'd also like to thank my sister, not least for hosting Christmas in Seattle every other year. Thanks to all my friends from Berkeley days, whom I always look forward to seeing. You still kill me, Bob!

I was Shri Kulkarni's first student (sounds like a good title for my memoirs), but on the whole, I think the experience has been a great success. He did have a tendency at first to get me involved in too many projects at once, but this was only because of his sheer enthusiasm for astronomy and my inexperience in knowing how much I could handle. He did an excellent job of making other astronomers aware of my work by allowing me to go to many conferences, and mentioning my work in his travels. He is always easy to talk to and has an overabundance of ideas. He also invented the term "Nick-ragging."

Thanks to all my fellow students throughout the years. There are far too many to mention them all by name. They seem to fall into three groups: the "old guard" (especially Dave Hough, Rick Edelson, and Alain (Earthquake!) Porter); my contemporaries (especially Steve, Chuck, Blaise, Karl, Debbie, Chris W., Alain, Helen, Chris T., and Josh); and "the younger generation" (including Jose, Tom, Nick, and Wenge). I should also mention my old drinking buddies, Wyman and Doug, and friends from other departments which seem to us to be even more bizarre than ours: Julie, Joel, Chris K., Paolo, and John the Greek. Finally, there is a large group of "non-students" to salute: honorary students Neill (my brewing partner), John Conway (the department will never be the same again), Chris "Sponger" Haniff, and Jeff Kenney; and higher-ups Wal ("the Sultan of Skulk") Sargent, Anneila ("the Shy, Retiring, Woodland Lassie") Sargent, Nick ("Spuds") Scoville, Jeremy Mould, and Tony Readhead. I also thank everyone at Palomar, the library staff, the secretaries, and especially the ever-helpful OVRO guys (how can they always be so cheery at 8:00 a.m.?).

In a recent Caltech thesis, a promising young astronomer from Iowa made some rather speculative predictions for the future of his sub-field. In a similar vain, I began to ponder the future of certain Caltech astronomers. Here, then, are a few predictions, in no particular order:

Nick Scoville will win a Pulitzer Prize for the collected Introduction sections of his papers.

Shri Kulkarni will one day drop all pulsar work, become an extragalactic astronomer, and go out and attempt to determine the Great Attractor–Great Attractor correlation function.

Nick Weir, Tom Herbig, and Jose Navarro will discover the Goon Show and learn the joys of going around the halls speaking and singing in silly voices.

John Conway, after receiving rave reviews for his performance in "The Astronomers," will become a movie star and appear in a science-fiction movie with Leslie Nielsen and Raquel Welch, in which they travel to 3C84 to find out what is really going on there.

Wal Sargent will bring the Major Leagues to England by buying the Dodgers and moving them to Scunthorpe.

Neill Reid, after finishing the Second Sky Survey, will decide that Sussex isn't so bad after all, and will retire to Bexhill-on-Sea.

Rich Rand will prove that M51, apart from being the Rosetta Stone of galaxies, also cures dandruff and removes unsightly stains from your collar.

Abstract

A study is presented of the relationship between the density wave, molecular gas and star formation in the molecule-rich, grand-design spiral galaxy M51.

An interferometric map of CO emission covering most of the disk of M51 at 8" resolution is presented. A narrow, two-arm spiral pattern is seen in the molecular gas. Streaming motions indicating the presence of a density wave can clearly be seen. Giant Molecular Associations (GMAs) of typical mass 3×10^7 $M_\odot$, first reported by Vogel, Kulkarni and Scoville, are seen in abundance along the arms. The virial theorem indicates that these GMAs are roughly gravitationally bound. A few unbound GMAs are also seen between the arms. There is evidence that these interarm GMAs form in a secondary compression of the density wave. Substructure in the GMAs is indicated by their CO spectra, which typically reveal a few discrete velocity components.

Higher (2.5") resolution maps of a small area south of the nucleus of M51 reveal patchy substructure along the southern molecular spiral arm and in the GMAs. The above-mentioned streaming motions are confirmed at this resolution. The one-dimensional velocity dispersion along the arms at this resolution is roughly 10 km s^{-1}. A more careful virial analysis confirms that the on-arm GMAs are bound while the interarm GMAs are unbound. The on-arm GMAs are shown to be stable against galactic tidal forces, while the interarm GMAs are close to the point of marginal

stability. Along the spiral arm in this map, the detailed agreement between CO and Hα luminosity is poor. There are several possible explanations for this.

Two consequences of star formation on the state of the ISM of M51 are discussed. Using the new, 8"-resolution VLA map of 21-cm emission, we find much new evidence in support of the idea of Tilanus and Allen that the HI is predominantly a product of dissociation in star-forming regions. The possibility is suggested that HI emission may be used as an indicator of star formation efficiency in molecule-rich galaxies.

IRAS pointed observations of M51 are used to probe the origins of the infrared emission. Two independent tests indicate that a substantial fraction of the infrared emission originates in a cirrus component, and not due to dust heating by star-forming regions. One consequence of the existence of the cirrus component is that infrared emission cannot be used in a straightforward way to test the hypothesis of the triggering of star formation by a density wave.

A kinematic study of the old-disk stars, and the molecular, neutral and ionized gas is presented. The old-disk stars, since they comprise most of the mass of the galaxy, trace the underlying gravitational perturbation. Long-slit spectroscopy of the absorption lines provides some evidence for radial streaming motions in the massive old-disk population. The amplitude of the motion at 85" from the nucleus is greater than that expected from linear density wave theory. A possible explanation from nonlinear theory is given. Long-slit spectroscopy of the Hα and [NII] lines, along with kinematic information from our CO map and the high-resolution VLA

map of 21-cm emission, clearly reveal streaming motions in the molecular, neutral and ionized gas. These motions are compared with the predictions of nonlinear density wave models.

A quantitative analysis of possible GMA formation mechanisms, which draws on our morphological and kinematic observations of the molecular gas, is presented. Gravitational instability and collisional agglomeration are both viable mechanisms for GMA formation on the arms. The interarm gas is close to the point of marginal stability, and the postulated secondary compression of the density wave may be sufficient to cause either weak instabilities in the gas, or low-level orbit crowding, thereby explaining the unbound interarm GMAs. The relationship between GMA formation and the triggering of star formation is briefly addressed. Problems with the conclusion that the on-arm GMAs are gravitationally bound are discussed. Disruption of bound on-arm GMAs must be rapid since they are confined to narrow spiral arms. Although the arguments are by no means conclusive, the input power of star formation is a plausible mechanism for GMA disruption.

Table of Contents

CHAPTER 1

Introduction and Overview

I. Introduction

What causes spiral structure in galaxies? How different is the spiral structure in the various components of galaxies: the old stars, the young stars, and the cold, warm and hot gas? Can one theory of spiral structure explain all types of spirals, from the grand-design systems like M51 and M83, to the flocculent spirals such as NGC 2841? What is the connection between the large-scale, internal dynamics of a spiral galaxy and star formation?

The idea that density waves are responsible for spiral structure in galaxies was proposed by C. C. Lin and F. H. Shu over 25 years ago (Lin and Shu 1964). Since they first made their hypothesis that galactic spiral structure is a wave phenomenon, the theory of spiral density waves has undergone substantial development. Roberts (1969) and Shu, Milione and Roberts (1973) addressed the problem of how the cold gas in a galaxy would react to a density wave. The results of these nonlinear calculations were that the cold, dissipative gas should react very strongly to the density wave, resulting in high compression factors, disturbed kinematics, and the possibility of large-scale "galactic shocks" and the triggering of star formation. In analogy to the expected stellar response (Lin, Yuan and Shu 1969), it was predicted that the gas should experience a boost in its tangential velocity and a retardation

followed by an increase in its radial velocity as it passed through the density wave compression. These shifts were expected to be larger for the gas than for the stars because the dissipative nature of the gas allows higher compression factors. The gas density peak was predicted to be upstream from the spiral potential minimum. Although such velocity shifts ("streaming motions") in the gas may be difficult to detect in the Milky Way, in an external galaxy the tangential and radial shifts should be evident where the gaseous arms cross the major and minor axes, respectively.

Two important observational searches for the predicted response of gas to a density wave were carried out by Tully (1974) and Visser (1980). Tully's Fabry-Perot study of ionized gas kinematics in M51 revealed some of the predicted velocity shifts on and between the arms, with amplitudes of about 50 km s^{-1}, but could not distinguish between linear and nonlinear models as fits to the data. Visser's study of the neutral gas in M81 revealed strong spiral structure in the HI and kinks in the velocity field all along the arms, indicating velocity shifts of amplitudes up to 20 km s^{-1} as the gas passes through the arms. His work provided much observational support for the predictions of the nonlinear density wave theory.

The nonlinear calculations of the gaseous response assumed that the gas could be treated as a hydrodynamic fluid. However, after these theoretical studies were carried out the field of millimeter wave astronomy flourished, and it was realized that stars form out of dense, self-gravitating clouds of molecular gas. Hence, density wave theory took a new direction when N-body codes were used to simulate the response of a cloud population to a spiral perturbation (Bash and Visser 1981;

Hausman and Roberts 1984; Combes and Gerin 1985; Tomisaka 1986; Kwan and Valdes 1987; Roberts and Stewart 1987; Sundelius *et al.* 1987; Roberts, Adler and Stewart 1990). The important processes of energy dissipation, agglomeration, star formation and supernovae unfortunately have to be handled in a somewhat elementary way in such simulations, not only because of inherent limitations in such methods but also because of our limited understanding of how such processes work. Recently, the effects of the self-gravity of the gas have begun to be included in N-body calculations (Roberts, Lowe and Adler 1990). The possible importance of self-gravity in the gaseous reaction to a density wave was stressed at least as long ago as 1973 (Shu, Milione and Roberts 1973).

The important result from these simulations was that strong spiral structure should exist in the cloudy components of galaxies. Specific predictions for the kinematics of the cloud system as it responds to the density wave were made by Hausman and Roberts (1984) and Roberts and Stewart (1987). A key observational result came from Vogel, Kulkarni and Scoville (1987, hereafter VKS), who mapped the NW quadrant of M51 at 8" resolution with the Millimeter Interferometer of the Owens Valley Radio Observatory (OVRO). They demonstrated the existence of strong, narrow molecular spiral arms in M51, and a velocity shift along the entire extent of the detected NW arm in the sense predicted by the density wave theory. The amplitude of the shift they found was 60-100 km s^{-1} – much larger than predicted by the models. Streaming motions in the molecular gas along the major axis of M51 were first reported by Rydbeck, Hjalmarson and Rydbeck (1985).

Another very important observational and theoretical aspect of the characteristics of the gas cloud population is the mass spectrum, typical cloud size, and the nature of the most massive structures. An observational understanding of these aspects can help lead to a theoretical understanding of how self-gravitating molecular clouds form, and the possible role of density waves in their formation. The Galactic GMC mass spectrum has the form N(M) α $M^{-1.6}$, and the typical GMC has a mass of 4×10^5 $M_\odot$ and a diameter of 40 pc (Scoville and Sanders 1987). HI superclouds of mass 10^7 $M_\odot$ have been observed in the spiral arms of many nearby spirals (summarized in Elmegreen 1987a). More recently, VKS reported the discovery of massive (3×10^7 $M_\odot$) concentrations of molecular gas along the NW arm of M51. These concentrations were termed Giant Molecular Associations (GMAs) by VKS. The two currently popular theories for the formation of GMCs and more massive structures are *a)* agglomeration by cloud collisions, and *b)* gravitational instabilities. Of the N-body simulations mentioned above, Kwan and Valdes (1983, 1987) have concentrated on determining whether the Galactic GMC mass spectrum can be reproduced through the process of agglomeration of initially small clouds as they pass through the density wave compression. They have been able to reproduce the observed GMC mass spectrum in this way. On the other hand, Elmegreen (1989) has shown that the mass spectrum can be explained if the GMCs form by gravitational instability out of a medium consisting of diffuse clouds. For the formation of the more massive superclouds and GMAs, the same two mechanisms have been invoked. Much analytic work showing how such large structures are expected to

form through gravitational instability has been carried out in recent years (Jog and Solomon 1984; Balbus and Cowie 1985; Elmegreen 1987b; Balbus 1990). N-body simulations with the effects of self-gravity included have also been able to reproduce structures of such high mass (Roberts, Lowe and Adler 1990). An important issue is whether these massive structures are gravitationally bound, as the GMCs appear to be (*e.g.,* Scoville and Sanders 1987). Another uncertainty in both pictures is that, in order to maintain a steady state, the gas must be returned to its initial state once it leaves the compressed region. In other words, if large concentrations exist only on the arms, they must be destroyed before they drift into the inter-arm regions. Diverging orbits (Roberts, Lowe and Adler 1990), energy input by star formation (Balbus and Cowie 1985; Elmegreen 1990) and galactic shear forces (Elmegreen 1987c) may all be important for "reversing" the effects of the density wave compression on the molecular gas and thus maintaining a steady state.

Density waves, then, may alter the state of the molecular gas, but how might they relate to star formation? Evidence has been brought forth recently that star formation is more efficient on the arms of spirals than off the arms. Hα images are generally used as tracers of the massive star formation rate, while CO observations are used to estimate the molecular gas surface density. One potential uncertainty is of course the conversion between CO luminosity and the mass of molecular hydrogen. However, for these kinds of studies, the only necessary assumption is that there are no large variations in the conversion factor within a galaxy. VKS and

Lord and Young (1990) have found that the star formation efficiency (SFE), assumed to be proportional to the ratio of the Hα luminosity to the CO luminosity, is enhanced on the arms of M51, implying that star formation is triggered when the gas is compressed. Such an effect has also been seen in NGC 6946 by Tacconi (1990). These results are seemingly in contradiction with the conclusions of Elmegreen and Elmegreen (1986), who found very little correlation between the global SFE and the large-scale coherence of the spiral pattern for a large sample of spiral galaxies. Their results suggested that density waves have little effect on the process of star formation. However, VKS showed that although the density wave is an efficient *local* star formation trigger, the *global* enhancement in the SFE due to density wave triggering should be modest enough so as to be undetectable in the Elmegreens' data.

It has been proposed that in our Galaxy, massive star formation occurs at the interfaces of colliding clouds (Scoville, Sanders and Clemens 1986). If so, then the star formation rate should depend on the frequency of collisions, which goes as the square of the number density of clouds. Therefore, the SFE should depend on the gas density, and should be higher on the arms of a spiral galaxy than between them, as observed in M51 and NGC 6946. Alternatively, gas is expected to be more gravitationally unstable and to collapse faster as it is compressed by the density wave, and thus, if star formation happens by a process of gravitational collapse, it may be more efficient on the arms (see Elmegreen 1990). The potential importance of the stability of the gas for star formation has been addressed in a

recent observational study by Kennicutt (1989), who has found evidence that there is a threshold in the gas surface density above which star formation is relatively efficient, and below which there is very little star formation. The threshold surface density is very well predicted by a simple gas instability model. The important lesson from this discussion is that a critical step toward understanding the global processes and regulation of star formation in galaxies is to understand how galactic dynamics, specifically spiral density waves in the case of the present study, affect the state of the star-forming gas.

Another important issue is how star formation, in turn, affects the state of the ISM. It was mentioned above how the input power from star formation may work to maintain a steady state in the ISM. Star formation has other consequences for the state of the gas besides the production of HII regions and the possible destruction of clouds. In M83 (Allen, Atherton and Tilanus 1986) and M51 (Tilanus and Allen 1989), from Westerbork 21-cm maps, it was observed that the spiral ridges of HI are not coincident with the dust lanes but are offset downstream. The HII region arms are also offset downstream from the dust lanes in these galaxies (Allen, Atherton and Tilanus 1986; VKS). These spatial relationships led Allen, Atherton and Tilanus (1986) and Tilanus and Allen (1989) to conclude that the HI is predominantly a product of dissociation of molecular gas in star forming regions in these molecule-rich galaxies. This conclusion was in contrast to some previous ideas which assumed the molecular clouds formed from neutral gas in the density wave compression. In galaxies with an ISM dominated by molecules, though, this does not appear to be

the case. In M51, only about 10% of the molecular gas is dissociated into HI on the arms (Tilanus and Allen 1989). Hence, the gas remains predominantly molecular, even in the dissociation regions.

Recent star formation also gives rise to infrared emission. It is therefore possible in theory to use infrared emission to independently check the theory of star formation triggered by a density wave. However, one must understand the origins of the infrared emission before carrying out such a check. In particular, there is mounting evidence that in the Milky Way and other nearby galaxies, there are two important components which contribute to the mid- and far-infrared emission. The first is emission from warm dust in star-forming regions while the second is emission from dust which is more uniformly distributed and is heated by the interstellar radiation field. The latter component has come to be known as "cirrus" (Low *et al.* 1984). The cirrus component is potentially separable from the infrared emission from star-forming regions by its more uniform spatial distribution. Its presence can also be inferred by comparing the observed level of infrared emission in a galaxy to that expected if the emission arose entirely from its star-forming regions.

II. Overview

This thesis is an attempt to understand the relationship between density waves, molecular gas and star formation in the grand-design spiral galaxy M51. General properties of this galaxy are listed in Table 1. M51, the first galaxy in which spiral structure was found (Parsons [Third Earl of Rosse] 1850), was chosen for this study because of its proximity, nearly face-on aspect, molecule-rich ISM, and strong,

coherent, two-armed spiral structure. Specifically, the goals of this thesis are to observationally characterize the density wave in M51 and the response of the various components to the wave, to understand the morphology and distribution of the various components of the ISM (especially the molecular gas) and the distribution of newly-formed stars, to apply current theories to relate the observed state of the ISM and the process of star formation to the influences of the density wave, and to examine how star formation in turn alters the state of the ISM. Each chapter is a paper. The first has been published (Rand and Kulkarni 1990), while the second and fourth will soon be submitted to the Astrophysical Journal, and the third has recently been submitted to the same journal. For a more general observational review of all aspects of the ISM of M51, see Rand and Tilanus (1990).

The first paper presents the initial results from the complete mosaic map at 8" resolution made with the Millimeter Interferometer at OVRO. This mapping project was initiated by S. Vogel (VKS). The main goals of the paper are to present and discuss the full mosaic map consisting of 30 one-arcminute fields and to further elucidate the nature of the GMAs. Are they gravitationally bound? Are they stable against galactic tidal forces? Are they confined to the arms? Do any exist between the arms? How might they form? Is there any evidence for substructure as seen in Galactic GMCs? How might the GMAs be destroyed? A further goal is to provide more evidence for density-wave induced streaming motions.

The 2.5" resolution mapping project that led to the second paper was largely motivated by some of the results from the first paper. Many of the GMAs at 8"

resolution were unresolved, giving possible cause for concern as to whether reliable virial masses could be estimated. Also, the CO spectra of the GMAs indicated that they generally consist of a few velocity components. The reason to use higher resolution, therefore, was to resolve some of the GMAs that were unresolved at 8" resolution so that more accurate virial masses could be calculated, and to look for spatial substructure in the GMAs. Two fields from the mosaic were mapped at this resolution. The fields include the region where the inner molecular spiral arm crosses the southern half of the major axis. Hence, these high-resolution observations can also be used to estimate more accurately the gradient of the tangential streaming velocity across the arm.

The third paper addresses two consequences of star formation for the ISM of M51. First, a new high-resolution VLA map of 21-cm emission by Rots *et al.* (1990) is used to determine whether the spiral and small-scale structure in the neutral gas supports the idea of Tilanus and Allen (1989) that the HI is largely a product of dissociation in star-forming regions. Second, *IRAS* pointed observations of M51 are used to probe the origins of the infrared emission. In particular, we compute the global ratio of far-infrared emission to thermal radio emission and compare the *IRAS* maps with optical images to address the question of whether all of the emission detected by *IRAS* arises from star-forming regions, or whether there is a substantial contribution from a cirrus component.

Finally, the fourth paper presents a detailed analysis of the reaction of the various components of M51 to the spiral density wave. We present a velocity profile

of the old disk stars along the minor axis and discuss the kinematics of the massive old stellar disk, which defines the underlying gravitational potential. The velocity profile is compared with the predictions of linear and nonlinear density wave theory. We present observations of the kinematics of the ionized, neutral and molecular gas along the major and minor axes, and compare the response of each of these components with each other and with the predictions of nonlinear density wave theory. We then use our kinematic results to carry out an analysis of GMA formation on and off the arms. We first determine whether the on- and off-arm gas should be gravitationally unstable, and estimate the expected characteristic masses. Timescales for GMA formation on and off the arms by gravitational instability and collisional agglomeration are then computed. These are compared with the time available for GMA formation, which may be limited by the rate of destruction by shear or the time for passage of the gas through the arm and interarm regions. GMA disruption is considered in more depth here than in the first paper.

To conclude this introduction, it is emphasized that M51 was chosen for this study because of its strong, coherent two-armed spiral structure, among other reasons. It is perhaps the best observational laboratory we have for studying density waves. The ultimate goal of such studies, of course, is to understand the process of star formation in spiral galaxies of all types. Some of the results discussed here may not be seen in other spirals with weaker or qualitatively different spiral structure. However, this would not necessarily imply that the same processes are not occurring at a lower level in other spirals. For instance, the large-scale spatial

offsets between the spiral patterns of the various tracers may not be perceptible in many galaxies with less coherent spiral structure. Other effects, such as the existence of GMAs, may require a strong compression so that the agglomeration or instability process has sufficient time to operate. Hence, many spirals may not show gaseous structures as massive as the GMAs of M51. The flocculent spirals may not have density waves at all – star formation may be stochastic in such galaxies (Gerola and Seiden 1978). Finally, many S0s are found to have star formation, with global efficiencies comparable to late-type spirals (Thronson *et al.* 1989), implying that density waves are not necessary for star formation. Therefore, we are only beginning to understand what causes and regulates star formation in galaxies. This thesis is an attempt to show how one physical process, the spiral density wave, affects the distribution of molecular gas and and how it relates to star formation.

Table 1. M51: General properties

R.A. (1950.0)[a]	$13^h27^m46^s.327$	Ford *et al.* (1985)
Decl. (1950.0)[a]	$47°27'10''.25$	Ford *et al.* (1985)
Distance	9.6 Mpc	Sandage and Tammann (1975)
Heliocentric Systemic velocity	$464\,km\,s^{-1}$	Tully (1974b)
Holmberg diameter	$14'.2 \times 9'.5$	Holmberg (1958)
P.A. major axis	170°	Tully (1974b)
Inclination angle	20°	Tully (1974b)
M_{HI}	5×10^9 $M_\odot$	Rots (1980)
M_{H2}	9×10^9 $M_\odot$	Scoville and Young (1983)
L_B	3.8×10^{10} $L_\odot$	de Vaucouleurs *et al.* (1976)
L_{FIR} (NGC 5194)	2×10^{10} $L_\odot$	Rice *et al.* (1988)
L_X (0.2–4 keV)	3×10^{40} erg s^{-1}	Palumbo *et al.* (1985)
S_{20cm}	1500 mJy	Hummel (1980)
$L_{H\alpha}$ (NGC 5194)	3.8×10^{41} erg s^{-1}	Kennicutt and Kent (1983)

[a]nuclear radio-continuum source

References

Allen, R. J., Atherton, P. D., and Tilanus, R. P. J. 1986, *Nature*, **319**, 296.

Balbus, S. A. 1990, in *The Interstellar Medium in Galaxies*, eds. H. A. Thronson and J. M. Shull (Dordrecht:Kluwer), p. 305.

Balbus, S. A., and Cowie, L. L. 1985, *Ap. J.*, **297**, 61.

Bash, F. N., and Visser, H. C. D. 1981, *Ap. J.*, **247**, 488.

Combes, F., and Gerin, M. 1985, *Astr. Ap.*, **150**, 85.

Elmegreen, B. G., and Elmegreen, D. M. 1986, *Ap. J*, **311**, 554.

Elmegreen, B. G. 1987a in *I.A.U. Symposium No. 115, Star Forming Regions*, ed. M. Peimbert and J. Jugaku (Dordrecht: Reidel), p. 457.

Elmegreen, B. G. 1987b, *Ap. J.*, **312**, 626.

Elmegreen, B. G. 1987c in *Galactic and Extragalactic Star Formation* ed. R. E. Pudritz and M. Fich (Kluwer), p. 215.

Elmegreen, B. G. 1989, *Ap. J.*, **347**, 859.

Elmegreen, B. G. 1990, in *The Evolution of the Interstellar Medium*, ed. L. Blitz, Astronomical Society of the Pacific Publishers, in press.

Gerola, H., and Seiden, P. E. 1978, *Ap. J.*, **223**, 129.

Hausman, M.A., and Roberts, W. W. 1984, *Ap. J.*, **282**, 106.

Jog, C. J., and Solomon, P. M. 1984, *Ap. J.*, **276**, 127.

Kennicutt, R. C. 1989, *Ap. J.*, **344**, 685.

Kwan, J., and Valdes, F. 1983, *Ap. J.*, **271**, 604.

Kwan, J., and Valdes, F. 1987, *Ap. J.*, **315**, 92.

Lin, C. C. and Shu, F. H. 1964, *Ap. J*, **140**, 646.

Lin, C. C., Yuan, C., and Shu, F. H. 1969, *Ap. J*, **155**, 721.

Lord, S. D., and Young, J. S. 1990, *Ap. J.*, **356**, 135.

Low, F. J. *et al.* 1984, *Ap. J. (Letters)*, **278**, L19.

Parsons, W. [Third Earl of Rosse] 1850, The Scientific Papers of William Parsons, Third Earl of Rosse, 1800-1867, ed. C. Parsons (London: Humphries & Co.), p 109.

Rand, R. J., and Kulkarni, S. R. 1990, *Ap. J. (Letters)*, **349**, L43.

Rand, R. J. and Tilanus, R. P. J. 1990, in *The Interstellar Medium in Galaxies*, eds. H. A. Thronson and J. M. Shull (Dordrecht:Kluwer), p. 525.

Roberts, W. W. 1969, *Ap. J.*, **158**, 123.

Roberts, W. W., Adler, D. S., and Stewart, G. R. 1988, in *Applied Mathematics, Fluid Mechanics, Astrophysics*, eds. D. J. Benney, F. H. Shu, and C. Yuan (Singapore: World Scientific), p. 373.

Roberts, W. W. and Stewart, G. R. 1987, *Ap. J.*, **314**, 10.

Rots, A. H., Bosma, A., van der Hulst, J. M., Athanassoula, E., and Crane, P. C. 1990, *A. J.*, **100**, 387.

Rydbeck, G., Hjalmarson, A. and Rydbeck, O. E. H. 1985, *Astr. Ap.*, **144**, 282.

Scoville, N. Z., and Sanders, D. B. 1987, in *Interstellar Processes*, ed. D. Hollenbach and A. Thronson (Dordrecht: Reidel), p. 21.

Scoville, N.Z., Sanders, D.B. and Clemens, D.P. 1986, *Ap. J. (Letters)*, **310**, L77.

Shu, F. H., Milione, V. and Roberts, W. W. 1973, *Ap. J.*, **183**, 819.

Sundelius, B. J., Thomasson, M., Valtonen, M. J., and Byrd, G. G. 1987, *Astr. Ap.*, **174**, 67.

Tacconi, L. J. 1990, in *Submillimetre Astronomy*, ed. G. D. Watt and A. S. Webster, (Dordrecht: Kluwer), p. 243.

Thronson, H. A. *et al.* 1989, *Ap. J.*, **344**, 747.

Tilanus, R. P. J., and Allen, R. J. 1989, *Ap. J. (Letters)*, **339**, L57.

Tomisaka, K. 1986, *Pub. A. S. Japan.*, **38**, 95.

Tully, R. B. 1974, *Ap. J. Suppl.*, **27**, 449.

Visser, H. C. D. 1980, *Astr. Ap.*, **88**, 159.

Vogel, S. N., Kulkarni, S. R., and Scoville, N. Z. 1988, *Nature*, **334**, 402 (VKS).

CHAPTER 2

M51: Molecular Spiral Arms, GMAs, and Superclouds

Abstract

We present an aperture synthesis image of the prototypical grand-design spiral galaxy M51 in the CO (1–0) line made with the Owens Valley Millimeter Interferometer. The image is a mosaic of 30 one-arcminute fields. Narrow (10" – 20") spiral arms are seen which are coincident with the optical dust lanes and non-thermal radio emission, but are offset from the ridges of Hα and thermal radio emission. There are many dense concentrations of emission, termed Giant Molecular Associations (GMAs), both along and between the arms. The GMAs have masses of 10^7 to 6×10^7 $M_\odot$, and most of the on-arm ones appear to be bound. They consist of several spectral components, termed Molecular Superclouds, which also appear to be bound. The interarm GMAs are unbound and are probably due to a secondary compression of the density wave. Streaming motions in the GMAs are consistent with density wave theory.

Subject headings: Galaxies: individual (M51) – Galaxies: interstellar matter – Galaxies: structure – Interferometry

I. Introduction

While it is generally acknowledged that density waves are responsible for galactic spiral structure, their role in triggering coherent star formation remains obscure. Direct evidence for the existence of density waves has been provided by the detection of streaming motions in the grand-design spiral galaxies M51 (Tully 1974b; Rydbeck *et al.* 1985) and M81 (Visser 1980). On the other hand, the observed spiral structure – even in grand-design systems such as M51 – can be reproduced by models of stochastic, self-propagating star formation (Seiden and Gerola 1979). Furthermore, Elmegreen and Elmegreen (1986) found that the overall star formation efficiency (SFE) is only weakly correlated with the large-scale coherence of the spiral arms, suggesting that density waves have little to do with star formation. Finally, Elmegreen (1987a) claims that the narrower and better defined arms seen in the blue light of spirals as compared to the red can be explained by higher compression of the molecular gas by the density wave relative to the old disk stars, with the massive star formation rate depending merely linearly on the molecular gas mass.

To investigate the relationship between density waves and star formation, we have undertaken a major program of radio synthesis mapping of M51 (NGC 5194) in the 2.6 mm CO (1–0) transition with the Owens Valley Millimeter Interferometer. Initial results for 8 one-arcminute fields revealed narrow molecular spiral arms and demonstrated the existence of spatially resolved velocity shifts across the arms in the NW quadrant of the galaxy (Vogel, Kulkarni, and Scoville 1988, hereafter VKS)

in the sense predicted by density wave theory. The SFE was found to be higher in the arms than between the arms (VKS; Rand and Kulkarni 1989).

In this *Letter*, we present our interferometric mosaic map for 30 fields covering most of M51 and discuss the implications of this map for the role of density waves in star formation.

II. Observations

The Millimeter Wave Interferometer of the Owens Valley Radio Observatory was used in the years 1986 through 1989 to map M51 in the CO (1–0) line. The three 10.4 m dishes are equipped with SIS receivers, cryogenically cooled to $\sim$ 4 K. Two filterbanks with 32 1-MHz and 32 5-MHz channels provided resolutions of 2.6 km s^{-1} and 13 km s^{-1}.

A total of 30 positions in M51 were observed in two array configurations, and each 12 hr track was shared between two positions. The synthesized beam is about 9" $\times$ 7" (PA=0°), corresponding to a linear resolution of 500 $\times$ 350 pc, assuming a distance of 9.6 Mpc (Sandage and Tammann 1975). The primary beam is 65" (HPBW). Phase calibration was based on observations of the quasar 1418+546 every 15 min. Mars, Uranus, 3C 84 and 3C 273 were used to determine the flux scale, giving an uncertainty of $\sim$ 20%. The mapping was carried out using standard NRAO AIPS software.

The first eight positions were mapped in 1986-87 (VKS) and the remaining 22 by us in 1987-88 and 1988-89. The 30 maps were combined into a single data cube through a simple mosaicing procedure which corrects for primary beam attenuation.

III. Features of the Mosaic Map

The mosaic is overlaid on an Hα CCD image of M51 in Figure 1*a* (Plate 1) and on a red-continuum image in Figure 1*b* (Plate 2).

The most striking feature of the mosaic are the narrow spiral arms, especially within about 100" of the nucleus. Two arms of width 10" – 20" can be traced for about 270° of azimuth. The emission breaks up into discrete features along these arms. Disconnected emission features delineate spiral arms further from the nucleus, and are also seen between the main arms. We detect typically 25 – 35% of the flux contained within a single-dish beam at a given position (Lord and Young 1989).

The molecular arms show excellent correspondence with the optical dust lanes. There is also a close coincidence between the molecular arms and the ridges of non-thermal radio emission (Tilanus *et al.* 1988). The arms are offset by 5"–10" to the inside of the Hα ridge in the inner regions. The offset is larger in the outer arms (10"–20"). Using the pitch angle, rotation curve and pattern speed from Tully (1974b), the implied delay between the peak compression of the molecular gas and the peak of massive star formation is $\sim 10^7$ years. Although this offset could be due to optical extinction, we note that a similar offset is seen between the molecular arms and the thermal radio emission arms (Tilanus and Allen 1989).

IV. Discussion

The molecular emission shows dense concentrations of gas both on and between the arms. For the determination of the masses of these concentrations, we first estimated the total flux in each. Using the Galactic conversion factor of integrated CO flux to molecular column density, $\alpha = 3 \times 10^{20}$ mol cm^{-2} (K km s^{-1})$^{-1}$ (*cf.* Scoville and Sanders 1987), we derive masses of $10^7 - 6 \times 10^7$ $M_\odot$ for the on-arm concentrations, and $10^7 - 4 \times 10^7$ $M_\odot$ for the interarm ones (a factor of 1.36 for the helium content is included). Sources of error in an individual mass estimate are the uncertainty in the distance to M51 (the dominant source since the mass depends on the square of the distance), measurement error in the exact extent of the concentration, the uncertainty in the above conversion ratio, and the error in our amplitude calibration. Assuming a distance uncertainty of 20%, the resulting fractional error on the mass is about $\pm 50\%$ for all concentrations.

These concentrations have been termed Giant Molecular Associations by VKS, to reflect the facts that *a)* the on-arm concentrations can only survive for a small fraction of a galactic rotation as evidenced by the widths of the arms, and *b)* their masses are more than an order of magnitude greater than those of typical Galactic GMCs ($10^5 - 10^6$ $M_\odot$). We identify 26 GMAs in our map: 20 on the arms, and 6 between the arms (Table 1). The 6 interarm GMAs represent the first such detections.

a) The Nature of the On-arm GMAs

To determine whether the GMAs are gravitationally bound, we have calculated the virial mass of each GMA from the velocity dispersion at the peak of its flux, σ, (in km s^{-1}) and its estimated diameter, D, (FWZI, in pc), according to the formula $M_{vir} = 525 D\sigma^2$ $M_\odot$. The GMA spectra are dominated by a few (1 to 5) distinct velocity components, hereafter referred to as "spectral components." In cases of multiple component GMAs in which a Gaussian fit is clearly inappropriate, the dispersion of the component velocities was used to estimate the virial mass. Sources of error in this determination are errors in σ and D (determined directly from the data for each GMA) and the uncertainty in the distance to M51. The range of fractional errors for the virial masses is about $30 - 100\%$, with the first of the above sources dominating the error. A majority (16) of the GMAs are unresolved – hence only upper limits on their virial masses can be calculated. The resulting virial masses (M_{Vir}) and CO-flux-based masses (M_{CO}) are shown in Table I. The interarm GMAs do not show good evidence of being virially bound. In contrast, many on-arm GMAs appear to be bound, especially within 5 kpc from the nucleus.

It is possible that the good agreement between M_{Vir} and M_{CO} is fortuitous and that the GMAs are just random superpositions of a few large GMCs. To test this possibility we simulated a random distribution of a population of large GMCs, with a size spectrum of $N(D)$ α $D^{-2.32}, 40$ pc $\leq D \leq$ 160 pc. The exponent in the above expression is the Galactic value (Scoville and Sanders 1987). GMCs were drawn from this parent population and randomly placed on a two-dimensional grid. Several simulations were run with varying mean column density. We then "mapped"

these simulations using our *uv*-coverage. The total area simulated was about half the area we have observed. In order for the 6 brightest simulated concentrations to reproduce the mean flux of the 6 largest GMAs, a surface density of $> 10^{23}$ mol cm^{-2} is needed, which is much too high to be consistent with both our observed mean on-arm value (5×10^{21} mol cm^{-2}) and the on-arm value (6×10^{21} mol cm^{-2}) in the single-dish observations of Lord and Young (1989).

The simulations were checked for their sensitivity to the input assumptions. Doubling the endpoints of the mass spectrum, to 80 and 320 pc, produced a clumpier structure but reduced the required column density only by a factor of 2. Increasing the exponent of the size spectrum to 2.82 also had an insignificant effect on our results. Thus our simulations demonstrate that random superposition cannot produce the observed on-arm GMAs, giving more support to the idea that most of them are bound.

If the on-arm GMAs are bound, we must then ask whether they are stable entities. For example, the mean density, $\overline{n}$, of large clouds must exceed $n_t = A\Omega/G$ to be stable against tidal forces in the galactic disk. From the observed flat rotation curve (*e.g.*, Tully 1974a), we find $A = 105/R$ km s^{-1} kpc^{-1}. From Table I, the interarm GMAs are therefore generally unstable. Four on-arm GMAs are stable, two are clearly unstable while the remaining 14 have only upper limits on the mean density. However, as Elmegreen (1987b) has pointed out, the tangential streaming motion induced by a density wave results in essentially solid-body rotation on the arms and therefore a much smaller Oort's constant A. Indeed, from the amplitude

of the streaming motions we have detected (see § IVb), one finds that in the spiral arms at 3 kpc from the nucleus, A is a factor of 2 smaller than the above value. Thus, the minimum density for tidal stability is reduced on the arms, and therefore the on-arm GMAs are probably not tidally unstable.

We can also check whether the individual on-arm GMA "spectral components" are themselves virially bound. In Figure 2, M_{Vir} and M_{CO} are compared for components which are well isolated in the spectra. Given the large uncertainty in this type of comparison, the plot shows good evidence that these components, with average mass $\sim 10^7$ $M_\odot$, are in fact gravitationally bound. We therefore call these components "molecular superclouds," in analogy to the HI superclouds of comparable mass seen in some spirals (Elmegreen 1987b). Although "normal" ($10^5 - 10^6$ $M_\odot$) GMCs have been found embedded in these HI superclouds (*e.g.,* Blitz 1985), gravitationally bound 10^7 $M_\odot$ molecular clouds have not been seen before in spiral galaxies.

How do these superclouds form? One possible mechanism is agglomeration through cloud-cloud collisions, which has received observational support in our own Galaxy (*e.g.,* Scoville *et al.* 1986). However, it is not clear that the formation of bound clouds with masses as large as 10^7 $M_\odot$ can be explained by this mechanism. Given the high molecular gas density in the disk of M51 (Lord 1987) combined with the strong density wave (Tully 1974b), one would expect a higher growth rate for the assemblages, possibly leading to the formation of many 10^7 $M_\odot$ clouds. Alternatively, such high-mass clouds are expected to form directly as a result of

gravitational instability, especially in the spiral arms (Elmegreen 1987c). This instability is enhanced in the arms because the tangential streaming motions of the gas tend to offset the stabilizing shear in the galactic disk, as discussed above. A hybrid of these two scenarios is also possible (Elmegreen 1987c).

How do the GMAs form and what confines them to the spiral arms? The formation of GMAs could be analogous to the formation of molecular superclouds: collisions of superclouds, direct formation through gravitational instability, or a hybrid of the two mechanisms. The confinement to the spiral arms implies that the GMAs are short-lived, with a lifetime of roughly 3×10^7 years. One possibility is that star formation within the constituent superclouds provides enough energy to disrupt the GMAs. The gravitational binding energy of a typical GMA is 2×10^{53} ergs. A cluster of 3000 OB stars, which is necessary to produce a typical supergiant HII region, can therefore easily provide enough energy to disrupt a GMA (or a supercloud). However, the coupling of the energy output to the bulk motion of the gas is a large uncertainty. Another possibility is that the GMAs and superclouds are only stable against tidal forces within the spiral arm, and are disrupted upon leaving the arm. As discussed above there is some marginal evidence that this could be the case.

b) Streaming Motions in On-arm GMAs

Simulations of the response of molecular clouds to a spiral density wave predict that the spiral potential disturbs the basic circular rotation by causing steep velocity gradients both parallel and perpendicular to spiral equipotentials near the

narrow region of spiral phase where the gas is highly compressed (see Figure 3 of Roberts and Stewart 1987). Observationally, these velocity gradients translate into a boost in the tangential velocity in the direction of rotation and a shift in radial velocity toward the nucleus. These disturbances to the clouds' orbits lead to longer residence times of the clouds in the region of the spiral potential minimum ("orbit crowding") and are the primary reason for molecular spiral structure in these simulations.

One of the most important results of VKS was the detection of such tangential and radial "streaming motions" in two GMAs near the major and minor axes, respectively, in the directions predicted by the models. With the now more complete data, streaming motions are detected in 4 additional complexes. In each case, the velocity shift is in the direction predicted by density wave theory. We defer further discussion of streaming motions to a future paper on the gas-dynamics of M51.

c) The Nature of the Interarm GMAs

The interarm GMAs are rather weak, but all are detected at $\geq 7\sigma$ in more than one field. They have a mean mass of 2×10^7 $M_\odot$ (half the mean on-arm GMA mass) and show typically 3 or 4 distinct spectral components with a mean mass of 6×10^6 $M_\odot$. Evidence was presented above that these GMAs are probably not bound.

The existence of interarm GMAs raises the question of whether they have a dynamical origin, or are perhaps just random superpositions of a few large GMCs.

Repeating our simulations with the same spectrum of very large GMCs ranging from 80 to 320 pc, the surface density required for the 6 brightest simulated concentrations to reproduce the mean flux of the 6 interarm GMAs is 2×10^{22} mol cm^{-2}. This value is much greater than the typical observed interarm value, which we estimate from Lord (1987) to be 5×10^{21} mol cm^{-2} at about 1' from the nucleus. The interarm GMAs in M51 must therefore have a dynamical origin, possibly analogous to the on-arm GMAs.

One possibility is that they are formed by secondary compressions of the density wave. The gas-dynamical numerical calculations of Shu et al. (1973) showed that high harmonic resonances of the epicyclic frequency and the frequency with which the wave passes through the gas can lead to secondary spiral features over narrow ranges of radii. The self-gravity of the gas should enhance this process. Secondary compressions have been speculated to be present in M51 (Tully 1974b; Rydbeck *et al.*, 1985) and M81 (Visser 1980).

The best observational test of this idea is to look for the streaming motions predicted by density wave theory in the interarm GMAs. The one interarm GMA near the minor axis (I6 in Figure 1*b*) does indeed show the expected radial velocity shift (15 km s^{-1}) toward the nucleus, in accordance with the density wave prediction. Also in support of this interpretation is the fact that we see faint, narrow strings of HII regions giving the appearance of coherent spiral features (Figure 1*a*) in the NE and SW interarm regions near concentrations of interarm GMAs, indicating a large-scale, but relatively low-level, star forming event. All the evidence

therefore indicates that these GMAs are indeed formed by secondary compressions of the density wave. The 6×10^6 $M_\odot$ spectral components are then likely to be smaller versions of the molecular superclouds in the main arms.

V. Conclusions

Our high-resolution interferometric map of the CO emission in M51 shows two narrow spiral arms with many bright concentrations of emission (GMAs). The GMAs have masses of $10^7 - 6 \times 10^7$ $M_\odot$. The interarm GMAs are unbound whereas many of the on-arm GMAs appear to be bound. Our simulations show that the GMAs cannot be a simple random superposition of large GMCs, but instead must have a dynamical origin.

The GMAs are composed of a small number of distinct components (superclouds) with a mean mass of 10^7 $M_\odot$, which show good evidence of being virially bound. These superclouds may be the extreme cases of agglomeration by cloud-cloud collisions, or they may form directly as a result of enhanced gravitational instability in the arms. An attractive feature of the former mechanism is that it can explain the higher SFE on the arms in M51, whereas the situation is less clear for the latter mechanism.

GMAs may also form through instabilities or collisions of superclouds. Because of the modification of the local rotation curve by the tangential streaming motions, they are stable against galactic tidal forces while in the arms, and may

become unstable as they leave the arms. Alternatively, they may be disrupted by the energy output of the newly formed stars.

Streaming motions in on-arm GMAs are consistent with the predictions of density wave theory. The discovery of streaming motions in interarm GMAs provides strong evidence for secondary compressions of the density wave.

These results demonstrate the need for new simulations of systems like M51 where the spiral potential may be more powerful than just a linear perturbation on the axisymmetric potential, and where gaseous compression is high enough so that the self-gravity of the gas may significantly affect the overall disk dynamics.

Acknowledgements

We thank N. Z. Scoville, S. N. Vogel, and J. D. Kenney for helpful comments on the manuscript, and J. J. Hester for help with the optical observations and reduction. The Owens Valley Millimeter Interferometer is supported by NSF grant AST 97-14405.

Table 1. GMA Properties

GMA	R.A. Offset from Nucleus (arcmin)	Dec. Offset from Nucleus (arcmin)	Distance from Nucleus (kpc)	M_{CO} (10^7 $M_\odot$)	M_{Vir} (10^7 $M_\odot$)	$\overline{n}/n_t$
A1	−0.18	0.88	3	4.6	< 11	> 0.6
A2	−0.65	0.82	3	5.4	< 5.1	> 0.8
A3	−1.45	−0.08	4	1.1	0.7	1.0
A4	−0.42	−0.62	2	5.2	< 5.1	> 0.3
A5	−1.90	−0.42	6	2.3	< 1.5	> 1.3
A6	−1.62	−1.32	6	3.1	1.4	1.9
A7	−1.62	−1.78	7	3.5	3.4	1.6
A8	0.28	−1.02	3	6.2	< 4.1	> 0.9
A9	0.50	−1.02	3	2.6	< 2.2	> 0.4
A10	1.08	−0.68	3.5	3.7	3.6	0.2
A11	0.82	−0.48	2.5	2.7	< 3.0	> 0.3
A12	1.32	1.02	5	2.8	< 2.2	> 1.1
A13	1.25	1.28	5	3.3	< 2.4	> 1.2
A14	0.42	2.08	5.5	6.2	5.2	0.4
A15	−0.60	1.65	5	5.6	17	1.2
A16	−0.88	1.50	5	4.5	5.2	0.2
A17	−1.22	1.70	6	3.8	< 3.4	> 2.1
A18	−1.28	1.35	6	2.0	< 18	> 1.2
A19	−1.55	1.40	6	2.4	< 12	> 1.4
A20	−1.70	1.20	6	4.2	< 24	> 2.4
I1	−0.88	−1.00	4	3.8	54	0.6
I2	−0.65	−1.30	4	2.8	50	0.2
I3	−1.00	−1.90	6	0.9	15	0.2
I4	−0.40	−2.02	6	1.9	22	0.3
I5	1.22	−1.22	5	2.0	39	0.4
I6	0.80	0.48	3	1.7	< 7.7	> 0.2

References

Blitz, L. 1985, *Ap. J.*, **296**, 481.

Elmegreen, B. G. 1987a in *I.A.U. Symposium No. 115, Star Forming Regions*, ed. M. Peimbert and J. Jugaku (Dordrecht: Reidel), p. 457-481.

Elmegreen, B. G. 1987b in *Galactic and Extragalactic Star Formation* ed. R. E. Pudritz and M. Fich (Kluwer), p. 215-225.

Elmegreen, B. G. 1987c, *Ap. J.*, **312**, 626.

Elmegreen, B. G. and Elmegreen, D. M. 1986, *Ap. J.*, **311**, 554.

Lord, S. D., and Young, J. S. 1990, *Ap. J.*, **356**, 135.

Rand, R. J. and Kulkarni, S. R 1989, in *Submillimetre Astronomy*, ed. G. D. Watt and A. S. Webster, (Dordrecht: Kluwer), p. 239.

Roberts, W. W. and Stewart, G. R 1987, *Ap. J.*, **314**, 10.

Rydbeck, G., Hjalmarson, A. and Rydbeck, O. E. H. 1985, *Astr. Ap.*, **144**, 282.

Sandage, A. and Tammann, G. A. 1975, *Ap. J.*, **196**, 313.

Schweizer, F. 1976, *Ap. J. Suppl.*, **31**, 313.

Scoville, N.Z. and Sanders, D.B. 1987, in *Interstellar Processes*, ed. D. J. Hollenbach and H. A. Thronson (Dordrecht: Reidel), p. 21.

Scoville, N.Z., Sanders, D.B. and Clemens, D.P. 1986, *Ap. J. (Letters)*, **310**, L77.

Seiden, P. E. and Gerola, H. 1979, *Ap. J.*, **233**, 56.

Shu, F. H., Milione, V. and Roberts, W. W. 1973, *Ap. J.*, **183**, 819.

Tilanus, R. P. J., and Allen, R. J. 1989, *Ap. J. (Letters)*, **339**, L57.

Tilanus, R. P. J., Allen, R. J., van der Hulst, J. M., Crane, P. C. and Kennicutt, R. C. 1988, *Ap. J.*, **330**, 667.

Tully, R. B. 1974a, *Ap. J. Suppl.*, **27**, 437.

Tully, R. B. 1974b, *Ap. J. Suppl.*, **27**, 449.

Visser, H. C. D. 1980, *Astr. Ap.*, **88**, 159.

Vogel, S. N., Kulkarni, S. R. and Scoville, N. Z. 1988, *Nature*, **334**, 402 (VKS).

Figure Captions

FIG. 1. Mosaic map of CO emission in M51 overlaid on *a)* an Hα CCD image and *b)* a red continuum CCD image, with the GMAs labelled. The mapped region is outlined by the dashed curve. No data from beyond the half-power point of the primary beam are included in the mosaic. Due to improvements in receiver sensitivity and atmospheric conditions over the three year span of the observations, there is a variation in rms noise of about a factor of two over the mosaic. Sensitivity generally improves from NW to SE in the map, ranging from about 2 Jy km s^{-1} $beam^{-1}$ to 4 Jy km s^{-1} $beam^{-1}$. The contour levels are 4.5, 7.8, 13.5, 22.5, 31.5 and 40.5 Jy km s^{-1} $beam^{-1}$. The CCD images were taken with the 60" telescope at Palomar. Registration of the mosaic map and optical images was achieved to an accuracy of better than 1" by deriving the positions of secondary stars in the CCD image from nearby SAO stars.

FIG. 2. Virial mass ($M_{\rm Vir}$) versus flux-based mass ($M_{\rm CO}$) for distinct components of GMAs. The solid line indicates equality between the two masses, while the dashed line indicates the marginally bound case. Upper limits on virial masses are indicated by the arrows.

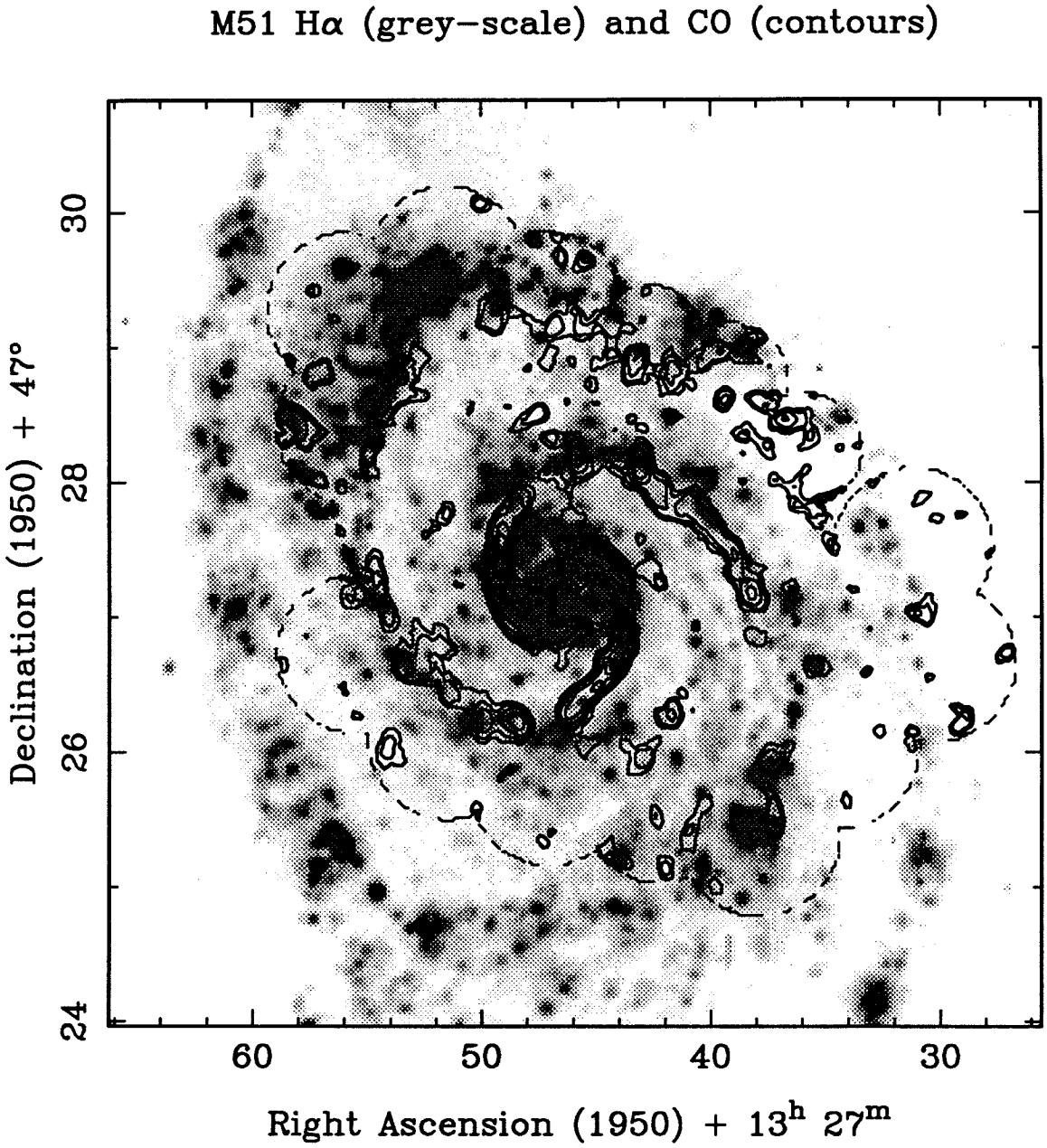
M51 Hα (grey−scale) and CO (contours)
Declination (1950) + 47°
30
28
26
24
60
50
40
30
Right Ascension (1950) + 13h 27m

Figure 1*a*

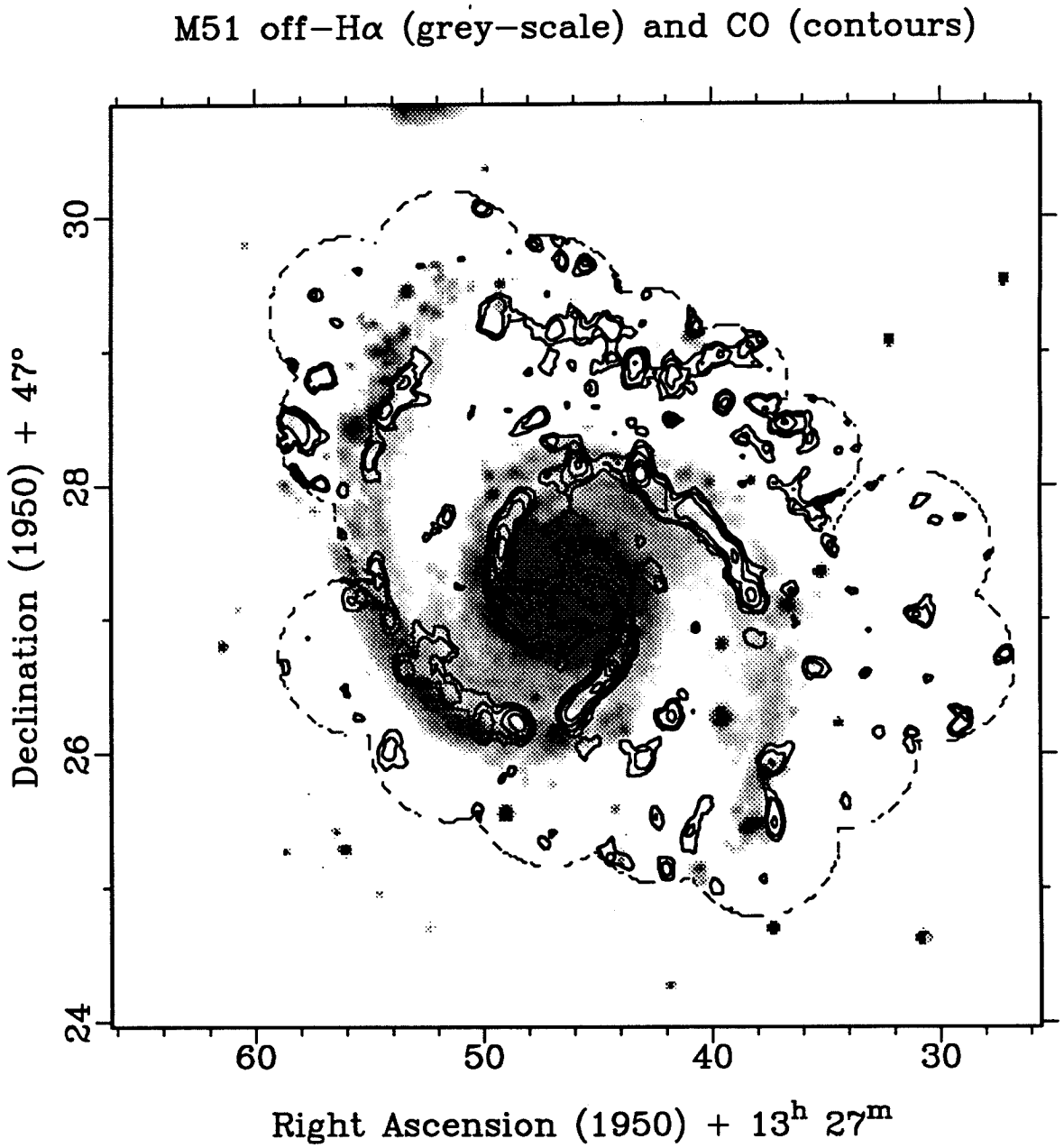
M51 off−Hα (grey−scale) and CO (contours)
Declination (1950) + 47°
30
28
26
24
60
50
40
30
Right Ascension (1950) + 13h 27m

Figure 1*b*

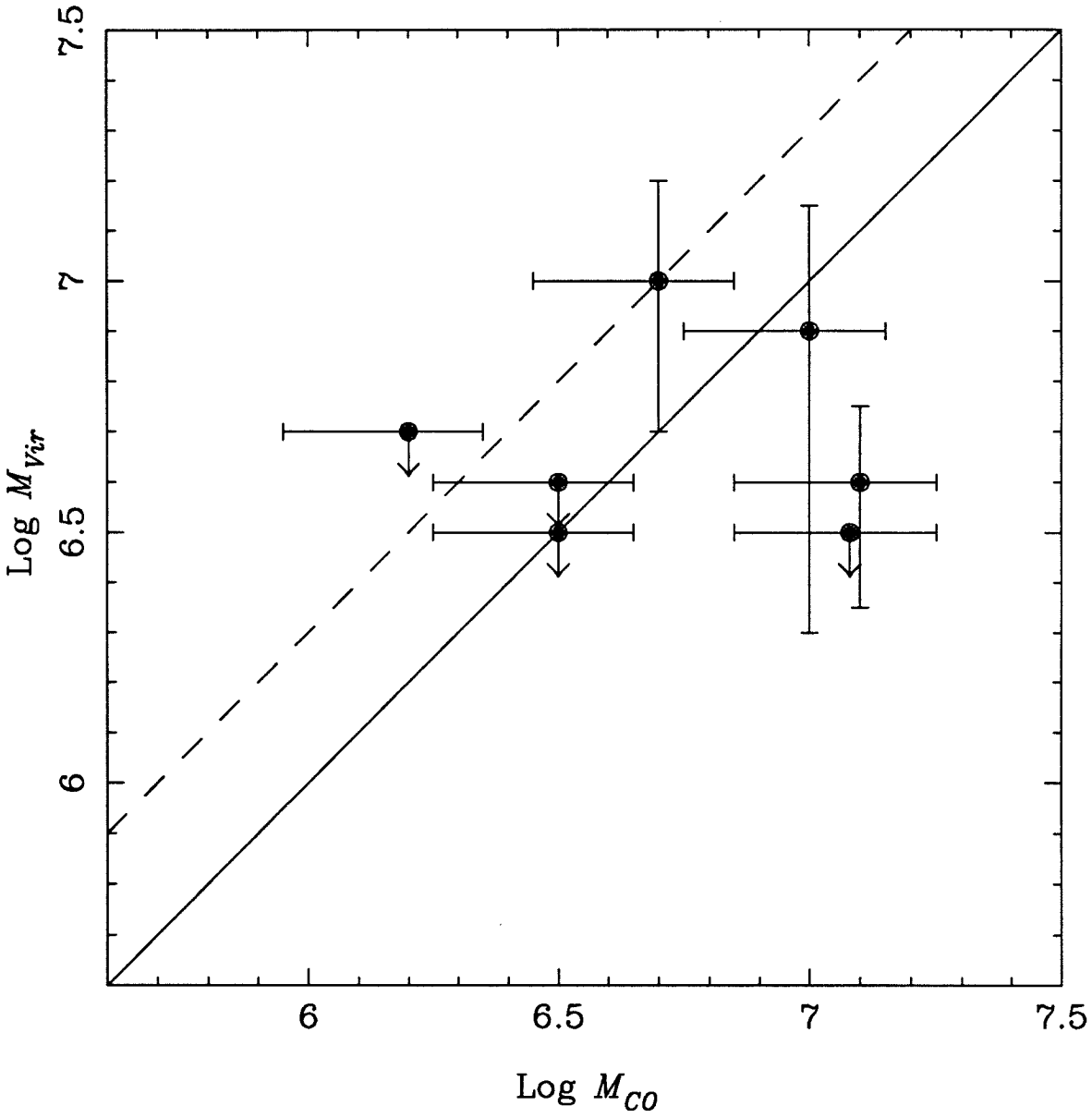

Figure 2

CHAPTER 3

Observations of Molecular Gas in M51 at 2.5" Resolution

Abstract

We present a CO (1–0) map of two one-arcminute fields in M51 at 2.5" resolution made with the Millimeter Interferometer of the Owens Valley Radio Observatory. The fields include three on-arm and two interarm Giant Molecular Associations (GMAs) identified earlier in our 8" mosaic map. The GMAs are well resolved at this resolution. The tangential velocity shift across the arm at the major axis crossing agrees with the shift measured from the 8" mosaic. The one-dimensional velocity dispersion on the arms at this resolution is about 10 km s^{-1}. We estimate virial masses with separate contributions from the random and systematic (streaming) motions within the GMAs. For the on-arm GMAs, the virial masses indicate that they are roughly gravitationally bound. The virial masses of the interarm GMAs confirm that they are unbound. Problems associated with the apparent boundedness of the on-arm GMAs are briefly mentioned here and more fully discussed in a later paper. We confirm that the on-arm GMAs are stable against galactic tidal forces, while the interarm GMAs are close to the condition of marginal stability. A possible reason, based on gravitational instability theory, for the difference in on-arm and interarm GMA properties is discussed. The detailed spatial coincidence between molecular emission and Hα emission is poor. Several

possible explanations are given for this. The interarm GMAs have very little associated Hα emission compared to the on-arm CO emission. This contrast may be related to the GMA formation process.

Subject headings: galaxies: interstellar matter – stars: formation – galaxies indiv: (M51) – interferometry

I. Introduction

Over the past few years, we have been carrying out an observational program to understand the relationship between the density wave, molecular gas and star formation in the grand-design spiral galaxy M51. In previous papers (Vogel, Kulkarni and Scoville 1988; Rand and Kulkarni 1990a, hereafter RK) mosaic maps were presented of CO (1–0) emission from M51 at 8" resolution made with the Millimeter Interferometer of the Owens Valley Radio Observatory. We briefly summarize the relevant results from those papers here. There is a narrow, two-armed spiral pattern in the molecular gas. The molecular arms well aligned with the dust lanes, but offset upstream from the HII region arms. The tangential and radial velocity shifts predicted by density wave theory are clearly seen where the arms cross the major and minor axes of the galaxy. Using Hα emission as a tracer of the massive star formation rate, we find that the star formation efficiency (SFE) is higher on the arms than between the arms, implying that the density wave is triggering excess star formation from the compressed gas. This SFE contrast depends on our knowledge of the molecular arm-interarm contrast, which is potentially difficult to measure from interferometric data. However, we have confidence that we have reliably measured the SFE contrast, since single-dish observations have subsequently confirmed our result (Lord and Young 1990). The molecular arms contain discrete emission features which we termed Giant Molecular Associations (GMAs), which have a typical mass of 3×10^7 $M_\odot$. GMAs are also found between the arms. We find indications that the on-arm GMAs are roughly gravitationally bound, while

the interarm GMAs are unbound. The spectra of the GMAs show that they typically consist of one to five velocity components (see Figure 1). Possible formation mechanisms for the GMAs include collisional agglomeration of pre-existing smaller clouds and gravitational instability. There is evidence that the interarm GMAs are formed in a weak, secondary compression of the density wave.

We chose to follow up these observations with higher resolution maps for three reasons. First, because many of the GMAs, especially on the arms, were unresolved or not well resolved, one may be concerned about whether reliable virial masses can be estimated. Second, with higher resolution observations we expect to measure more accurate, spatially-resolved velocity gradients across the arm. Third, the CO spectra indicated that the GMAs consist of a small number of components which might be spatially separated if mapped at higher resolution. For these reasons, we mapped two adjacent fields, chosen to contain on-arm and interarm GMAs, at 2.5" resolution. One of the fields includes a major-axis crossing of the molecular spiral arm south of the nucleus. The on-arm GMAs in these fields were all unresolved in our mosaic map.

II. Observations

The observations were made in the years 1988 through 1990 with the Millimeter Wave Interferometer of the Owens Valley Radio Observatory. The instrument consists of three 10.4 m dishes which are equipped with SIS receivers, cryogenically cooled to 4 K. The filterbank used for the data presented here consists of 32 1-MHz

channels, giving a resolution of 2.6 km s^{-1}. The low resolution data (two configurations with deprojected baselines ranging from 15 m to 55 m) were used in the mosaic of RK and were taken in the months of February, May, and November 1988, and January 1989. The high resolution data (three configurations with baselines ranging from 60 m to 205 m) were taken in January and February 1990.

The synthesized beam is about 2.7" × 2.2" (P.A. = 0°), giving a linear resolution of 125 × 100 pc, assuming a distance of 9.6 Mpc (Sandage and Tammann 1975). The primary beam is 65" (HPBW). Phase calibration was based on observations of the quasar 1418+546 every 15 min. Mars, Uranus, 3C 84 and 3C273 were used to determine the flux scale, giving an uncertainty of about 10%. The mapping was carried out using standard NRAO AIPS software. Pairs of channels were averaged together before mapping to improve sensitivity. The final velocity resolution is therefore 5.2 km s^{-1}. The two maps were combined into a single data set through a simple mosaicing procedure which corrects for the primary beam attenuation.

III. Results and Discussion

Shown in Figure 2*a* is the contour map of total intensity of CO emission for the two fields. The spiral arm can clearly be seen, as well the on-arm GMAs A4, A8 and A9, and the interarm GMAs I1 and I2 (see RK for identification of GMAs). Some of the circumnuclear emission seen in the 8" map is detected, but most of the gas in that region emits at velocities outside the range of the filterbank for these observations, and so is missed in this map.

Of the on-arm GMAs, A4 remains relatively compact at this resolution, while A8 shows a significant amount of substructure. A9 is intermediate between these extremes. All three GMAs were unresolved in the 8" mosaic (RK). The substructure observed in the GMAs here confirms our expectations based on the CO spectra from the 8" mosaic cube.

The brightness temperature of the gas along the arm ranges from 2 to 10 K, with 6 K being a typical value for the GMAs, and 3 K being typical of the gas between the GMAs. These numbers are comparable to the brightness temperatures of Galactic GMCs of 5–10 K (*e.g.,* Scoville and Sanders 1987). The brightness temperature reflects both the actual temperature of the clouds and their areal filling factor. If the molecular clouds in M51 are actually at about the same temperature as the Galactic GMCs, then the areal filling factor of the clouds along the arms of M51 is close to unity. Alternatively, the clouds may be hotter than Galactic GMCs and have a filling factor less than unity. Possible support for the latter interpretation comes from the high $^{12}CO/^{13}CO$ ratio found for the disk of M51 by Young and Sanders (1986). The ratio of about 11 that they find for regions 1–5 kpc from the nucleus is about twice the value for clouds in the inner Milky Way. Hotter gas is likely to lead to such a difference; however, there may also be a correlation of the isotope ratio with metallicity (Young and Sanders 1986).

a) Streaming Motions and Velocity Dispersion

The streaming motions we found at 8" resolution in RK along this arm are confirmed at the higher resolution. Figure 3 shows velocity cuts through the major axis GMAs A8 and A9 in directions across and along the arms. For tangential motions on this side of the major axis, increasing V_{lsr} corresponds to increasing tangential velocities in the plane of M51. No systematic motions are seen in the cuts along the arms. Whereas the underlying rotation curve is flat (Tully 1974), the across-arm cuts both show a positive velocity shift of about $dv/dR = 130$ km s^{-1} kpc^{-1} in the plane of the sky, assuming an inclination of 20° (Tully 1974). Hence the tangential streaming at this southern crossing of the major axis is somewhat greater than the (spatially-resolved) streaming of 90 km s^{-1} kpc^{-1} reported for the northern crossing by RK. This velocity gradient is steeper than that expected for solid-body rotation at this radius, indicating that a condition of "reverse shear" exists at this location. No streaming motion has been detected in the interarm GMAs I1 and I2. The 1-d velocity dispersion along the arms was computed in two ways. First, we used a "dispersion map" produced by the MOMNT program of the NRAO AIPS package. The second method was to fit spectra at various points along the arms with Gaussians. Both methods show that the dispersion along the arms ranges from about 6 to 13 km s^{-1}, with a mean value of 10 km s^{-1}. The shift expected over a resolution element from the tangential streaming is only 5 km s^{-1}, so the observed dispersion in each resolution element is dominated by random and not systematic motions.

b) Virial Masses

We recalculate the virial masses and masses based on CO flux reported in RK to check the boundedness of the GMAs. We derive here a formula for the virial mass which includes terms representing both the random and systematic motions in a GMA. For equality between the gravitational and random kinetic energy, Scoville and Sanders (1987) give for the virial mass in $M_\odot$:

$$M_{vir,random} = 550 D (\sigma_{1d})^2. \quad (1)$$

where D is the observed FWHM diameter in parsecs, and σ_{1d} is the 1-d velocity dispersion. This formula assumes a $1/r$ density profile.

Our measurement of the systematic velocity shift across the major-axis GMAs implies that there is a shear across them. This shear has an energy associated with it and therefore must be taken into account in the virial analysis. The shear can be treated approximately as a kinetic energy term in the virial theorem. At galactocentric radius R, the rate of shear is twice the generalized Oort A constant: $2A(R) = (dv/dR - v/R)$. The shift for a fluid element at any distance r from the center of the GMA is $\Delta v = 2A(R)\, r \cos\theta$, where $r\cos\theta$ is the projected distance of the fluid element from the GMA center along the tangential axis. The kinetic energy term in the virial theorem, $2T = \int_V \rho\, (\Delta v)^2\, dV$, is then

$$2T = \int_0^{\pi} \int_0^{R_{cl}} \rho(r) (2A(R)\, r \cos\theta)^2 2\pi r^2 \cos\theta \, dr d\theta \quad (2)$$

where $\rho(r)$ is the density at radius r, and R_{cl} is the radius of the cloud. Integrating using a $1/r$ density profile, $\rho = \rho_{R_{cl}} R_{cl}/r$, we find

$$2T = 4/3\, M A(R)^2 R_{cl}^2 \quad (3),$$

where M is the mass. Setting this equal to the gravitational potential energy, $2GM^2/3R_{cl}$, we find that virialization in the presence of the systematic shift alone requires

$$M_{vir,systematic} = 5.6 \times 10^{-5} A(R)^2 D^3 \quad (4),$$

where the units of $M_{vir,systematic}$ are $M_\odot$, $A(R)$ is in km s^{-1} kpc^{-1}, and D, the cloud diameter, is in pc.

The virial mass in the presence of both random and systematic motions therefore reduces to

$$M_{vir} = 550 D(\sigma_{1d})^2 + 5.6 \times 10^{-5} A(R)^2 D^3 \quad (5).$$

The virial masses calculated according to equation (5) are shown in Table 1 for the five GMAs, along with the quantities D and σ_{1d}. For the on-arm GMAs, $\sigma_{1d} \approx 10 \pm 3$ km s^{-1}. For the interarm GMAs, the velocity dispersion was taken to be the average value over the GMAs measured from our dispersion map smoothed to 6" (still less than the size of the interarm GMAs). The rms of this mean provided an estimate of the uncertainty. Diameters of the interarm GMAs were measured from a map also smoothed to 6". For the GMA A4, which is not near the major axis, we assumed that the same tangential velocity shift exists across it as observed in A8 and A9. The virial masses for the interarm GMAs include only the random component. Along the major axis, the CO velocities indicate a typical rotation speed of 200 km s^{-1}. We use this value and a flat rotation curve (Tully 1974) to

calculate A. The shear component turns out to contribute only a small fraction of the virial mass ($\sim 10\%$).

The CO-flux-based mass, M_{CO} is calculated by assuming the Galactic conversion factor between CO luminosity and H_2 column density of $\alpha = 3 \times 10^{20}$ mol cm^{-2} (K km s^{-1})$^{-1}$. Values of M_{CO} are listed in Table 1.

The sources of error in the two mass estimates are as stated in RK. The fractional uncertainty in the CO-flux-based masses is about 50% , based on the sources of error listed in RK. However, we consider the CO masses estimated from the current map to be more uncertain than those estimated from the 8" map (see RK). The reason is that the inclusion of the high resolution data should have little effect on the total flux information but does add significantly to the noise in the map. We therefore believe our CO-flux-based mass estimates of these GMAs from the 8" mosaic to be more accurate. This is especially true for the interarm GMAs, which are particularly extended, low surface brightness features. In reality the on-arm GMA masses agree fairly well with our earlier measurements, but the interarm GMA masses are significantly higher than the values of 3.8×10^7 $M_\odot$ and 2.8×10^7 $M_\odot$ given in RK for I1 and I2, respectively. The fractional uncertainties on the virial masses are listed in Table 1.

At this resolution, we find that the virial masses for the on-arm GMAs are certainly not higher than the CO-flux-based masses, and in fact are systematically lower by about a factor of 2. This discrepancy exists whether we use the current CO-flux based masses or those from the 8" mosaic. The disagreement may simply reflect

the systematic uncertainty in the conversion factor, α. The high $^{12}CO/^{13}CO$ ratio in M51 may provide some evidence in favor of this explanation (see above). The virial theorem indicates, however, that the on-arm GMAs are roughly gravitationally bound. The interarm GMAs have virial masses greater than their CO-flux-based masses and several times greater than those of the on-arm GMAs, and so they still appear to be unbound.

If the on-arm GMAs are actually bound, then some problems arise. These are only briefly mentioned here and will be discussed more fully in an upcoming paper (Rand and Kulkarni 1990b). First, if the shear observed across A8 and A9 persisted at its current rate, the GMA lifetime would be limited by the shearing disruption to $\sim 2 \times 10^7$ yr (Rand and Kulkarni 1990b). Therefore, the energy associated with the shear must quickly be dissipated or converted into rotational or random kinetic energy in order for these GMAs to remain bound. However, no major-axis GMAs in the 8" mosaic are observed to have evolved into this state, *i.e.,* none is observed *without* streaming across it. In fact, there is no evidence that any of the GMAs show streaming that is any different from the gas observed between them (see Figure 2 of Vogel, Kulkarni, and Scoville [1988]). For the northern major axis, shear disruption may not be such a problem since the local rotation curve is close to solid-body and the shear timescale is much longer ($\sim 10^8$ yr; Rand and Kulkarni 1990b).

The second problem is that in order to explain their confinement to narrow spiral arms, bound GMAs must be rapidly destroyed as they move off the arms.

In Rand and Kulkarni (1990b), we discuss the plausibility of and uncertainties associated with disruption by star formation or galactic tidal forces.

c) Tidal Stability

In RK, we suggested that the on-arm GMAs are stable against galactic tidal forces while the interarm GMAs were not stable. Thus, bound GMAs may be disrupted by tidal forces when they move off the arms. We can make a stronger statement regarding tidal stability with the new high-resolution data. The minimum density for stability against galactic tidal forces is $n_t(R) = A(R)\Omega(R)/G$ where $A(R)$ is the Oort constant at radius R, $\Omega(R)$ is the orbital angular frequency, and G is the gravitational constant. This expression can be derived by balancing the tidal acceleration (*e.g.,* Stark and Blitz 1978) with the gravitational force per unit mass of the cloud. Using the flat rotation curve and the tangential streaming motion mentioned above, we calculate n_t at $R = 2$ kpc to be 8 mol cm^{-3}, and at $R = 3$ kpc, $n_t = 11$ mol cm^{-3}. The average column densities and FWHM diameters of the GMAs can be used to find the mean densities, assuming spherical symmetry. The resulting densities are 36, 34 and 17 mol cm^{-3} for on-arm GMAs A4, A8, and A9, respectively. Hence the on-arm GMAs appear to be tidally stable. The interarm GMAs (at $R \approx 4$ kpc) have ratios of true to tidal densities a few times smaller and are therefore close to the point of marginal stability, assuming the rotation curve is essentially flat in the interarm regions.

d) Spatial Relationship with Hα Emission

Figure 2*b* shows the CO contours overlaid on our continuum-subtracted Hα CCD image (see RK). While it is clear that CO and Hα emission is concentrated to the arms, the detailed agreement between regions of CO and Hα emission along the arms is poor. A4, for instance, is a relatively massive GMA, but only has a faint HII region associated with it. A9, on the other hand, has a lower mass but has a very bright HII region associated with it. To the west of A8, there are HII regions with no detectable CO in their vicinity. The interarm GMAs have little Hα emission associated with them. What are the possible explanations for this breakdown in correlation on small scales?

Simple variations in the star formation efficiency (SFE) may be one explanation for the lack of correlation. If so, then A4 would be a region of low SFE, while A9 would have a high SFE. The interarm GMAs would have particularly low SFEs in this explanation. If they are formed in a weak, secondary compression of the density wave, as suggested by RK, then this SFE contrast between the main and secondary arms may be an example of how the SFE depends on the spiral arm strength. Elmegreen (1987) has suggested that, for formation of large structures by gravitational instability in spiral arms, there is insufficient time in weak compressions for the instabilities to fully develop, so that preexisting clouds are only temporarily brought together into loose agglomerations. The rate of dissipation would be much less than in a strong compression, so that little star formation would occur before the agglomerations disband again due to the expanding flow. In Rand and Kulkarni (1990b) we demonstrate, by carrying out an analysis based on

Kennicutt (1989), that the interarm gas is close to the condition for gravitational instability. A weak compression could be sufficient to trigger weak instabilities in the gas. These ideas would explain both the unbound nature of the interarm GMAs and the lack of much associated Hα emission.

Second, the poor correlation may be reflecting the temporal sequence of star formation. Two effects can lead to the disruption of GMAs into a diffuse enough state to be undetectable interferometrically: *i)* energy input from star formation (*e.g.,* stellar winds and supernovae), and *ii)* increased shear when the GMAs move off the arm. In this explanation then, the high-mass GMA A4, which has little associated Hα emission, is near the beginning of its star formation episode and has thus suffered little disruption by these effects, while A9, with its bright associated HII region, is more evolved and may already be significantly disrupted. There may once have been a GMA associated with the HII regions to the west of A8, but it may have been severely disrupted by this time.

Finally, patchy extinction might be naively expected to cause anticorrelation, since a higher gas surface density implies more extinction from the associated dust. We can test this possibility by comparing the Hα emission with the thermal radio emission. Tilanus *et al.* (1989) have carried out a separation of the 6 and 20-cm VLA maps of M51 into thermal and nonthermal components. Since the thermal fraction is very low, the sensitivity of the map of thermal emission is somewhat poor. However, there does seem to be a relatively bright thermal feature at about the position of the faint HII region near A4, indicating that there is in fact relatively

high extinction in that region. The bright HII region associated with A9 also shows a bright thermal feature, while the HII regions with little associated CO emission show very little detectable thermal emission. From the thermal and Hα fluxes, we can estimate rough visual extinctions using the formula given in van der Hulst *et al.* (1988), who used the 6-cm VLA map (as an indicator of thermal emission) and an Hα image to estimate extinctions toward giant HII regions. The extinction we estimate for the HII region near A9 is 1.9 mag, which compares well with the value of 2.2 mag found by van der Hulst *et al.* Near A4, we estimate an extinction of about 3 mag, while for the HII regions to the west of A8 the extinction is less than 0.5 mag. Hence, the thermal radio data indicates that there are significant small-scale variations in the extinction which contribute to the anticorrelation. For these three regions at least, a higher extinction does seem to correlate with a higher gas surface density. A more systematic study over the disk of the galaxy should be carried out to test this correlation.

It would be interesting to know how the SFE varies along and between spiral arms on small scales in order to test various theories of star formation triggering. An example is the consequence of a possibly low SFE for interarm GMAs as mentioned above. Another interesting question is whether the GMAs have a higher SFE than other on-arm gas. A caveat arising from this discussion, however, is that it is difficult to interpret such small scale CO and Hα emission in terms of potentially interesting real SFE variations without understanding these other decorrelating effects in greater detail.

IV. Conclusions

We have reported high-resolution CO observations of two 1-arcminute fields in M51 south of the nucleus. The molecular spiral arm and the GMAs are well resolved at this resolution. The GMAs show much substructure, often with several peaks of emission. The brightness temperatures of the GMAs are about equal to the typical value for Galactic GMCs, indicating either hotter gas or a high cloud filling factor in M51. The tangential streaming motions noted by RK where the arm crosses the major axis are confirmed, and the streaming velocity gradient across this southern arm is steeper than the gradient across the northern arm. The 1-d velocity dispersion of the molecular gas along the arms at this resolution is roughly 10 km s^{-1}. The virial theorem – with both the random and systematic motions within the GMAs included – indicates that the on-arm GMAs are roughly gravitationally bound while the interarm GMAs are unbound. There are some problems, however, with the conclusion that the on-arm GMAs are bound. The on-arm GMAs are probably stable against galactic tidal forces while they are on the arms. The interarm GMAs are only marginally stable. The poor small-scale agreement between CO and Hα fluxes has several possible causes, including *a)* real SFE variations, *b)* star formation at different stages along the arm, and *c)* patchy extinction. There is evidence from the thermal radio emission that extinction variations are indeed a contributor to the lack of agreement.

Acknowledgements

We thank E. S. Phinney, N. Z. Scoville, and S. A. Balbus for helpful comments. The Millimeter Interferometer of the Owens Valley Radio Observatory is supported by NSF grant AST 97-14405.

Table 1. GMA Properties at 2.5" Resolution

GMA	R.A. Offset from Nucleus (arcmin)	Dec. Offset from Nucleus (arcmin)	σ_{1d} (km s^{-1})	D (pc)	M^a_{CO} (10^7 M$_\odot$)	M_{Vir} (10^7 M$_\odot$)	Fractional Uncertainty in M_{Vir}	$\overline{n}/n_t$
A4	−0.42	−0.62	12	230	4.2	1.8	0.58	4.5
A8	0.28	−1.02	12	300	4.9	2.6	0.35	3.1
A9	0.50	−1.02	12	230	2.4	1.9	0.58	1.5
I1	−0.88	−1.00	22	630	6.1	17	0.33	1.1
I2	−0.65	−1.30	20	510	6.1	11	0.63	1.1

[a] M_{CO} is the mass based on the CO flux in the high resolution map. However, we consider the masses from RK to be more accurate, especially for the interarm GMAs (see text). The masses from RK are 3.8×10^7 M$_\odot$ and 2.8×10^7 M$_\odot$ for I1 and I2, respectively.

References

Elmegreen, B. G. 1987 in *I.A.U. Symposium No. 115, Star Forming Regions*, ed. M. Peimbert and J. Jugaku (Dordrecht: Reidel), p. 457-481.

Kennicutt, R. C. 1989, *Ap. J.*, **344**, 685.

Lord, S. D., and Young, J. S. 1990, *Ap. J.*, **356**, 135.

Rand, R. J., and Kulkarni, S. R. 1990a, *Ap. J. (Letters)*, **349**, L43 (RK).

Rand, R. J., and Kulkarni, S. R. 1990b, in preparation.

Sandage, A., and Tammann, G. A. 1975, *Ap. J.*, **196**, 313.

Scoville, N. Z., and Sanders, D. B. 1987, in *Interstellar Processes*, ed. D. Hollenbach and A. Thronson (Dordrecht: Reidel), p. 21.

Stark, A., and Blitz, L. 1978, *Ap. J. (Letters)*, **225**, L15.

Tilanus, R. P. J., Allen, R. J., van der Hulst, J. M., Crane, P. C., and Kennicutt, R. C. 1988, *Ap. J.*, **330**, 667.

Tully, R. B. 1974, *Ap. J. Suppl.*, **27**, 438.

van der Hulst, J. M., Kennicutt, R. C., Crane, P. C., and Rots, A. H. 1980, *Astr. Ap.*, **195**, 38.

Vogel, S. N., Kulkarni, S. R., and Scoville, N. Z. 1988, *Nature*, **334**, 402.

Young, J. S., and Sanders, D. B. 1986, *Ap. J.*, **302**, 680.

Figure Captions

FIG. 1. Spectra of the GMAs *a)* A1 and *b)* A10 from the mosaic map.

FIG. 2. *a)* Contours of CO flux at 2.5" resolution. Contour levels are 3, 4, 6, 8, 10, 13, 16 and 19 times the noise level of 0.7 Jy km s^{-1}. *b)* Contours of CO flux overlaid on an Hα image.

FIG. 3. Velocity profiles across GMAs A8 and A9, in directions across and along the spiral arm: *a)* A8, across the arm, *b)* A8, along the arm, *c)* A9, across the arm, and *d)* A9, along the arm. For the profiles across the arm, the abscissa is in the direction of increasing galactocentric radius, while for the profiles along the arm, the abscissa is in the direction of increasing Right Ascension. The increase in V_{lsr} across the arm for both GMAs indicate a boost in the tangential velocity in the sense predicted by density wave theory.

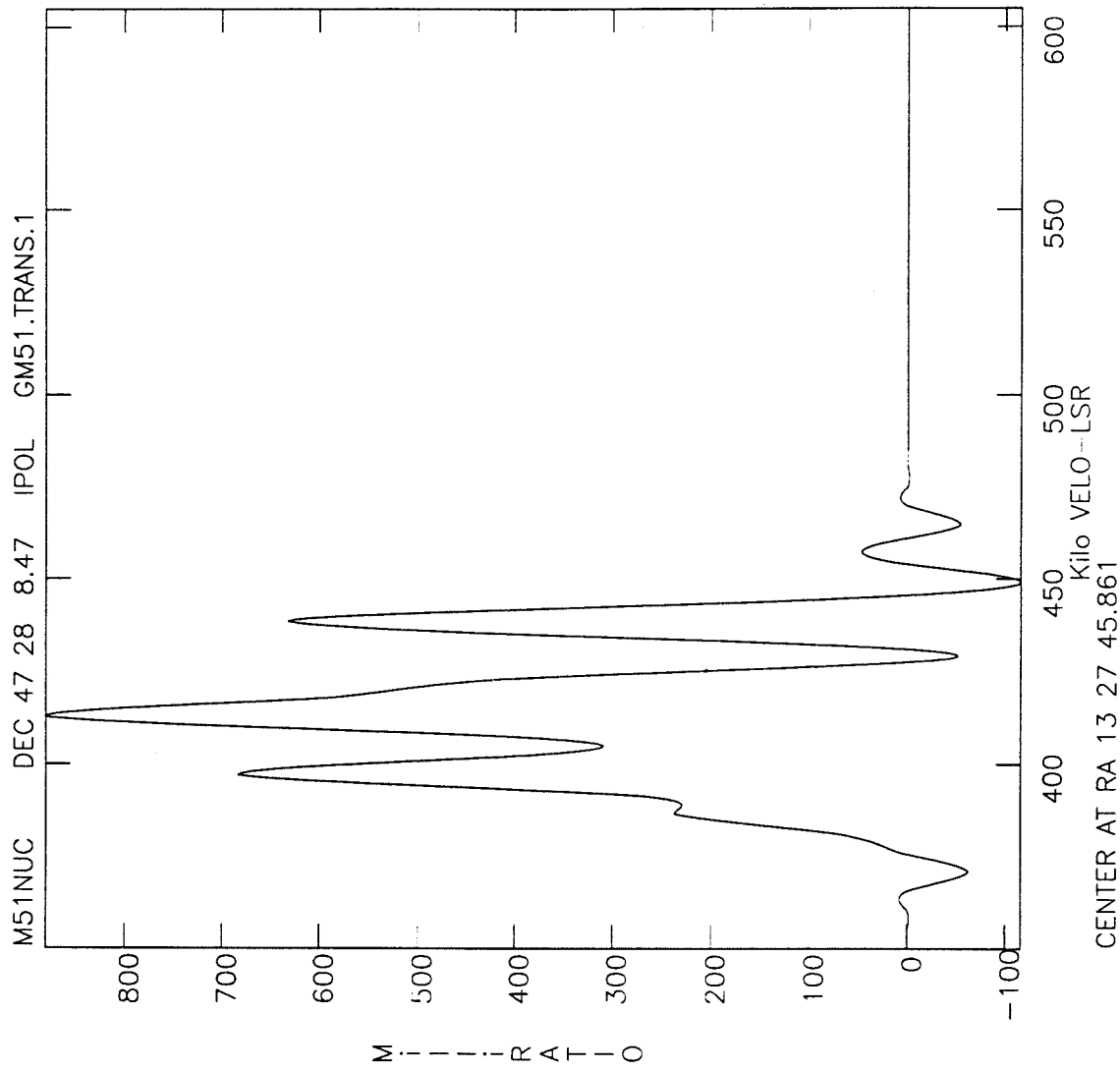
M51NUC DEC 47 28 8.47 IPOL GM51.TRANS.1
M
R
A
T
O
800
700
600
500
400
300
200
100
0
-100
400
450
500
550
600
Kilo VELO-LSR
CENTER AT RA 13 27 45.861

Figure 1*a*

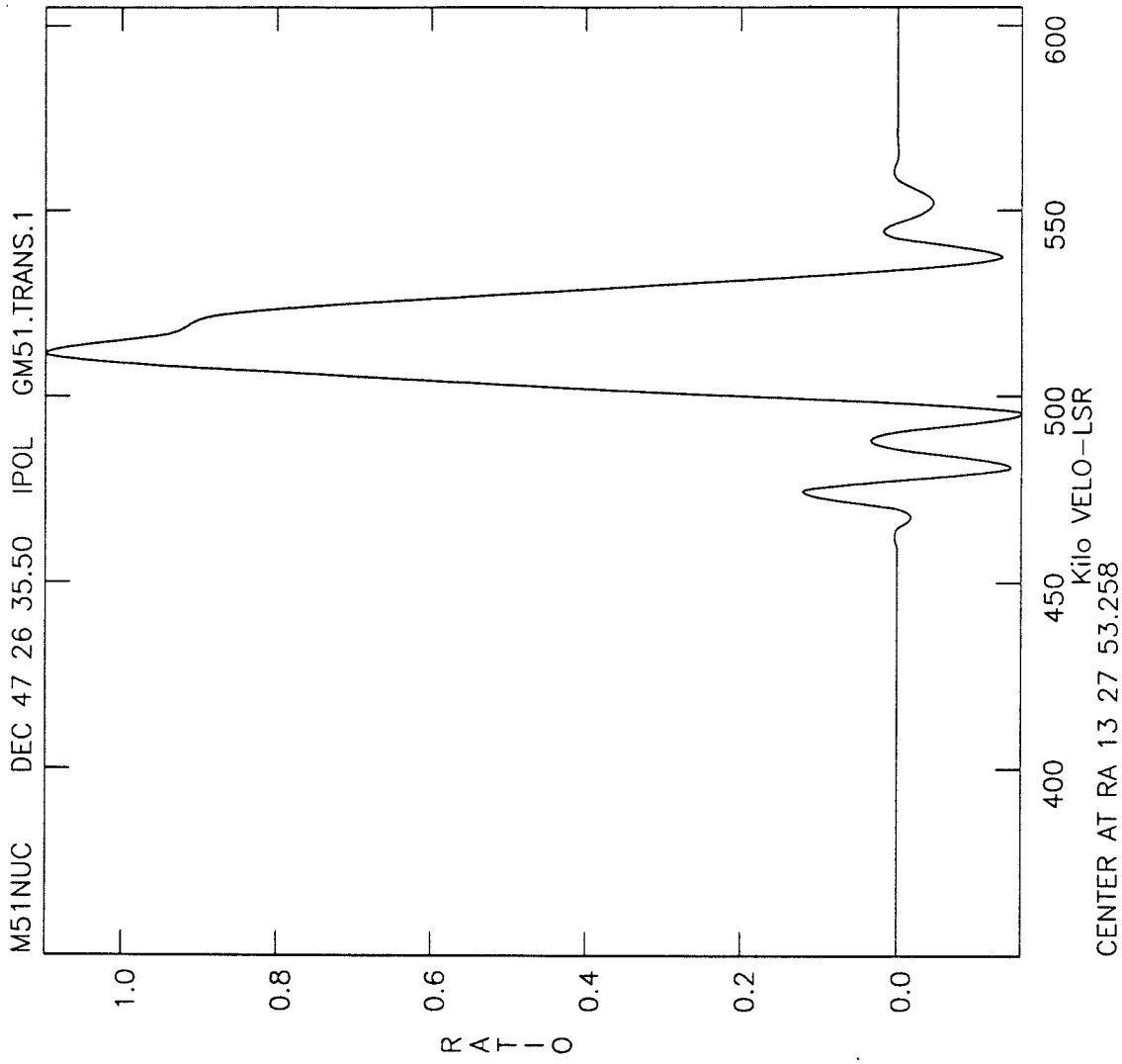
M51NUC DEC 47 26 35.50 IPOL GM51.TRANS.1
RATIO
1.0
0.8
0.6
0.4
0.2
0.0
400
450
500
550
600
Kilo VELO-LSR
CENTER AT RA 13 27 53.258

Figure 1*b*

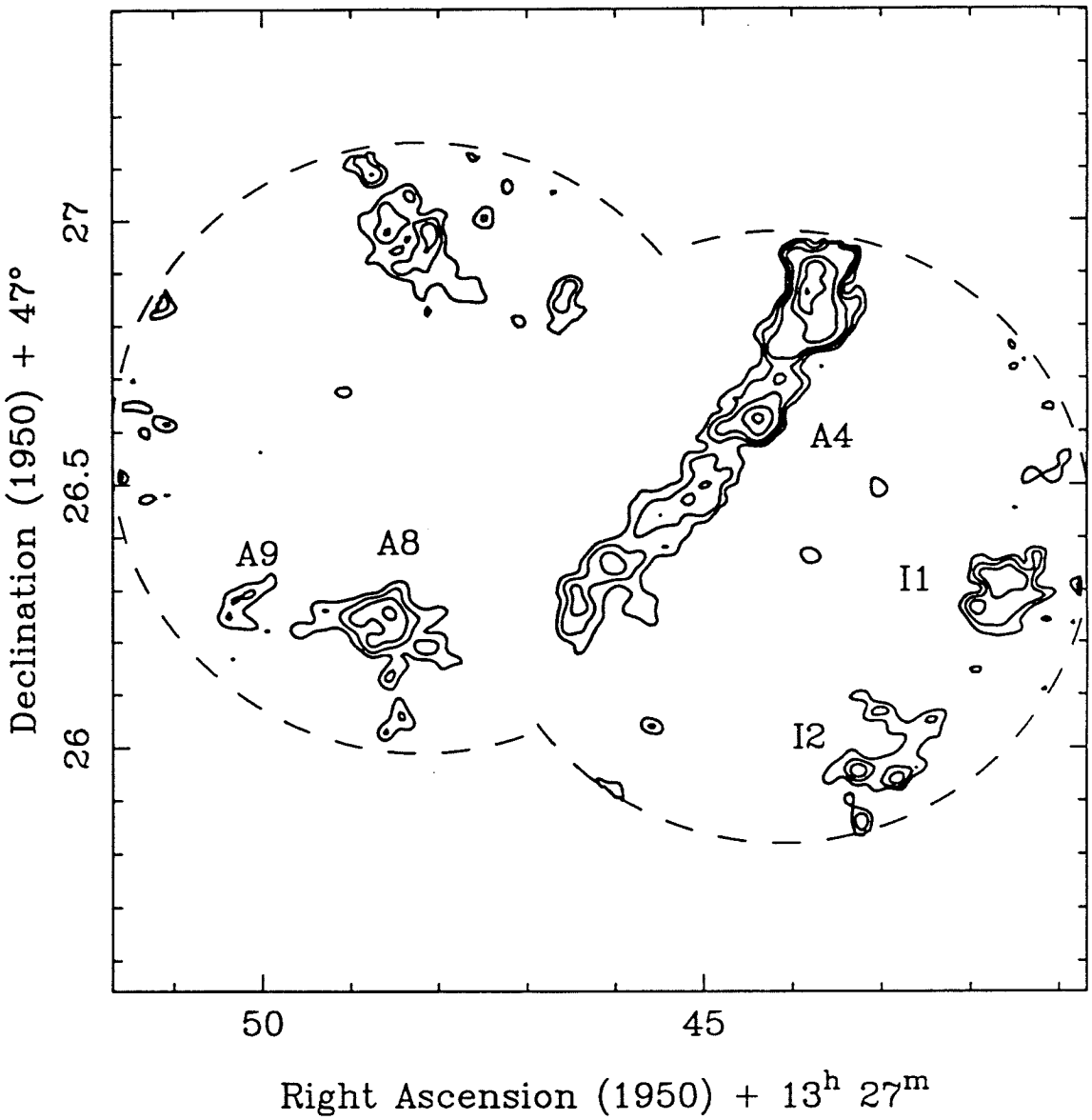
Declination (1950) + 47°
27
26.5
26
A4
A9
A8
I1
I2
50
45
Right Ascension (1950) + 13h 27m

Figure 2*a*

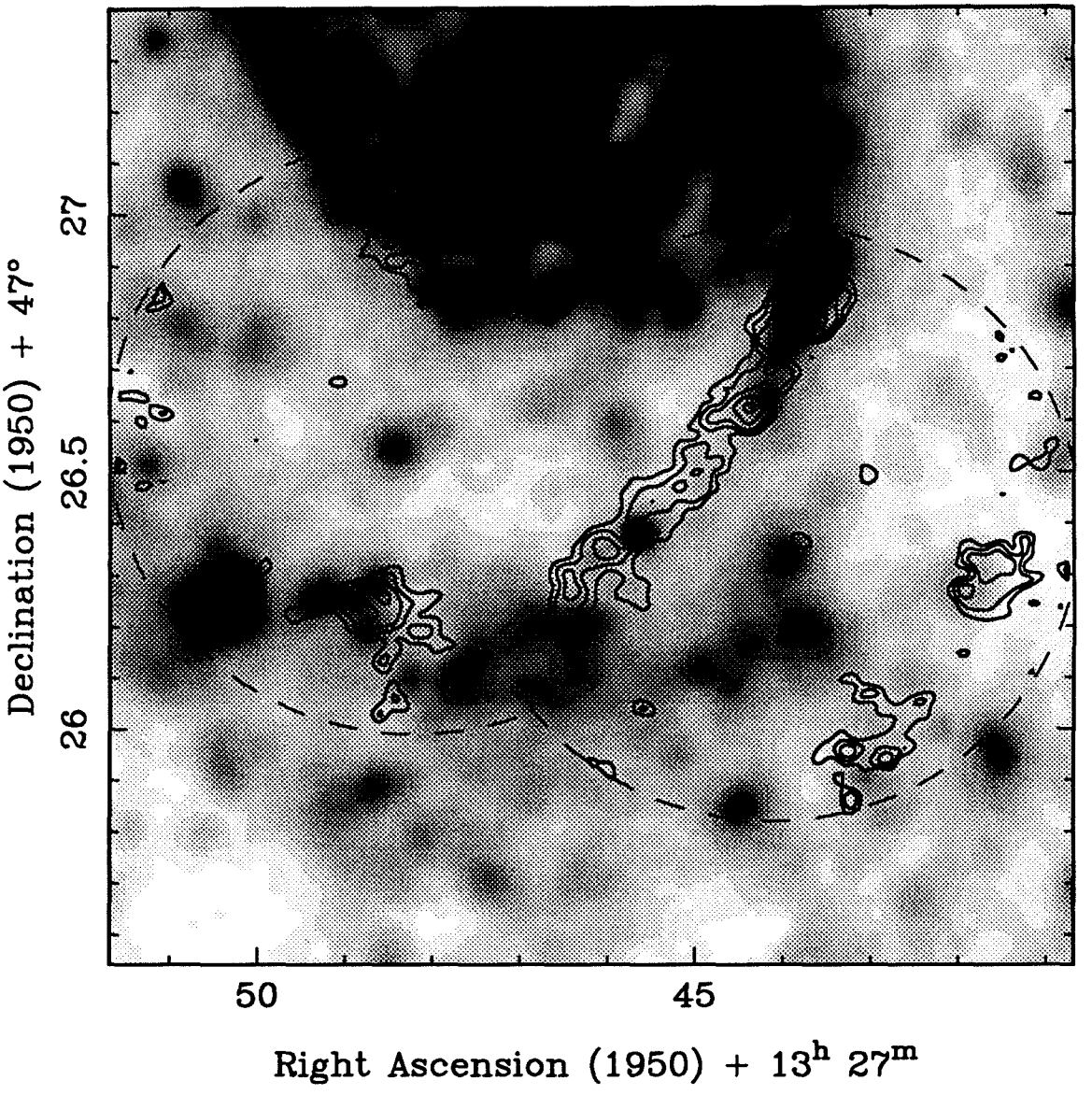
Declination (1950) + 47°
27
26.5
26
50
45
Right Ascension (1950) + 13h 27m

Figure 2*b*

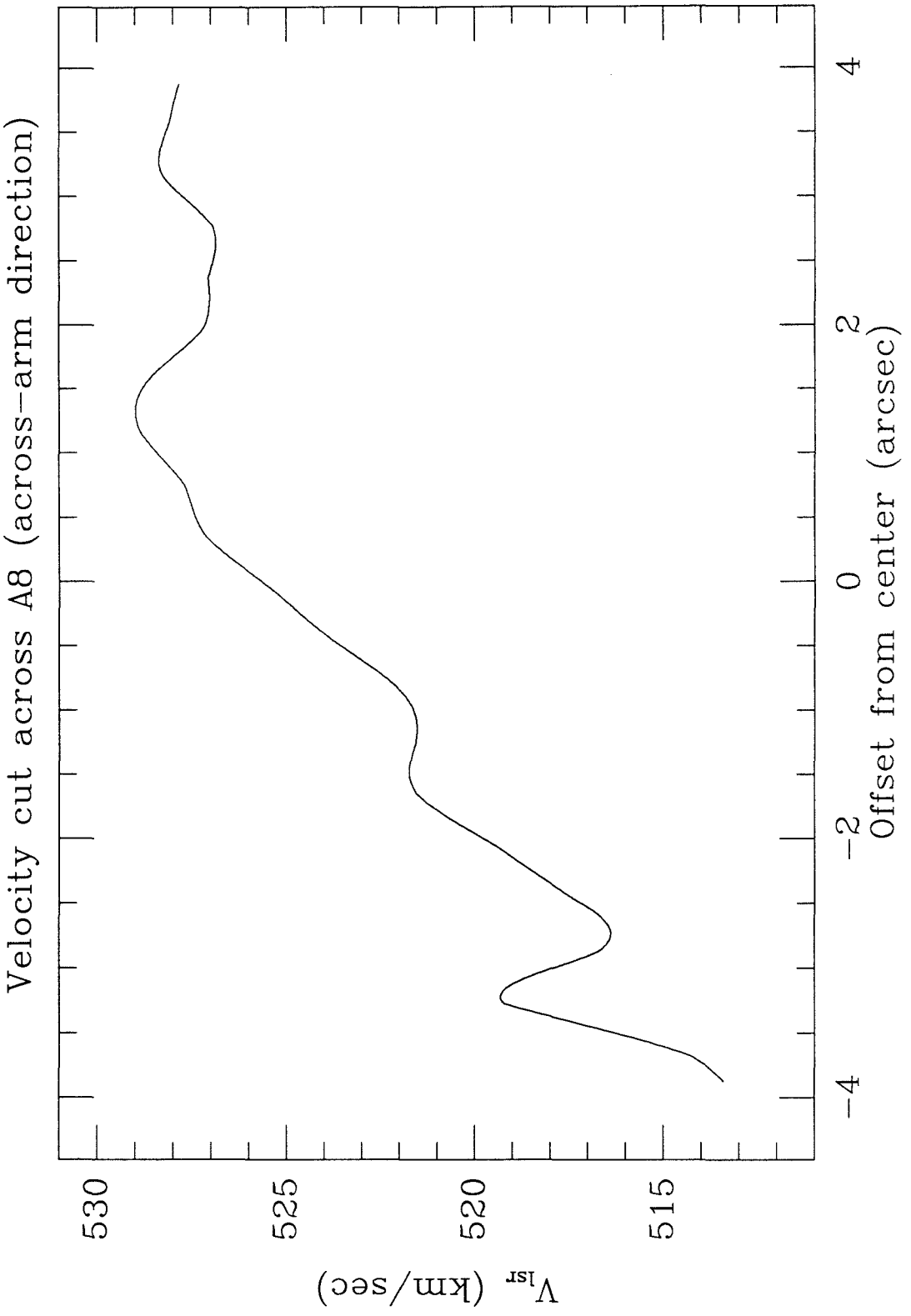
Velocity cut across A8 (across-arm direction)
530
525
520
515
V_{lsr} (km/sec)
−4
−2
0
2
4
Offset from center (arcsec)

Figure 3*a*

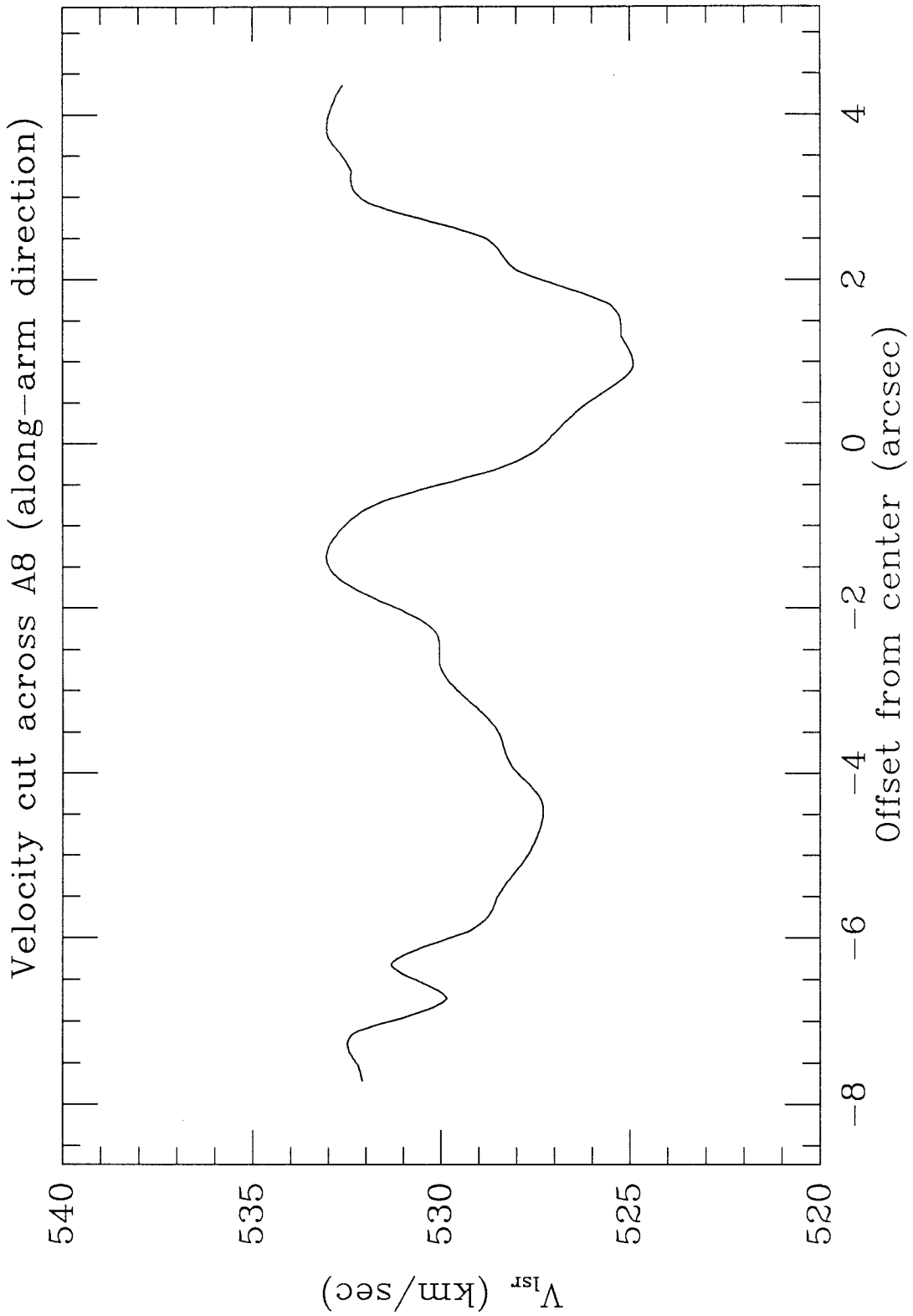
Velocity cut across A8 (along−arm direction)
V_{lsr} (km/sec)
540
535
530
525
520
−8
−6
−4
−2
0
2
4
Offset from center (arcsec)

Figure 3*b*

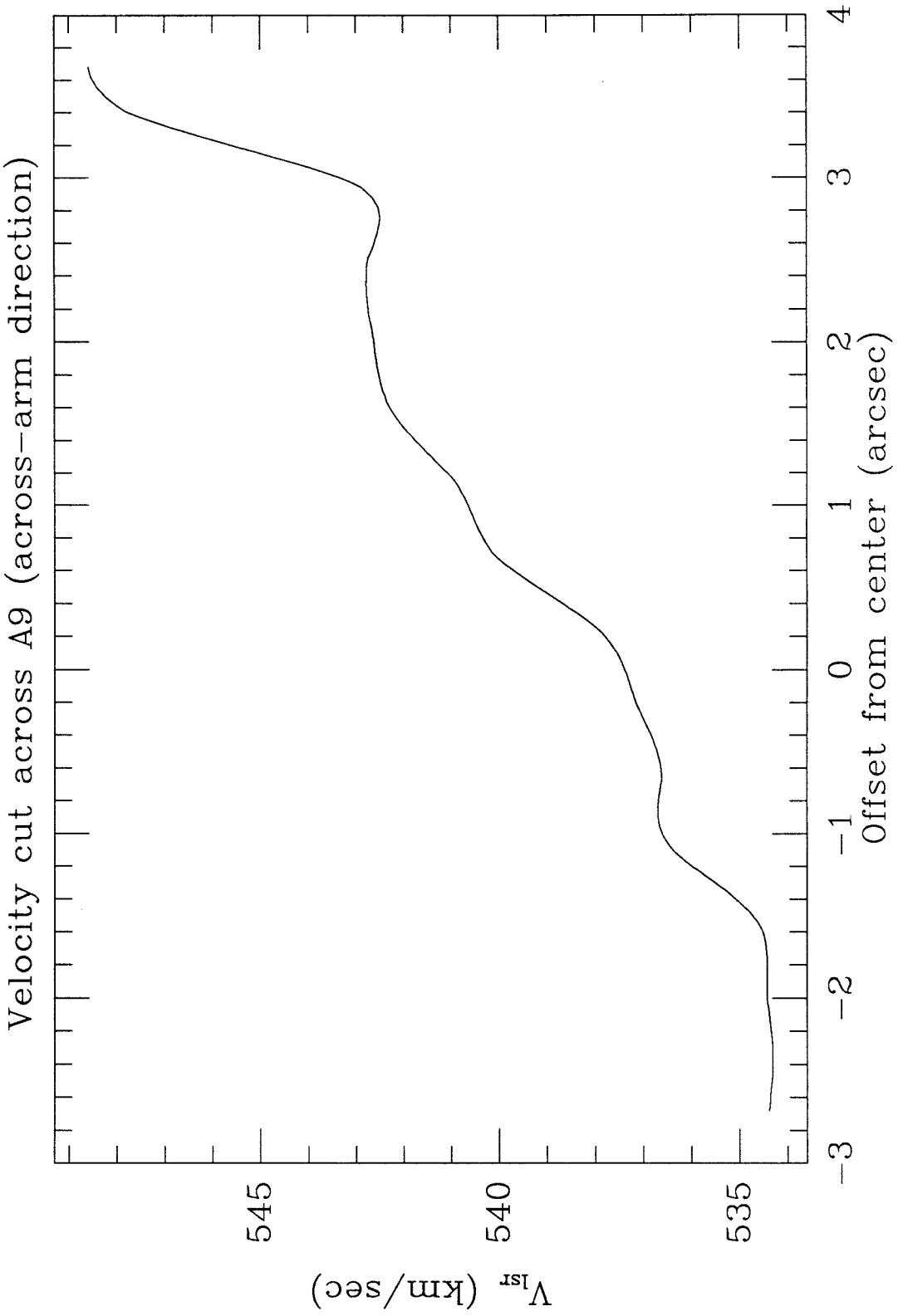
Velocity cut across A9 (across-arm direction)
V_{lsr} (km/sec)
545
540
535
−3
−2
−1
0
1
2
3
4
Offset from center (arcsec)

Figure 3*c*

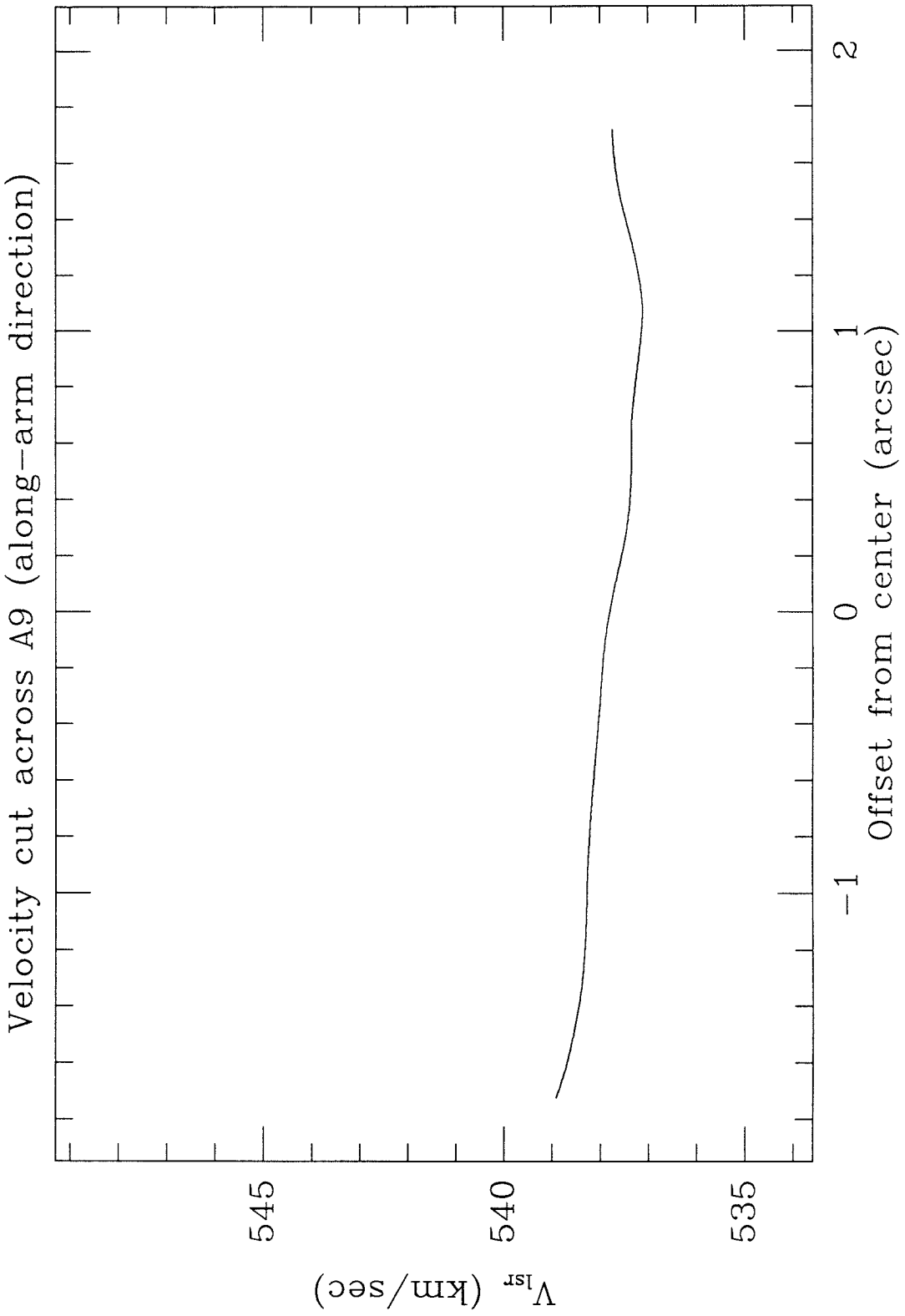
Velocity cut across A9 (along-arm direction)
V_{lsr} (km/sec)
545
540
535
−1
0
1
2
Offset from center (arcsec)

Figure 3*d*

CHAPTER 4

Star Formation and the Distribution of HI and Infrared Emission in M51

Abstract

HI, infrared, CO, Hα and B-band observations of M51, the prototypical grand-design spiral galaxy, are used to study the consequences of star formation for the distribution of HI and dust. Using the VLA map of 21-cm emission, the OVRO CO mosaic map, and an Hα image, we carry out new tests of the idea of Tilanus and Allen that the HI is largely a photodissociation product in star-forming regions. We confirm that the HI spiral arms are generally coincident with the HII region arms, and offset downstream from the CO arms. The radial distributions of total gas, Hα and HI surface density have a simple explanation in the dissociation picture. The distributions also demonstrate how the surface density of HI might be related to the star formation efficiency in molecule-rich galaxies. The large width of the HI regions along the arms compared to that of the HII regions can be understood in terms of a simple calculation of the expected size of an HI region associated with a typical HII region. The longer lifetime of the stars producing dissociating radiation *vs.* those producing ionizing radiation and the relatively long molecule formation timescale will also contribute to the greater width of the HI arms if stars are continuously forming on the arms. The lack of detailed coincidence of the HI and HII regions

along the inner arms has a variety of possible explanations within the dissociation scenario.

We carry out two simple tests to probe the origins of the *IRAS* emission in M51. First, we find that the infrared excess (IRE) of M51 is 24, suggesting that a substantial fraction of the infrared emission arises from dust heated by photons which *do not* originate in massive star-forming regions. Second, radial cuts through the *IRAS* bands show that at 12, 25 and 60 μm, the arm-interarm contrast of the *IRAS* emission is substantially less than that of the Hα emission, convolved to matching resolutions, providing further evidence for the above explanation and for the existence of a broadly distributed dust component. Deconvolved *IRAS* maps have improved resolution but do not change this finding.

Subject headings: galaxies: interstellar matter – galaxies: individual (M51) – stars: formation – infrared: sources

I. Introduction

Great advances in our understanding of how spiral density waves organize atomic and molecular gas in galaxies and how they therefore relate to ongoing star formation have been made possible in the past few years with the advent of high-resolution centimeter- and millimeter-wave interferometers. M51 has been a popular target for such studies because of its proximity (9.6 Mpc; Sandage and Tammann 1975), nearly face-on aspect, strong spiral structure, and molecule-rich ISM (about 90% of the ISM is molecular; Scoville and Young 1983). Observations of the ISM of this galaxy have been recently reviewed by Rand and Tilanus (1990).

In two previous papers (Vogel, Kulkarni, and Scoville 1988, hereafter VKS; Rand and Kulkarni 1990a, hereafter RK) we have presented mosaic maps of CO (1–0) emission from M51 at 8" resolution made with the Millimeter Interferometer of the Owens Valley Radio Observatory (OVRO). We detected molecular spiral arms which are well aligned with the dust lanes but offset upstream from the HII region arms (see Figure 1*a*,*b*), implying that the onset of massive star formation occurs several million years after the peak compression of the molecular gas. The spiral arms represent about one-third of the total emission measured with single dish instruments. The tangential and radial velocity shifts predicted by density wave theory as the gas is being compressed can be clearly seen where the arms cross the major and minor axes of the galaxy. Using Hα emission as a tracer of the massive star formation rate, we found that the star formation efficiency is higher on the arms than between the arms, implying that the density wave is triggering

excess star formation from the compressed gas. This result has been confirmed in single-dish CO observations (Lord and Young 1990). The molecular arms contain well-organized structures which we termed Giant Molecular Associations (GMAs). The typical mass of a GMA is 3×10^7 $M_\odot$. GMAs are also found between the arms. The on-arm GMAs show a rough equality of virial and CO-flux based masses, while the interarm GMAs have virial masses several times their CO-flux based masses. The CO (1–0) spectra of the GMAs show that they typically consist of one to five velocity components. The GMAs may form through collisional agglomerations of pre-existing smaller clouds or by gravitational instabilities in the molecular gas (see Rand and Kulkarni 1990b). The interarm GMAs may owe their existence to a weak, secondary compression of the density wave.

VKS and RK examined how the density wave organizes the molecular gas and discussed the consequences for star formation from analysis of Hα images. In this paper, we further examine the "back reaction" of star formation on the ISM of M51 by considering, in conjunction with molecular data and an Hα image, the distribution of atomic gas and infrared emission from two new data sets: the VLA map of 21-cm emission by Rots *et al.* (1990, hereafter RBHAC), and the *IRAS* (Infrared Astronomical Satellite) pointed observations of M51 (Rice *et al.* 1988).

Recently, evidence has been presented that in the molecule-rich galaxies M51 (Tilanus and Allen 1989, hereafter TA) and M83 (Allen, Atherton, and Tilanus 1986) HI is predominantly a product of dissociation of H_2 in star-forming regions. If the detected HI were distributed in the same way as all the gas we would expect

to see the peak of the 21-cm emission along the dust lanes, where the highest compression of the gas is occurring. However, the observations show that in these galaxies HI is concentrated downstream from the dust lanes but coincident with the HII region arms. TA estimate that in M51 approximately 10% of the molecular gas is dissociated in star-forming regions. Compared to the WSRT map of TA, the VLA map of RBHAC has higher angular resolution (8" *vs.* 12" x 18") and sensitivity. In this paper we use this map, along with our Hα and *B*-band images, CO data (see RK) and published single-dish CO data to carry out further quantitative tests of the dissociation scenario. In particular, we examine whether *a)* the radial distributions of total gas, Hα and HI, *b)* the small-scale structure of the HI emission and *c)* the detailed spatial relationship between the HI and HII regions can be explained in this picture. We find that the new VLA map provides further evidence in favor of the dissociation scenario.

Radiation from young stars not only ionizes HI and dissociates H_2 but also heats the interstellar dust. The infrared emission from dust allows yet another probe of the back reaction of star formation on the ISM. In the second part of this paper, we use the *IRAS* pointed observations of M51 to study the distribution and origins of the infrared emission. Recent work on the *IRAS* spectra of our Galaxy and other spirals (Cox and Mezger 1987; Lonsdale-Persson and Helou 1987; Helou 1986) has led to a picture for the dust emission in which the 12 μm emission is dominated by very small grains transiently heated by the interstellar radiation field (ISRF; there may also be a contribution from OH/IR stars), the 25 and 60 μm emission is from

warm dust in star-forming regions but may also have a substantial contribution from generally distributed dust heated by the ISRF (or intermediate-mass young stars), and the 100 μm emission is dominated by relatively large grains heated by the ISRF. The very small grains are expected to be destroyed in star-forming regions (Puget, Léger, and Boulanger 1985), so little 12 μm emission is expected from such regions. Broadly distributed dust heated by the ISRF has come to be referred to as "cirrus" (Low *et al.* 1984). We use this term here to refer to both dust heated by the ISRF and by non-ionizing young stars.

We attempt to interpret the infrared emission of M51 in terms of these two-components: dust in star-forming regions and cirrus. Our goal is to understand the origins of the *IRAS* emission in M51. In particular, we carry out two tests designed to distinguish between infrared emission arising from massive star-forming regions, and emission from a cirrus component. We first calculate the "Infrared Excess" (IRE; Mezger 1978), a dimensionless quantity which provides a measure of the fraction of the infrared flux which arises from dust heated by photons which originate in massive star-forming regions. We then compare cuts through the *IRAS* maps with cuts through Hα and B-band CCD images convolved to the *IRAS* resolutions to determine whether the infrared emission is distributed in the same way as the optical line emission from star-forming regions. If the infrared emission shows a reduced concentration to the spiral arms compared to the Hα emission, then one can conclude that a fraction of the infrared emission arises from generally distributed

dust. We find that the results of both these tests indicate that a substantial fraction of the emission detected by *IRAS* is in fact in a cirrus component.

II. HI and Dissociation

a). Radial Distributions

The radial distributions of the total gas, Hα and HI surface density are shown in Figure 2. To estimate the total (H_2 and HI) gas surface density, we have used the FCRAO CO data at 45" resolution by Lord and Young (1990) and Scoville and Young (1983). To convert the CO emission to molecular column density, we assume the Galactic conversion factor of $\alpha = 3 \times 10^{20}$ mol cm^{-2} (K km s^{-1})$^{-1}$. A rough Hα calibration was carried out by comparing our measured fluxes for nine HII regions in the inner disk to the published values of van der Hulst *et al.* (1988, hereafter HKCR). The scatter in this comparison is 20%, which is sufficiently low for our purposes. We corrected for extinction by assuming a mean value of $A_V = 2$ mag from HKCR. These authors found no significant dependence of A_V on galactocentric radius. The total gas profile shows a roughly exponential fall-off with radius, while the Hα profile shows a similar fall-off, but with a pronounced enhancement at $R \approx 150$" (the Hα intensities may not be reliable for the region $R < 25$": the continuum images used for the continuum subtraction were saturated over parts of this region). The HI profile shows a central hole ($R \lesssim 30$"), a relatively flat inner disk ($30" \lesssim R \lesssim 100"$), a large enhancement in the outer disk peaking at $R \approx 150$", and finally a falloff at $R \gtrsim 175$". This profile can be understood

in terms of the theory of Federman, Glassgold, and Kwan (1979), who consider the shielding of a molecular cloud to dissociating radiation by an outer envelope of HI. In this picture, the thickness of the dissociated envelope depends on the ratio of the dissociation and formation rates of H_2. This ratio has been shown by Hollenbach, Werner and Salpeter (1971) to depend on a power of G/n, where G is essentially the flux of dissociating radiation times the cross section in the Lyman bands of H_2, and n is the density of the gas. Here we are considering the creation of dissociation regions in massive star-forming regions by energetic photons from young stellar associations. Since Hα traces the high-mass stars it should also trace the dissociating radiation. The flat HI profile in the inner disk and the large enhancement in HI around $R \approx 150$" can then be understood in terms of this simple balance between molecule formation and dissociation in star-forming regions. In the inner disk at $R \lesssim 100$", the Hα and total gas profiles show a similar falloff with radius, so that the balance between dissociation and formation changes little with radius and a constant column density of HI is produced. At $R \approx 150$", the "excess" of dissociating radiation in the outer arms relative to the gas density tips the scales in favor of dissociation, and thus more HI is produced. Beyond $R = 170$", the Hα enhancement ends, and the HI returns to roughly its inner disk value. The radial distributions therefore support the dissociation picture.

An interesting consequence of such an interpretation for the origin of the HI is that, since the Hα emission traces the star formation rate, the HI surface density is actually related to the star formation *efficiency* (the star formation rate per unit

gas mass). The possibility of using HI as an indicator of star formation efficiency in molecule-rich galaxies such as M51 and M83 should be pursued further.

b). The Small-scale Structure

In Figure 1*c,d* we show the VLA HI map of RBHAC overlaid on our CO map and Hα image. It is clear that compared to the CO distribution there is enhanced HI emission in the outer ($R \gtrsim 100$") arms, although the azimuthally averaged surface density of HI never contributes more than about 25% of the total gas surface density (Figure 2). Comparing with the OVRO CO map, we find a typical ratio of H_2 to HI column density in the inner arms of about 16. Therefore the new VLA map confirms the low HI/H_2 ratio on the arms, and the conclusion of TA that only a small fraction of the molecular gas is dissociated.

Figure 3 shows cuts across typical gaseous features on the NW arm: a giant HII region (No. 83 of Carranza, Crillon, and Monnet [1969]), an HI emission feature 30" south of this HII region from the 13"-resolution VLA map, and a cut across the CO (2–1) arm measured by hand from the contour map of Garcia-Burillo and Guélin (1990) at 12" resolution. The purpose of this figure is to give a rough indication of the low ionized and neutral gas surface densities relative to the molecular gas surface density. The peak Emission Measure of 4000 pc cm^{-6} corresponds to a surface density of about 10 $(\phi/0.1)^{1/2}$ $M_\odot$ pc^{-2}, where ϕ is the filling factor of the ionized gas. This surface density is found assuming a full-thickness of 250 pc for the ionized gas, a temperature of 10^4 K, and a visual extinction of $A_V = 3.3$ mag, the

value measured for this HII region by HKCR. Giant HII regions in nearby galaxies tend to have low filling factors, with perhaps 0.02 being a typical value (Kennicutt 1984). The 13"- resolution version of the VLA data was used because of its better sensitivity to interarm emission relative to the 8" version. The CO (2–1) brightness temperatures were converted to surface densities using the observed CO (2–1)/ CO (1–0) ratio of 0.7 from Garcia-Burillo and Guélin (1990) and assuming the above value of α. The figure demonstrates that only a small fraction of the molecular gas is dissociated or ionized.

Table 1 gives typical arm and interarm surface densities for the inner disk. The Hα image was convolved to 13" resolution for the purpose of calculating these numbers to allow a comparison at matched resolutions. Because of scattering and reflection problems in the point-spread function of the reimaging camera used to obtain the Hα image, the Hα arm-interarm surface density contrast may be somewhat reduced from its true value. A filling factor of $\phi = 0.1$ is assumed for the ionized gas. These numbers again demonstrate how little molecular gas is dissociated or ionized on the arms, and that the interarm gas is almost completely molecular.

From the VLA HI map (Figures 1*c,d*) we note the following:

i) Over large sections of the inner ($R \lesssim 100$") arms (see Figure 1*c*) an offset can be seen between the centroids of the HI arms and CO arms, but the broad HI emission in many places extends upstream to the CO arms and often even *further* upstream into the pre-compression zone.

ii) The inner HI arms show a patchy structure and are broader than the Hα arms. The typical diameter (FWHM) of the bright HII regions in the inner arms is 5.5" or 250 pc, while the typical diameter of the HI arms is about 17" or 800 pc, although there is much variation in the latter quantity.

iii) While parts of the inner arms show a simple morphology in which HI envelopes exist around HII regions, there are many HI clouds which have very little Hα emission associated with them, as in M83 (Allen, Atherton, and Tilanus 1986). Figure 4 is a close-up view of an arm segment which shows the detailed spatial correspondence of the CO, 21-cm, and Hα emission.

iv) There are a few HI clouds in the interarm regions, where there is also very little or no Hα emission. It should be pointed out that the total mass of HI in the VLA 8"-resolution map is 2×10^9 $M_\odot$, which is only 40% of the mass found in the single-dish observations of Appleton, Foster, and Davies (1986) and Rots (1980). In fact, RBHAC report that in their lower resolution VLA observations, there is broadly distributed HI between the arms at the level of about 10^{20} cm^{-2} which has been missed in the 8" map. This interarm emission may not make up the entire missing flux, but the fact that the total flux is well below the single-dish value indicates that some emission has been resolved out in the 8" map.

We now explore whether these diverse observational results can be explained in the framework of the dissociation model.

i) The HI-CO Offset

First, the fact that the HI arms are, like the Hα arms, offset downstream from the CO arms supports the idea that the HI is produced in star-forming regions. If the HI arms seen in the VLA map simply consisted of gas compressed by the density wave, then we would expect the HI emission generally coincident with the CO emission. This is not the case, although in some places the HI arms do overlap the CO arms, sometimes even extending upstream of the CO emission. In the dissociation model, this latter fact would imply that a small fraction of the molecular gas is dissociated by downstream star formation *before* it reaches the zone of peak compression.

ii) The HI Arm Width

We now address the issue of whether the greater width of the HI arms compared to the Hα arms in the inner disk can be explained by a simple calculation of the expected size of an HI region associated with a typical giant HII region along the arms. Certainly the patchiness of the inner HI arms would be expected if each emission feature corresponded to a dissociated region around a young stellar cluster or clusters.

In the Appendix, we calculate the expected sizes of the HII and HI regions along the inner arms of M51 using the observed Hα luminosity of a typical inner-arm giant HII region to estimate the ionizing photon rate. The effects of dust opacity are included in the calculation by using the HII region extinctions published by HKCR. The gas is considered to consist of dense and diffuse components, with a

varying fraction in each. We find that almost all of the HI surface density in the dissociation features is contributed by the diffuse medium. With our simple model we can reproduce HI regions with diameters of about 500 to 700 pc, in reasonable agreement with the observed sizes, but slightly underestimating them for most values of the free parameters in the calculation. However, the calculation ignored any clumpiness or porosity in the diffuse medium, which would allow dissociating photons to travel further from their sources. The characteristic size of the HI features, therefore, has a reasonable explanation in the dissociation picture.

A perhaps surprising result from the calculation in the Appendix is that we find from two independent methods of estimating the dust surface density that the dust-to-gas ratio (which is a necessary number for calculating the H_2 formation rate) is about equal to the Galactic value. This near equality of dust-to-gas ratios in M51 and the Galaxy may be a cause for concern given that the typical metallicity in the inner disk of M51 is three times the Solar value (Pagel and Edmunds 1981), so that one might expect a higher dust abundance.

The H_2 reformation timescale, $(Rn_H)^{-1}$, where R is the molecule formation constant (units cm^{-3} s^{-1}), and n_H is the total gas density, is about 10^8 yr. If the gas is clumped with filling factor ϕ, this timescale will be reduced by a factor of ϕ. The timescale can be compared to the time between arm passages, $\pi(\Omega_{rot} - \Omega_P)^{-1}$ (where Ω_{rot} is the rotational angular velocity and Ω_P is the pattern speed of the density wave), to see whether a steady state between dissociation and reformation can be maintained. Tully (1974b) determined a pattern speed, scaled to a distance

of 9.6 Mpc, of 37 km s^{-1} kpc^{-1}. The rotation curve is essentially flat at $v_{rot} = 210$ km s^{-1} (Tully 1974a; Scoville and Young 1983). With these parameters, the time between arm passages is 5×10^7 yr at 2 kpc from the nucleus, and 2×10^8 yr at 4 kpc. Thus it is plausible that the dissociated gas can reform into molecules before the next arm passage such that a steady state is maintained if the gas is moderately clumpy. The HI features on the arms should be rapidly diluted as they move off the arms by the expansion and shear of the underlying flow.

As mentioned above, our calculation may not be able to fully explain the characteristic HI arm width. Other effects may contribute to the greater HI arm width. Since the hotter stars evolve more rapidly, the ionizing radiation from a stellar cluster will disappear faster than the dissociating radiation, to which B and A stars can contribute significantly. Thus, if young stellar clusters are continuously being formed in the arm, then the zone over which dissociating stars are found will be broader than the zone over which ionizing stars are found. The dissociation zone will also be broader than the typical size of a *single* HI region corresponding to a giant HII region. Some of the HI regions, then, may be due to dissociation by multiple clusters formed at different times on the arms. Furthermore, the relatively long molecule-reformation timescale implies that the 21-cm emission will persist for a significant time after the dissociating radiation disappears, leading to further downstream extension of the dissociation regions. The width of the zone due to these two effects can be estimated as follows. From simple blackbody approximations, we find that the stars that dominate the dissociating flux are late O and early B

stars, which have main sequence lifetimes of $\tau_{MS} \approx 1 - 2 \times 10^7$ yr. For $\phi \sim 0.1$, the reformation timescale is about 3×10^7 yr. The component of circular velocity perpendicular to the arms is approximately $(\Omega_{rot} - \Omega_P) R \sin i$, where i is the pitch angle of the spiral arms and R is the galactocentric radius. Tully (1974b) measured i to be 18.5°. Therefore, at a distance from the nucleus of $R = 3$ kpc, the width perpendicular to the arms of the zone where dissociating stars should be found, assuming that they are all formed at about the same spiral phase, is 0.7 "τ_{MS} (Myr) $\approx 7 - 13$". The width perpendicular to the arms corresponding to the reformation timescale is ~ 21". Hence the width of the HI arms is likely due in part to these effects. However, these numbers are upper limits since the orbits in a density wave compression bend to become more aligned with the spiral pattern compared to purely circular orbits, so that the effective $\sin i$ is reduced. The width expected from these effects is larger near the Inner Lindblad Resonance of the wave and smaller near corotation.

iii) Poor Detailed Spatial Coincidence of HI and HII Regions

It remains to be explained why the detailed spatial coincidence of HII and HI regions is poor, particularly in the inner regions where the existence of the density wave has been established. One possibility, still within the above dissociation scenario, is that some of the HI clouds on the arms are simply regions of low total gas density compared to the typical on-arm density. In terms of the Federman, Glassgold, and Kwan (1979) model, for a given flux of radiation, the HI column

density is high in these regions because the molecule formation timescale is relatively long. In other words, G/n is relatively high. However, a visual inspection of Figures 1*c* and 1*d* shows that HI regions not associated with Hα emission are sometimes associated with CO emission, and sometimes not, indicating that the HI is not necessarily found in regions of low total gas density.

We prefer the following effects as the more likely reasons for the lack of correlation. First, as mentioned above, the ionizing radiation from a stellar cluster disappears faster than the dissociating radiation because of the longer characteristic lifetime of the stars providing the dissociating radiation. Also, the molecule reformation timescale is much longer than the recombination timescale, so the 21-cm emission will persist well after the dissociating radiation disappears, whereas the ionized gas will quickly recombine once the ionizing radiation disappears. These effects would not only lead to a lack of correlation but would also explain why some HI regions extend preferentially downstream from the HII regions (Figure 1*d*). Another possible contributor could be the inevitable supernovae, which will clear out the immediate vicinity of the cluster, where the Hα emission is concentrated, much more effectively than the regions where the HI is found, much further away from the cluster center. The timescale for this clearing process may be comparable to the age of $\sim 10^7$ yr inferred by Brinks and Bajaja (1986) for the $\sim$ 500 pc diameter HI holes they found in M31. Finally, if some clusters form without many OB stars, they may produce HI regions with little Hα emission.

iv) Interarm HI

The surface density of the smoothly distributed interarm component is 10^{20} cm^{-2}. This component presumably consists of diffuse gas and dense cloud envelopes which are dissociated either by the ISRF or interarm star formation. The few interarm clouds compact enough to be seen in the 8"-resolution map do not have much associated Hα emission. They may be dissociation regions around stellar clusters with few OB stars.

III. Infrared Properties

The aim of this analysis is to understand whether or not the infrared emission in M51 arises purely from star-forming regions. Figure 5 shows the *IRAS* maps of M51, while Table 2 lists some of the global properties of the infrared emission. T_W and T_C in Table 2 are the resulting temperatures in a two component fit to the *IRAS* data by Rice *et al.* (1988). T_C is $\lesssim 1\sigma$ above the mean value of all large optical galaxies modelled in this way by Rice *et al.* (1988).

Our first diagnostic is the dimensionless IRE, which is defined as the total *IRAS* flux (νf_ν summed over the four *IRAS* bands, although some authors use the 60 and 100 μm bands only) divided by the Lyman continuum flux. Mezger, Smith, and Churchwell (1974) calculate the infrared emission expected from an HII region for a given ionizing photon rate, and show how this photon rate can be estimated from the thermal flux density. The IRE is calculated as follows (Rice *et al.* 1990):

$$\mathrm{IRE} = 9.4\ (\mathrm{Hz}^{-1})\ \frac{F_{IRAS}(10^{-13}\mathrm{Wm}^{-2})}{S_{21}(\mathrm{mJy})} \qquad (1)$$

where F_{IRAS} is the total *IRAS* flux and S_{21} is the thermal continuum flux at 21 cm. The IRE is defined such that a value of unity means that all of the infrared emission can be explained as arising from dust heated by Ly-c photons which have been absorbed and degraded to Lyα by gas. An IRE greater than one implies that some of the infrared emission arises from dust heated directly by photons from H-ionizing stars and from dust heated by stars which provide little ionization.

The typical IRE found by Myers *et al.* (1986) for Galactic HII regions is 6. It is possible, however, that their balloon observations may have missed some of the shorter wavelength infrared emission since they employed only two detectors at 150 μm and 350 μm. However, Scoville and Good (1989), using all four *IRAS* bands to calculate the IR luminosity, found IREs ranging from 3 to 7 for four HII regions in the M17 and W51 regions. Furthermore, the *IRAS* study of M33 by Rice *et al.* (1990) showed that ten well-isolated HII regions with measurable IREs have values in the range 4–9 (the mean IRE over the whole galaxy is 14). Hence, these studies all indicate a typical IRE of 6 for HII regions. For a galaxy, an IRE well in excess of the value for Galactic HII regions indicates a substantial amount of infrared emission *not* due to dust heating by photons which originate in massive star-forming regions, but rather due to a "cirrus" component (see the Introduction).

In order to calculate the IRE, we need an estimate of the thermal continuum flux at 21 cm. Thermal-nonthermal flux separations have been carried out independently by Tilanus *et al.* (1988) and Klein, Wielebinski, and Beck (1984), with both studies finding a thermal flux at 21 cm of about 75 mJy. Thus the IRE

of M51 is about 24, which is much higher than the typical value for Galactic HII regions, indicating that a large fraction of the infrared luminosity arises from a cirrus component. One way to escape this conclusion is to invoke a much higher dust-to-gas ratio in M51, such that in the HII regions of M51, dust grains compete more effectively for ionizing photons than HI atoms relative to Galactic HII regions. However, we show in the Appendix that the dust-to-gas ratio is not significantly different from the Galactic value. Another possibility is that some fraction of the energetic photons escape from the HII regions in M51 and is available to power a cirrus-like dust component and perhaps a diffuse, ionized medium. The thermal radio emission from the diffuse ionized gas may be too weak to detect, while the dust emission may be significant. However, to explain in this way the IRE of M51, which is fully four times the typical HII region IRE, almost all of the energetic photons responsible for the IR emission would have to escape from each HII region and be absorbed by generally distributed dust. Given that the typical visual extinction within the giant HII regions of M51 is about 0.5 mag (see the Appendix), the extinction at about 1000 $\AA$ is about 2.2 mag, assuming the Galactic extinction curve. Although some of this extinction may be due to scattering and not absorption, it is unlikely that almost all of the photons around 1000 $\AA$ escape the HII region.

Our second test involves comparing the arm-interarm contrast in the *IRAS* maps with that in our Hα image convolved to the resolutions of the *IRAS* maps. The beam of the *IRAS* detectors is such that the resolution along the in-scan direction (P.A. $\approx 45°$ for M51) is significantly better than that along the cross-scan direction.

The in-scan resolution of the *IRAS* observations is sufficient for the measurement of an arm-interarm contrast at 12, 25 and 60 μm. The in-scan and cross-scan resolutions are listed in Table 3. If all of the infrared emission arises in star-forming regions, we would expect to see the same arm-interarm contrast in the infrared maps as in our Hα image.

Cuts in the in-scan direction of the original 12, 25 and 60 μm maps are presented in Figure 6 along with cuts through Hα and B-band images which have been convolved to the *IRAS* resolutions using the elongated *IRAS* beams. Ongoing star formation is traced by the Hα emission while the ISRF is best traced by the B-band light. The 100 μm cut is not shown because at the low resolution of the 100 μm data no spiral structure can be seen in either the map or the cut.

Features corresponding to the nuclear region and the outer NE and SW spiral arms can be seen in all of the cuts in Figure 6. The arm-interarm contrast in the 12 μm cut is slightly lower than that at 25 μm. It is clear that the arm-interarm contrast in the *IRAS* cuts in all three bands is lower than in the Hα cuts but higher than in the B-band cuts. This result implies that in all three bands there is emission both from dust in star-forming regions and cirrus. For the warm dust (25 and 60 μ m) this is not too surprising given the above discussion of the IRE. This result is also understandable for the 12 μm emission if it is dominated by emission from very small grains which are destroyed in star-forming regions.

Deconvolved images of the *IRAS* pointed observations (see Neugebauer *et al.* 1984) of M51 at all four *IRAS* bands were produced at the Infrared Processing

and Analysis Center (IPAC) using a Richardson-Lucy deconvolution algorithm (Aumann, H. H., private communication). We examined maps at various stages of the deconvolution procedure and chose ones for the analysis below based on the level of spurious structure introduced in the blank regions around M51 by the deconvolution process. We judged that maps produced using more than 5 iterations at 12 and 25 μm, and 20 iterations at 60 and 100 μm, were possibly unreliable due to this rather subjective criterion. The deconvolved maps using the above numbers of iterations are shown in Figure 7, and the achieved resolutions are listed in Table 3. Cuts were made through these images as before, and are shown in Figure 8, along with Hα and B-band cuts at matched resolutions. Increases in the arm-interarm contrast can be clearly seen in the 12, 25 and 60 μm maps, but in the 100 μm map, the companion is only partially resolved and the outer arms remain unresolved. The 100 μm cut (not shown) shows no evidence for spiral structure.

The smoothness of the 100 μm map and cut is surprising when compared to Smith's (1982) map at 170 μm with 49" resolution (his Figure 2) made with the Kuiper Airborne Observatory. This map, at only slightly better resolution, shows clear spiral structure in the NE and SW. The longer wavelength of his observation should guarantee a smaller contribution to the emission from dust in star-forming regions, since this wavelength traces colder dust, thus reducing the expected contrast relative to that at 100 μm. The likely reason for this discrepancy is that the original 100 μm map had insufficient resolution to detect any spiral structure at all, even in

the in-scan direction. Naturally, the deconvolution procedure would not bring out any spiral structure if there were none in the original data.

Figure 8 shows the same ordering of cuts by arm-interarm contrast as in Figure 6, and thus point to the same conclusion as that drawn from the original maps: there are at least two components to the infrared emission in the 12, 25 and 60 μm bands.

The deconvolution we have presented is by no means unique. For comparison, we show in Figure 9 a deconvolution of the 60 μm survey data by W. N. Weir (personal communication) using the MEMSYS software (based on the Maximum Entropy Method). This deconvolution method, unlike the Richardson-Lucy algorithm, does not assume that the point-spread function is constant over the field. The achieved resolution, although it almost certainly varies over the map, is obviously much better than that of Figure 7*c*, and a higher arm-interarm contrast in the outer arms can be seen. Unfortunately, a comparison of this map with the Hα image would be perilous since the resolution varies over the map. It is therefore not clear how to perform the necessary convolution of the Hα image before the comparison. Compared to the pointed observations, the *IRAS* survey data unfortunately has a worse problem with striping in the in-scan direction, and a stripe can be seen running through the center of M51 in Figure 9 which confuses the interpretation.

We emphasize that our conclusions which are based on differences in arm-interarm contrast between the *IRAS* and Hα images do not depend on the reliability

of the Richardson-Lucy deconvolution since the differences can be seen from the cuts through the *original IRAS* maps (Figure 6).

We can make a very rough estimate of the fractions of infrared emission which are associated with star-forming regions and ISRF-heated cirrus. Since the emissivity per dust grain of the cirrus component should be roughly proportional to the ISRF intensity, and since the cirrus arises from dust which is associated with the general gas distribution, the profile of cirrus emission should roughly resemble the product of the B-band profile and the profile of total gas surface density. The emission profile of dust in star-forming regions should roughly resemble the Hα profile. For the construction of the total gas profile the resolution of the FCRAO map is insufficient. We therefore use the new map of CO emission at 15" resolution from the Nobeyama 45-m and convolve it to the *IRAS* resolutions. Using this simple model and the profiles shown in Figure 6, we estimate that at 60 μm, 75% of the emission comes from the cirrus component, while 25% of the 25 μm emission and 75% of the 12 μm emission is due to cirrus. For M33, by way of comparison, a more careful decomposition by Rice *et al.* (1990) showed that cirrus accounts for 50% of the 12 and 60 μm emission, and 10% of the 25 μm emission. For both these galaxies then, the 25 μm band contains the highest fraction of emission from star-forming regions.

The results from these two tests imply that a direct interpretation of the *IRAS* luminosity of M51, either the total *IRAS* luminosity or L_{FIR} alone, in terms of a star formation rate, would be spurious. The same conclusion has been reached

in studies of many other nearby spirals, where the IRE's range from 13 to 24 (M33 [Rice *et al.* 1990]; M101 [Beichman *et al.* 1987]; and NGC 4565, NGC 891 and NGC 5907 [Wainscoat, de Jong, and Wesselius 1987]). Furthermore, studies of M31 (Walterbos and Schwering 1987) and the Galaxy (Bloemen, Deul, and Thaddeus 1990) have shown that most of the FIR emission arises from cirrus in these galaxies. Finally, Bothun, Lonsdale, and Rice (1989) found for most spiral galaxies in an optically selected sample – using f_{60}/f_{100} as a diagnostic of dust heating sources along with a simple dust-heating model – that dust in star-forming regions and cirrus are both important contributors to the total FIR luminosity.

The position of M51 in the color-color diagram of Helou (1986) confirms the above conclusion. In his Figure 2, M51 lies below the line where half of the infrared emission derives from star-forming regions, implying that the cirrus contributes the majority of the emission.

These results may not be surprising given that the galaxy is very gas-rich. The total mass of gas has been estimated by Scoville and Young (1983) to be 1.2×10^{10} $M_\odot$, of which 9×10^9 $M_\odot$ is in molecular form. In comparison, Scoville and Young estimate a dynamical mass of about 10^{11} $M_\odot$, so that the gas accounts for fully 13% of the dynamical mass. The high SFR in M51 implies significant dust heating in star-forming regions, but should also imply a relatively intense ISRF, since, for a normal IMF, there will be copious production of intermediate-mass stars which dominate the ISRF. This combination of a rich ISM with an intense ISRF could be the reason for the significant cirrus component.

Throughout this analysis, we have used the term "cirrus" to refer to emission from dust outside of regions of high-mass star formation. It should be noted, however, that Cox, Krügel, and Mezger (1986) conclude that non-ionizing young B and A stars could heat dust in star-forming regions to 30-40 K and provide some of the emission detected by *IRAS* in the Galaxy. It has been suggested for our Galaxy (see Scoville and Sanders 1988), although there is no direct evidence for M51, that B and A star formation is more uniformly distributed than O star formation. If this is the case in M51, then such an infrared emission component from regions of low-mass star formation may have a spatial distribution more like the cirrus component and thus be observationally indistinguishable from cirrus based on the spatial distribution of far infrared (FIR) emission alone. It is therefore worth keeping in mind that radiation from "generally distributed dust" may have more than one origin. However, regardless of the nature of the cirrus, our tests have shown that the infrared emission cannot be accounted for by high-mass star formation alone.

An important consequence of the main conclusion of this section is that infrared emission cannot be used to independently test the hypothesis of density wave triggering of star formation unless the component of emission from star-forming regions can be effectively isolated, both spatially and spectrally. One should keep in mind that the arms which have been resolved or partially resolved by *IRAS* are beyond the radius of corotation of the density wave and are probably tidal arms generated by the passage of the companion (Tully 1974a; Elmegreen, Elmegreen, and Seiden 1989). Therefore, even the deconvolved *IRAS* images do not begin to resolve

the density wave arms and hence cannot be used to test density wave triggering of star formation.

IV. Conclusions

We have used VLA HI data and *IRAS* maps of M51 in an attempt to further understand the consequences of star formation in this molecule-rich galaxy with a strong density wave. From the HI map, we find compelling evidence which favors the idea that the HI is almost entirely a product of dissociation of H_2 in star-forming regions. The radial distribution of HI as well as the characteristic size of the emission features along the arms have simple explanations in the dissociation scenario. The lack of detailed correlation between HI and HII regions has a variety of possible causes. HI between the arms may be dissociated by the ISRF or by interarm star formation. There are indications that the gas-to-dust ratio is about equal to the Galactic value.

The IRE and the reduced arm-interarm contrast of the *IRAS* maps compared to the Hα image both indicate that a substantial fraction of the infrared emission detected by *IRAS* does not arise in star-forming regions, but rather from dust associated with generally distributed gas ("cirrus"). Given the high surface density of gas in M51, this result is perhaps not too surprising. The same conclusion has now been drawn for several nearby galaxies. An important implication of this result is that it will be difficult to interpret the FIR emission from M51 in terms of recent star formation, and thus to use FIR emission to check the hypothesis of density wave triggering of star formation. Regardless of whether a reliable separation of

emission components can be done, the resolution of the *IRAS* maps is insufficient to resolve the inner, density-wave spiral arms.

Acknowledgements

We are deeply indebted to A. Rots for providing us with the VLA map of HI emission. We thank N. Nakai for allowing us to use the Nobeyama 45-m CO map in the discussion of the *IRAS* emission. We are grateful to N. Z. Scoville and E. S. Phinney for helpful comments. We thank W. N. Weir for his deconvolution of the 60 μm *IRAS* image, and we acknowledge the Maxent90 Image Reconstruction Contest and the Laboratory for Space Research in Groningen, the Netherlands, for permission to use this image. This work was partially supported by *IRAS* grant NAG 5-1164. The OVRO Millimeter Interferometer is supported by NSF grant AST 97-14405.

Appendix

We show here through a simplified radiative analysis that the large observed sizes of the discrete HI regions along the inner arms can be understood if they owe their existence to photo-dissociation by the OB associations (as indicated by the giant HII regions) along the arms. These HI regions have FWHM diameters of about 700 pc (when deconvolved from the 8" beam) and peak surface densities of about 20 $M_\odot$ pc^{-2} (see Figure 3).

A typical giant HII region has an extinction-corrected Hα luminosity of 5×10^{39} erg s^{-1} (HKCR), which corresponds to about 3.5×10^{51} ionizing photons per second, or the equivalent of 70 O5 stars (Kennicutt, Edgar, and Hodge 1989). We assume that all photons shortward of 13.6 eV are absorbed by H atoms, while photons with energies between 11.2 and 13.6 eV are available to dissociate H_2 molecules. Using simple blackbody approximations and a Salpeter Initial Mass Function, we estimate that the photon rate in the above energy range for a stellar cluster is about 50% of the ionizing photon rate. We use this ratio for the HI regions of M51.

Dissociation of H_2 occurs by excitation through photon absorption followed by a decay to the ground level with vibrational quantum number $v \geq 14$. Only about 23% of such absorptions lead to a dissociation (Dalgarno and Stevens 1970). We calculate the dissociation rate by the method of de Jong, Dalgarno, and Boland (1980), who consider only photon absorption in the Lyman band, and approximate that all 60 Lyman bands have an identical oscillator strength. The dissociation rate is given by their equation (A1). For the line opacity, we assume the regime

in which photon absorption in the Lorentz wings of the lines dominates. For the ζ Oph cloud, de Jong, Dalgarno, and Boland estimate that this regime pertains for 10^{16} cm$^{-2} \lesssim N_{H_2} \lesssim 10^{22}$ cm^{-2}, hence covering most cases of interest. The line opacity is then given by equation (A4) of de Jong, Dalgarno, and Boland. The dissociation rate is therefore

$$R_D = 2 \times 10^5 I/I_H e^{-2.5\,A_V} N_H^{-1/2} n(\mathrm{H_2}) \qquad \text{(A1)}$$

where I/I_H is the intensity of the radiation field in units of the Habing (1968) ISRF (2×10^{-8} photons cm^{-2} s^{-1} Hz^{-1} at 1000 Å), A_V is the visual extinction, N_H is the column density of H atoms, and $n(\mathrm{H_2})$ is the number density of molecules. The radiation field intensity, I, is readily calculated from the dissociating photon flux, geometrically diluted for the radius of interest.

The molecule formation rate is given by

$$R_F = R n_H n(\mathrm{HI}) \qquad \text{(A2)}$$

where n_H is the total density of H and n(HI) is the density of atomic H. R is the H_2 formation constant (Spitzer 1978, p. 123), which is proportional to the projected area of dust grains per H nucleus, so that it must be scaled from the Galactic value of $R_{Gal} \approx 3.0 \times 10^{-17}$ cm^3 s^{-1} by the estimated dust-to-gas ratio contrast between M51 and our Galaxy (assuming similar grain properties). So equation (A2) becomes

$$R_F = R_{Gal} \frac{D_{M51}}{D_{Gal}} n_H n(\mathrm{HI}) \qquad \text{(A3)}$$

where D_{M51} and D_{Gal} are the dust-to-gas ratios in M51 and the Galaxy. By balancing molecule formations with dissociations, one can solve for the neutral fraction at any distance from the source of dissociating radiation.

The extinction in the HI and HII regions can be estimated from HKCR. From a comparison of the extinction at Hβ and the Hα-Hβ color excess with the models of Caplan and Deharveng (1986) for 11 giant HII regions, they deduce that only about 0.5 mag of the typical 1.8 mag of visual extinction could arise from within the HII regions, and that the remaining extinction occurs in foreground dust. We therefore assume that $A_V = 0.5$ mag over the $\sim$ 125 pc radius of the giant HII regions.

The dust-to-gas ratio can simply be estimated from the typical HII region visual extinction of about 1.8 mag and the mean gas surface density at 3 kpc from the nucleus of about 100 $M_\odot$ pc^{-2} (Lord and Young 1990; the surface density is calculated assuming the value of α in the text). This extinction represents the contribution from the HII region and the dust layer above it. There should therefore be an additional 1.3 mag of extinction from the dust associated with the gas layer on the opposite side of the plane, leading to a total extinction of 3.1 mag in a gas column. Assuming the gas and dust are coextensive, these numbers imply a column density of 2.1×10^{21} cm^{-2} per magnitude of visual extinction, compared to the Galactic value of 2×10^{21} cm^{-2} (Spitzer 1978, p. 156, 161). The inferred dust-to-gas ratio is thus about equal to the Galactic value. A check on this number can be obtained from Smith's (1982) estimate of the dust mass surface density in

the inner disk of M51 (Smith's "Bar" region) of 0.64 $M_\odot$ pc^{-2}. The dust-to-gas mass ratio calculated in this way is thus 0.006, again about equal to the Galactic value. We also use this result to calculate the extinction in the ISM outside of the HII region for use in equation (A1).

In contrast to our Galaxy, M51 should have a diffuse medium which is predominantly molecular as opposed to atomic (except near star-forming regions). In the interarms, the HI surface density is ~ 1 $M_\odot$ pc^{-2} (RBHAC) while the H_2 surface density inferred from the CO (2–1) map of Garcia-Burillo and Guélin (1990) is ~ 50 $M_\odot$ pc^{-2}. Hence, if the diffuse medium has any appreciable surface density at all relative to the cloudy medium, it should be largely molecular. We assume the ISM outside of the HII region consists of two components: a uniformly distributed population of homogeneous dense clouds all with properties of a canonical Galactic GMC ($M = 4 \times 10^5$ $M_\odot$, $D = 40$ pc), and a uniformly distributed diffuse molecular medium between the dense clouds. The total molecular surface density in the region where the HI emission features are found, just downstream of the peak of CO emission, is estimated from the map of Garcia-Burillo and Guélin (1990) to be about 140 $M_\odot$ pc^{-2}. The full-thickness of the gaseous layer is initially taken to be 150 pc. Finally, we assume that there is no neutral gas within the HII region.

Our method is to assume fractions of the total surface density which are in dense clouds and diffuse gas, and calculate first the neutral fraction in the diffuse gas as a function of the distance from the cluster center. We call the distance at which the neutral fraction drops to 0.5 the "radius"of the HI region. For this calculation

we need to know the volume filling factor of the dense clouds. This we calculate from the areal filling factor (equal to the assumed surface density of dense clouds divided by the observed total molecular surface density) and the assumed full-thickness of the gas layer. For any radiation field intensity of interest, the dense clouds will be completely opaque and can be treated as opaque disks in the calculation for the diffuse component. For computational purposes, we arrange the dense clouds in equally-spaced shells around the HII region, with the linear separation between clouds in each shell and the shell-to-shell separation both equal to the inverse of the linear filling factor, and the height of each shell set by the full-thickness of the gaseous layer.

Having determined the neutral fraction in the diffuse gas as a function of radius, we calculate the thickness of the dissociated envelopes of the dense clouds as a function of distance from the cluster, taking into account the attenuation in the diffuse molecular gas between the cloud and the cluster. We use a plane-parallel geometry for the cloud surfaces. The "thickness" is defined as the depth at which the neutral fraction drops to 0.5. Finally, we calculate the total HI surface density as a function of distance from the cluster, approximating that the HI surface density per dense cloud will equal the volume density times the envelope thickness.

We first show that the dominant contributor to the HI surface density in a dissociation feature is the diffuse, not the dense, component. If the gas is all in canonical dense clouds, then we calculate that a dense cloud at the edge of the HII region (125 pc from the cluster) will have a dissociated envelope with a thickness

of 0.3 pc. The corresponding surface density for the entire cloud system (for which the areal filling factor will be about 0.2) is only 1 $M_\odot$ pc^{-2}. For an alternative estimate of the envelope thickness, we use the calculations of Federman, Glassgold, and Kwan (1979). Using their equation (10) and our parameters at 125 pc from the cluster, we find an envelope thickness of 0.7 pc. Hence, the negligible contribution to the surface density is confirmed.

Figure 10 shows surface density profiles for various dense-diffuse fractions. To reproduce the observed HI region radius of 350 pc, most of the gas must be in the dense component. However, for diffuse fractions too low, the central surface density begins to drop below the observed value. The necessary fraction in the diffuse component can be doubled by assuming that the gas layer has a full-thickness of 300 pc (Figure 10).

Our results, therefore, depend on the rather uncertain gas layer thickness and dense-diffuse fraction. We can, however, approximately reproduce an observed HI region with reasonable parameters. The sizes are somewhat underestimated for some cases. However, in the text we describe other effects which may lead to the large observed sizes of the dissociation features.

Table 1. Typical Arm and Interarm Gas Surface Densities

Component	$\Sigma_{\rm arm}$ ($M_\odot$ pc^{-2})	$\Sigma_{\rm interarm}$ ($M_\odot$ pc^{-2})
Molecular Gas	180	45
Neutral Gas	10	1
Ionized Gas	2	1

Table 2. Infrared Properties of M51

		Reference
$f_\nu(12\ \mu\mathrm{m})$	11 ± 5 Jy	Rice *et al.* 1988
$f_\nu(25\ \mu\mathrm{m})$	17 ± 6 Jy	"
$f_\nu(60\ \mu\mathrm{m})$	109 ± 4 Jy	"
$f_\nu(100\ \mu\mathrm{m})$	292 ± 7 Jy	"
$f_\nu(170\ \mu\mathrm{m})$	393 Jy	Smith 1982
L_{FIR} (40 μm–120 μm)	$1.9 \times 10^{10}\ L_\odot$	Rice *et al.* 1988
L_{FIR}/L_B	0.7	"
L_{IRAS} (5 μm–1 mm)	$5.0 \times 10^{10}\ L_\odot$	"
Infrared Excess (IRE)	24	This work
T_W	209.4 K	Rice *et al.* 1988
T_C	33.4 K	Rice *et al.* 1988

Table 3. Original and Deconvolved *IRAS* Map Resolutions

Band	Original Resolution	Deconvolved Resolution
	In-Scan/Cross-Scan FWHM	In-Scan/Cross-Scan FWHM
12 μm	45"/271"	30"/78"
25 μm	43"/271"	32"/81"
60 μm	83"/278"	33"/56"
100 μm	170"/290"	59"/69"

References

Allen, R. J., Atherton, P. D., and Tilanus, R. P. J. 1986, *Nature*, **319**, 296.

Appleton, P. N., Foster, P. A., and Davies, R. D. 1986, *M. N. R. A. S.*, **221**, 393.

Beichman, C., Boulanger, F., Rice, W., and Lonsdale Persson, C. J. 1987, in *Star Formation in Galaxies*, ed. C. J. Lonsdale Persson (NASA: CP 2466), p. 297.

Bloemen, H., Deul, E. R., and Thaddeus, P. 1990, preprint.

Bothun, G. D., Lonsdale, C. J., and Rice, W. 1989, *Ap. J.*, **341**, 129.

Brinks, E. and Bajaja, E. 1986, *Astr. Ap.*, **169**, 14.

Caplan, J. and Deharveng, L. 1986, *Astr. Ap.*, **155**, 297.

Carranza, G., Crillon, R., and Monnet, G. 1969, *Astr. Ap.*, **1**, 479.

Cox, P., Krügel, E., and Mezger, P. G. 1986, *Astr. Ap.*, **155**, 380.

Cox, P. and Mezger, P. G. 1987, in *Star Formation in Galaxies*, ed. C. J. Lonsdale Persson (NASA: CP 2466), p. 23.

Dalgarno, A., and Stevens, T. L. 1970, *Ap. J. (Letters)*, **160**, L107.

de Jong, T., Dalgarno, A., and Boland, W. 1980, *Astr. Ap.*, **91**, 68.

Elmegreen, B. G., Elmegreen, D. M. and Seiden, P. E. 1989, *Ap. J.*, **343**, 602.

Federman, S. R., Glassgold, A. E., and Kwan, J. 1979, *Ap. J.*, **227**, 466.

Garcia-Burillo, S., and Guélin, M. 1990, preprint.

Habing, H. J. 1968;Bull. Astr. Inst. Netherlands;19;421

Helou, G. 1986, *Ap. J. (Letters)*, **311**, L33.

Hollenbach, D., Werner, M. W., and Salpeter, E. E. 1971, *Ap. J.*, **163**, 155.

Kennicutt, R. C. 1984, *Ap. J.*, **287**, 116.

Kennicutt, R. C., Edger, B. K., and Hodge, P. W. 1989, *Ap. J.*, **339**, 761.

Klein, U., Wielebinski, R., and Beck, R. 1984, *Astr. Ap.*, **135**, 213.

Lonsdale-Persson, C. J. and Helou, G. 1987, in *Star Formation in Galaxies*, ed. C. J. Lonsdale Persson (NASA: CP 2466), p. 23.

Lord, S. D., and Young, J. S. 1990, *Ap. J.*, **356**, 135.

Low, F. J. *et al.* 1984, *Ap. J. (Letters)*, **278**, L19.

Mezger, P. G. 1978, *Astr. Ap.*, **70**, 565.

Mezger, P. G., Smith, L. F., and Churchwell, E. 1974, *Astr. Ap.*, **32**, 269.

Myers, P. C., Dame, T. M., Thaddeus, P., Cohen, R. S., Silverberg, R. F., Dwek, E., and Hauser, M. G. 1986, *Ap. J.*, **301**, 398.

Neugebauer, G. *et al.* 1984, *Ap. J. (Letters)*, **278**, L1.

Pagel, B. E. J., and Edmunds, M. G. 1981, *Ann. Rev. Astr. Ap.*, **19**, 77.

Puget, J. L., Léger, A., and Boulanger, F. 1985, *Astr. Ap.*, **142**, L19.

Rand, R. J., and Kulkarni, S. R. 1990a, *Ap. J. (Letters)*, **349**, L43 (RK).

Rand, R. J., and Kulkarni, S. R. 1990b, in preparation.

Rand, R. J. and Tilanus, R. P. J. 1990, in *The Interstellar Medium in Galaxies*, eds. H. A. Thronson and J. M. Shull (Dordrecht:Kluwer), p. 525.

Rice, W., Boulanger, F., Viallefond, F., Soifer, B. T., and Freedman, W. L. 1990, *Ap. J.*, **358**, 418.

Rice, W., Lonsdale, C. J., Soifer, B. T., Neugebauer, G., Kopan, E. L., Lloyd, L. A., De Jong, T., and Habing, H. J. 1988, *Ap. J. Suppl.*, **68**, 91.

Rots, A. H. 1980, *Ap. J. Suppl.*, **41**, 189.

Rots, A. H., Bosma, A., van der Hulst, J. M., Athanassoula, E., and Crane, P. C. 1990, *A. J.*, **100**, 387 (RBHAC).

Sandage, A., and Tammann, G. A. 1975, *Ap. J.*, **196**, 313.

Scoville, N. Z., and Good, J. C. 1989, *Ap. J.*, **339**, 149.

Scoville, N. Z., and Sanders, D. B. 1987, in *Interstellar Processes*, ed. D. Hollenbach and A. Thronson (Dordrecht: Reidel), p. 21.

Scoville, N. Z., and Young, J. S. 1983, *Ap. J.*, **265**, 148.

Smith, J. 1982, *Ap. J.*, **261**, 463.

Spitzer, L. J. 1978, *Physical Processes in the Interstellar Medium* (New York: Wiley).

Tilanus, R. P. J., and Allen, R. J. 1989, *Ap. J. (Letters)*, **339**, L57 (TA).

Tilanus, R. P. J., Allen, R. J., van der Hulst, J. M., Crane, P. C., and Kennicutt, R. C. 1988, *Ap. J.*, **330**, 667.

Tully, R. B. 1974a, *Ap. J. Suppl.*, **27**, 437.

Tully, R. B. 1974b, *Ap. J. Suppl.*, **27**, 449.

van der Hulst, J. M., Kennicutt, R. C., Crane, P. C., and Rots, A. H. 1980, *Astr. Ap.*, **195**, 38 (HKCR).

Vogel, S. N., Kulkarni, S. R., and Scoville, N. Z. 1988, *Nature*, **334**, 402 (VKS).

Wainscoat, R. J., de Jong, T., and Wesselius, P. R. 1987, *Astr. Ap.*, **181**, 225.

Walterbos, R. A. M. and Schwering, P. B. W. 1987, *Astr. Ap.*, **180**, 27.

Figure Captions

FIG. 1. Shown in the top left panel are contours of CO emission from the OVRO mosaic overlaid on a red CCD image. The contour levels are as stated in RK. The top right panel shows CO contours overlaid on an Hα CCD image. The bottom left panel shows contours of CO overlaid on a grey-scale representation of the VLA 21-cm map. The bottom right panel shows contours of 21-cm emission on the Hα image. The contour levels are 1, 1.5, 2, and 4 times 8.4×10^{20} cm^{-2} in the bottom right panel.

FIG. 2. The radial distributions of total gas (H_2 plus HI) surface density, Hα emission, and HI surface density. The radial profiles of Lord and Young (1990, for $R < 150$") and Scoville and Young (1983, for $R > 150$") have been converted to surface density units assuming $\alpha = 3 \times 10^{20}$ mol cm^{-2} (K km s^{-1})$^{-1}$. The Hα intensities have been corrected for $A_V = 2$ mag of extinction (see van der Hulst *et al.* (1988).

FIG. 3. Cuts in surface density through typical on-arm molecular, neutral and ionized gas features along the NW arm: (*solid line*) a cut across the CO (2–1) arm of Garcia-Burillo and Guélin (1990; see text for the conversion from CO (2–1) flux to surface density), (*dashed line*) a cut through a prominent HI emission feature on the NW arm, and (*dot-dashed line*) a cut through a typical giant HII region on the same arm (see text for the conversion of Hα flux to surface density). The peak EM of the HII region roughly corresponds to $10\,(\phi/0.1)^{-1/2}$ M$_\odot$ pc^{-2}, where ϕ is the filling factor of the ionized gas.

FIG. 4. A close-up of a spiral arm segment south of the nucleus showing the small scale relationship between HI, Hα and CO emission. The solid contours are HI emission. The levels are 1, 2, 3, 4, and 5 times 8.4×10^{20} cm^{-2}. The dashed contours are CO emission from the OVRO mosaic. The grey-scale represents Hα emission. The flow direction is indicated. The area labelled "A" is an example of a region where an HI peak coincides with an HII region. The areas labelled "B" are examples of HI peaks *between* HII regions.

FIG. 5. The original maps of *IRAS* emission in M51: *a)* 12μm, *b)* 25μm, *c)* 60μm, and *d)* 100μm. The unit contour interval is the estimated noise in the map.

FIG. 6. Cuts through the original *IRAS* maps and Hα and *B*-band CCD images along the *IRAS* in-scan direction from NE to SW.

FIG. 7. The deconvolved maps of *IRAS* emission in M51: *a)* 12μm, *b)* 25μm, *c)* 60μm, and *d)* 100μm. The unit contour interval is the estimated noise in the map.

FIG. 8. Cuts through the deconvolved *IRAS* maps and Hα and *B*-band CCD images along the *IRAS* in-scan direction from NE to SW.

FIG 9. Deconvolution of the *IRAS* 60μm survey data on M51 by W. N. Weir using the MEMSYS package. The contour levels are 5, 10, 15, 20, 25, 30, 35, 40, 50, 60, 70, 80, and 90 percent of the peak.

FIG 10. Profiles of HI surface density for five model dissociation regions with varying dense cloud-diffuse gas fractions and gas disk full-thicknesses: *(solid line)* all diffuse

gas, full-thickness 150 pc, *(dotted line)* 50% diffuse gas, full-thickness 150 pc, *(short-dashed) line* 25% diffuse gas, full-thickness 150 pc, *(long-dashed line)*, 13% diffuse gas, full-thickness 150 pc, and *(dot-dashed line)* 25% diffuse gas, full-thickness 300 pc.

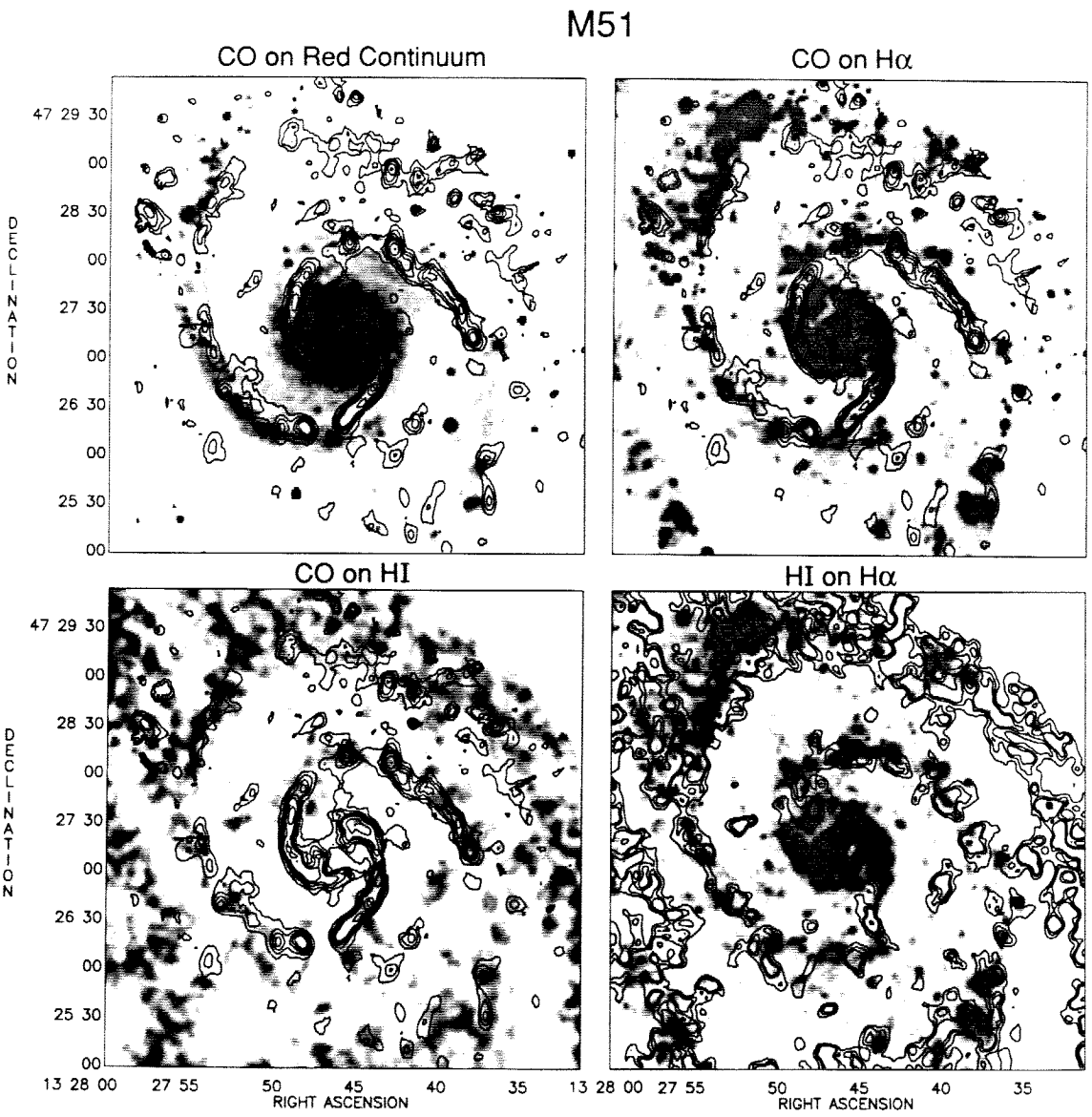
M51
CO on Red Continuum
CO on Hα
CO on HI
HI on Hα
DECLINATION
47 29 30
00
28 30
00
27 30
00
26 30
00
25 30
00
13 28 00
27 55
50
45
40
35
RIGHT ASCENSION

Figure 1

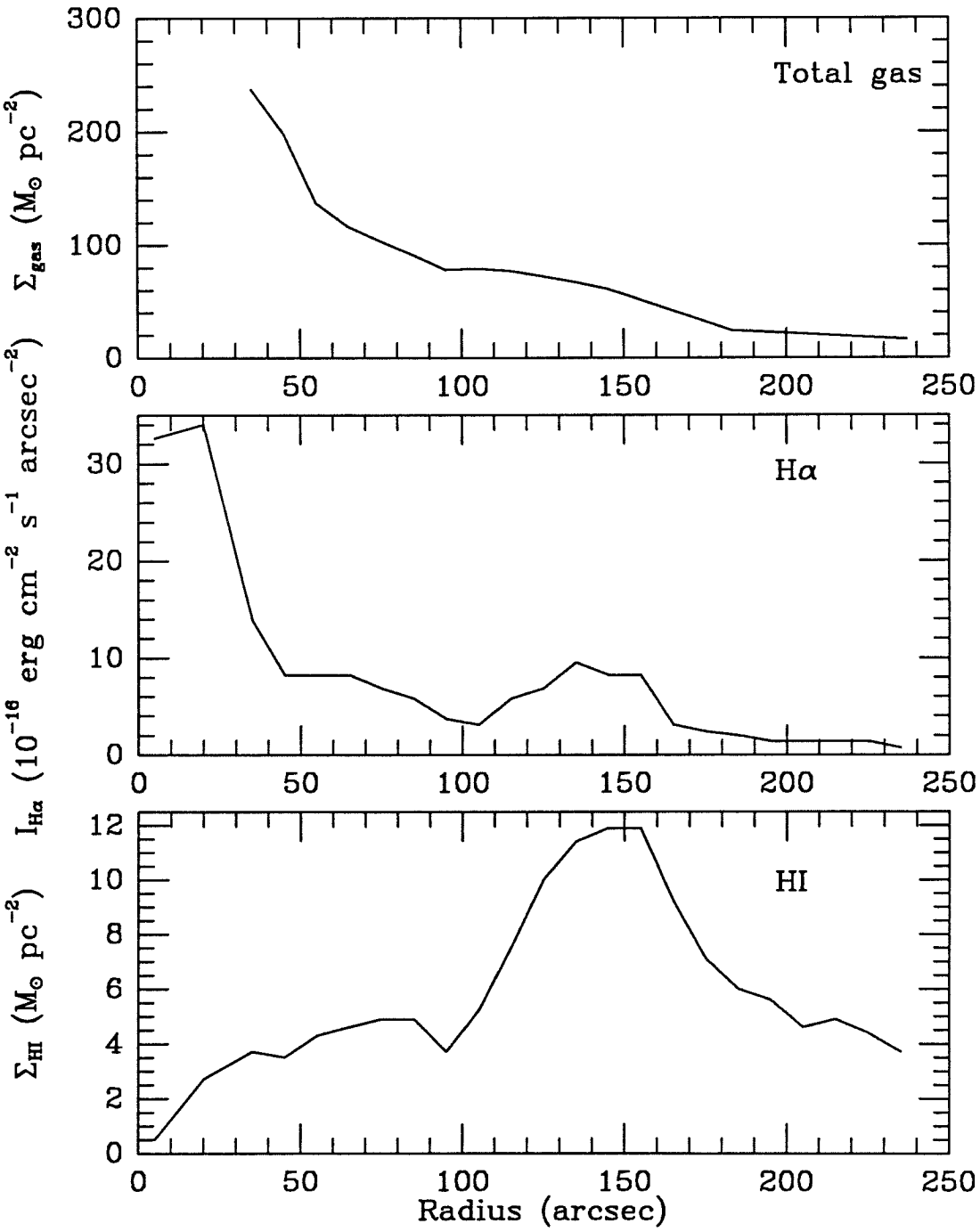
Total gas
Hα
HI
Σ_{gas} ($M_\odot$ pc^{-2})
$I_{H\alpha}$ (10^{-16} erg cm^{-2} s^{-1} arcsec^{-2})
Σ_{HI} ($M_\odot$ pc^{-2})
Radius (arcsec)

Figure 2

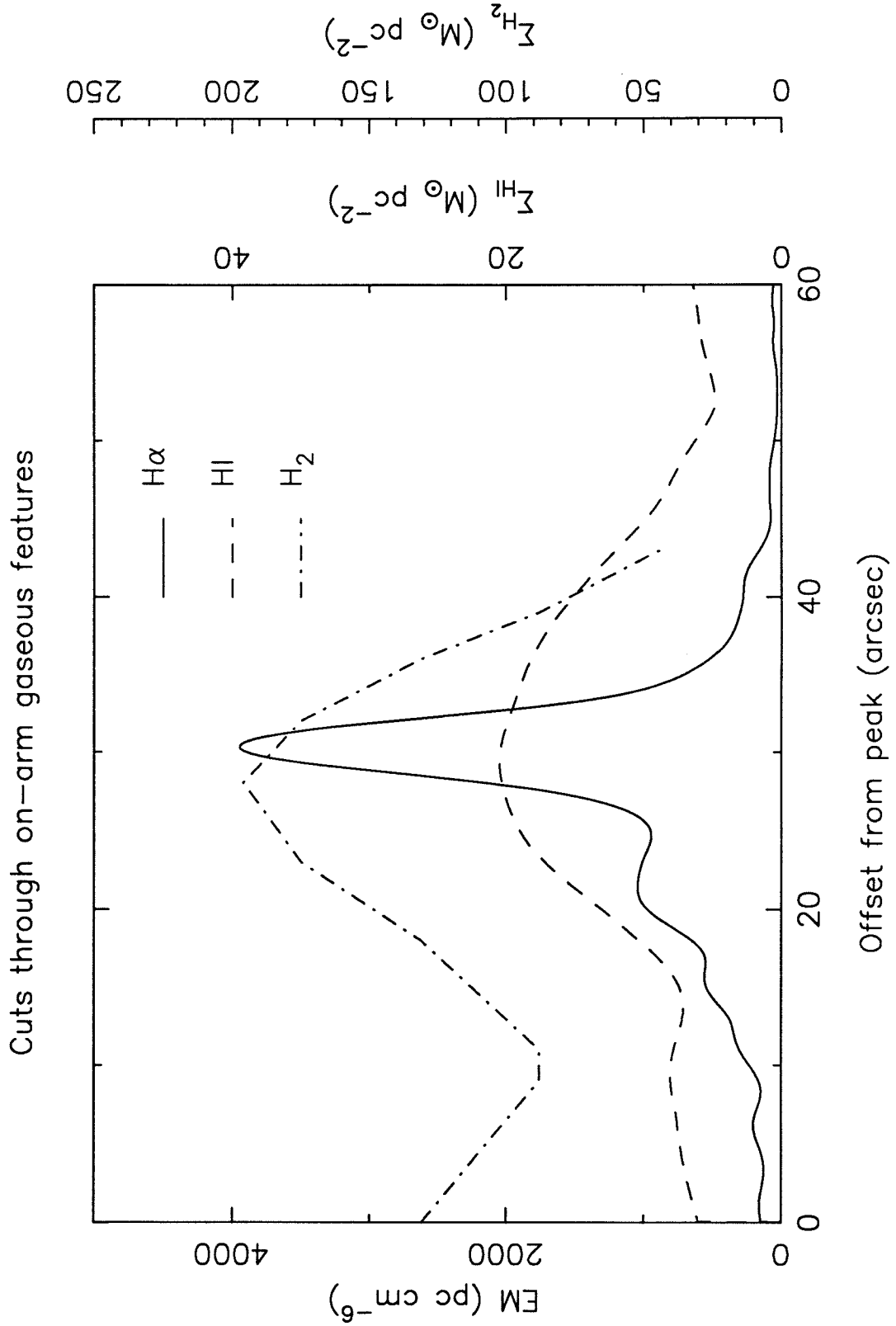
Cuts through on−arm gaseous features
Hα
HI
H2
EM (pc cm−6)
0
2000
4000
ΣHI (M⊙ pc−2)
0
20
40
ΣH2 (M⊙ pc−2)
0
50
100
150
200
250
Offset from peak (arcsec)
0
20
40
60

Figure 3

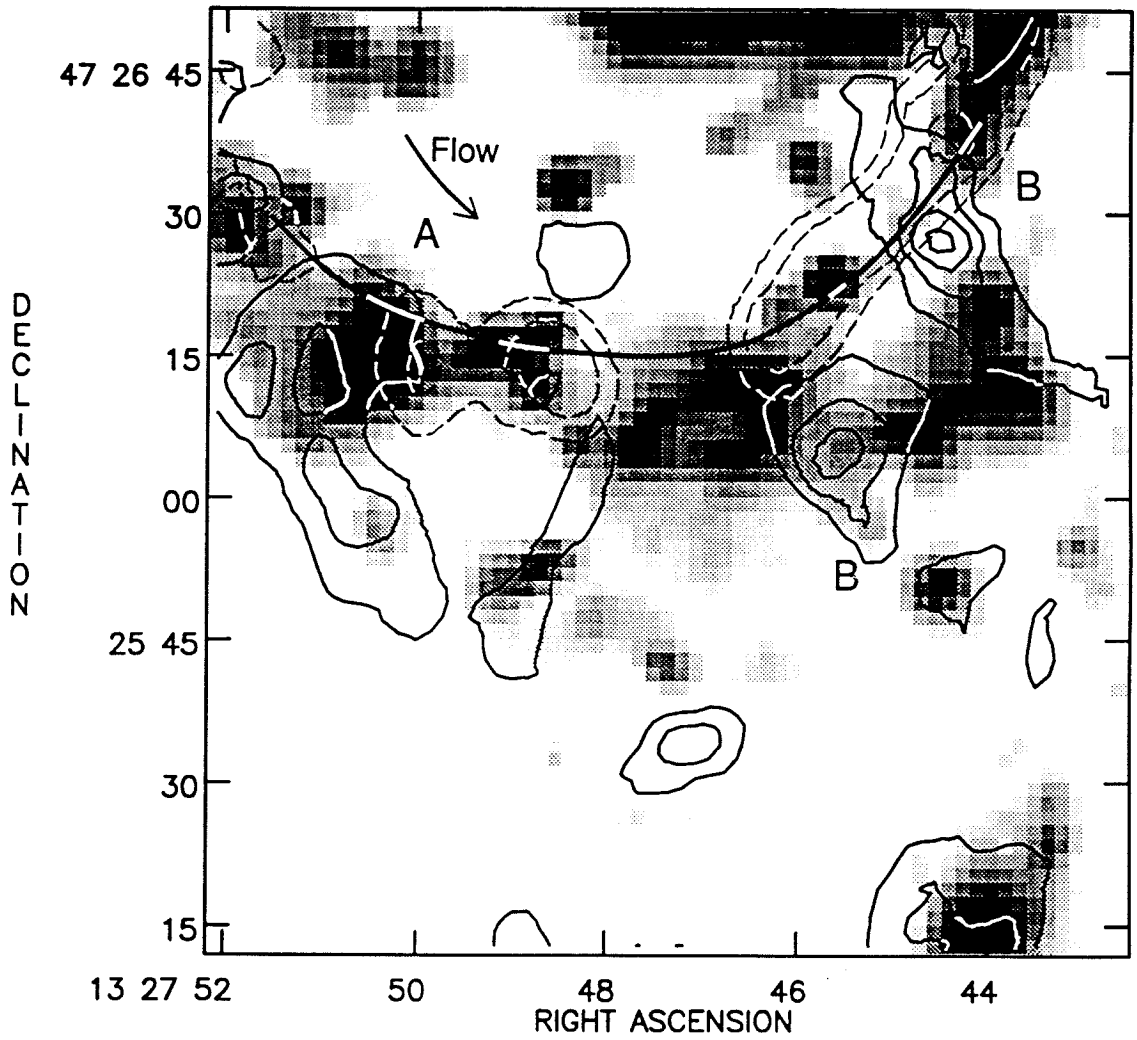
47 26 45
30
15
00
25 45
30
15
DECLINATION
Flow
A
B
B
13 27 52
50
48
46
44
RIGHT ASCENSION

Figure 4

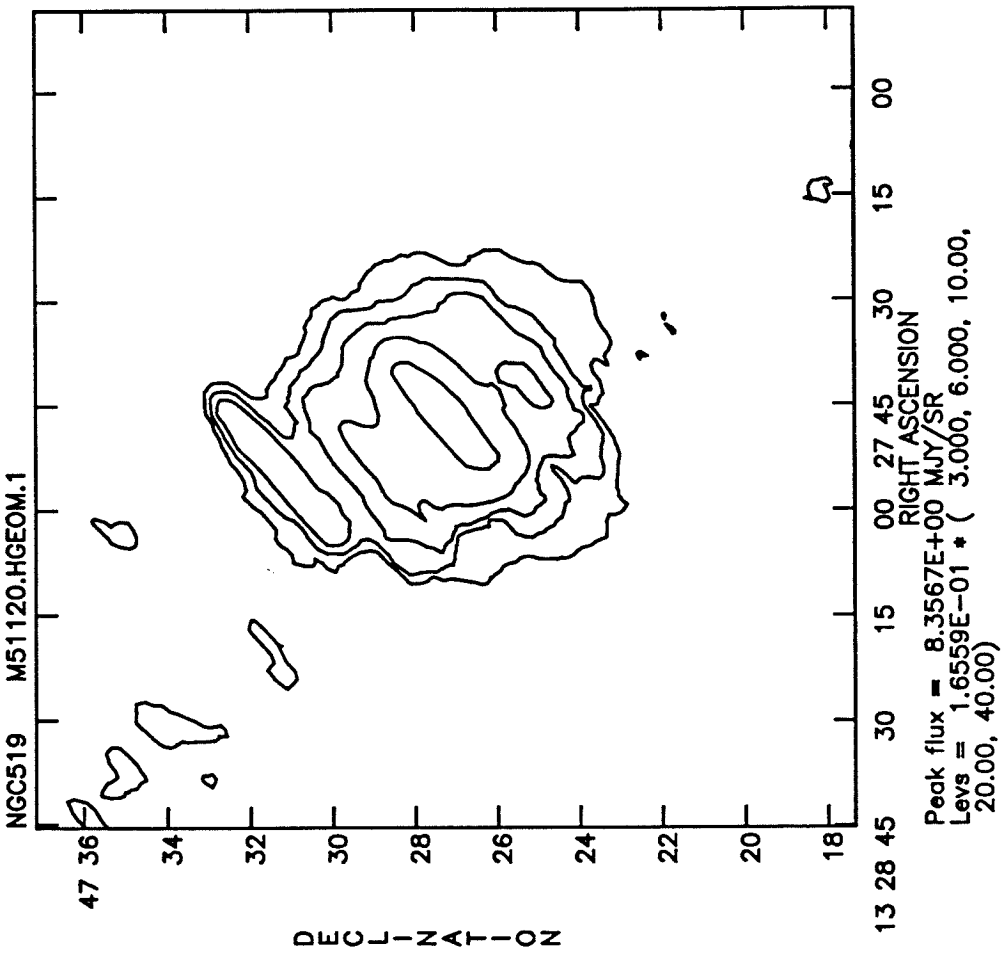
NGC519 M51120.HGEOM.1
DECLINATION
47 36
34
32
30
28
26
24
22
20
18
13 28 45
30
15
00
27 45
30
15
00
RIGHT ASCENSION
Peak flux = 8.3567E+00 MJY/SR
Levs = 1.6559E-01 * (3.000, 6.000, 10.00, 20.00, 40.00)

Figure 5*a*

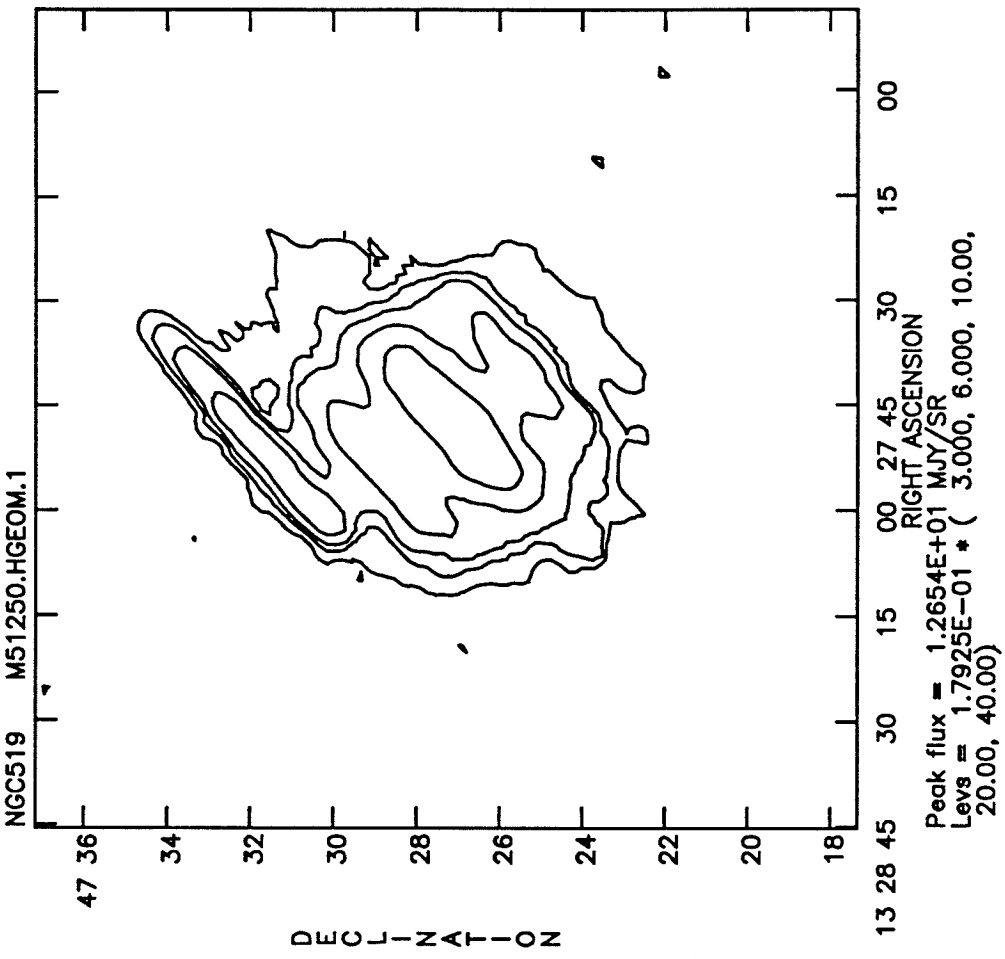
NGC519 M51250.HGEOM.1
DECLINATION
47 36
34
32
30
28
26
24
22
20
18
13 28 45
30
15
00
27 45
30
15
00
RIGHT ASCENSION
Peak flux = 1.2654E+01 MJY/SR
Levs = 1.7925E-01 * (3.000, 6.000, 10.00, 20.00, 40.00)

Figure 5*b*

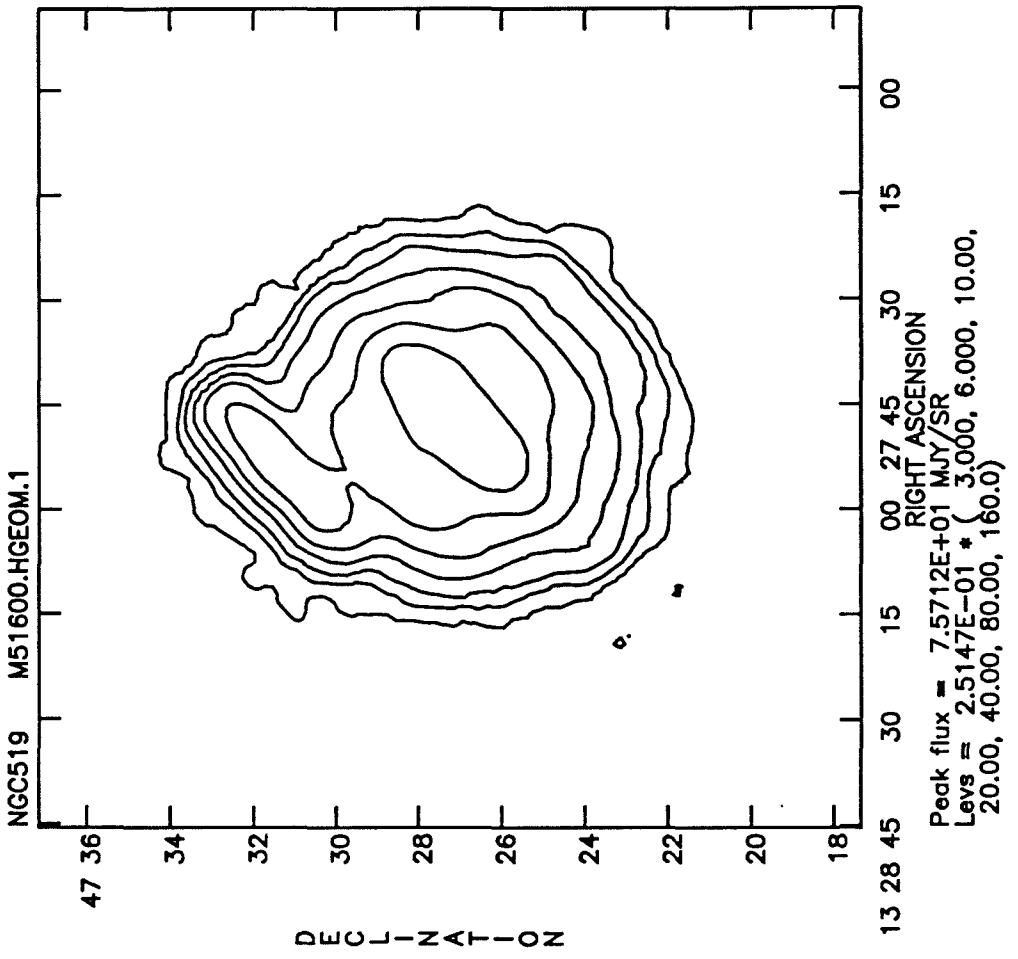
NGC519 M51600.HGEOM.1
DECL-NAT-ON
47 36
34
32
30
28
26
24
22
20
18
13 28 45
30
15
00 27 45
30
15
00
RIGHT ASCENSION
Peak flux = 7.5712E+01 MJY/SR
Levs = 2.5147E-01 * (3.000, 6.000, 10.00,
20.00, 40.00, 80.00, 160.0)

Figure 5*c*

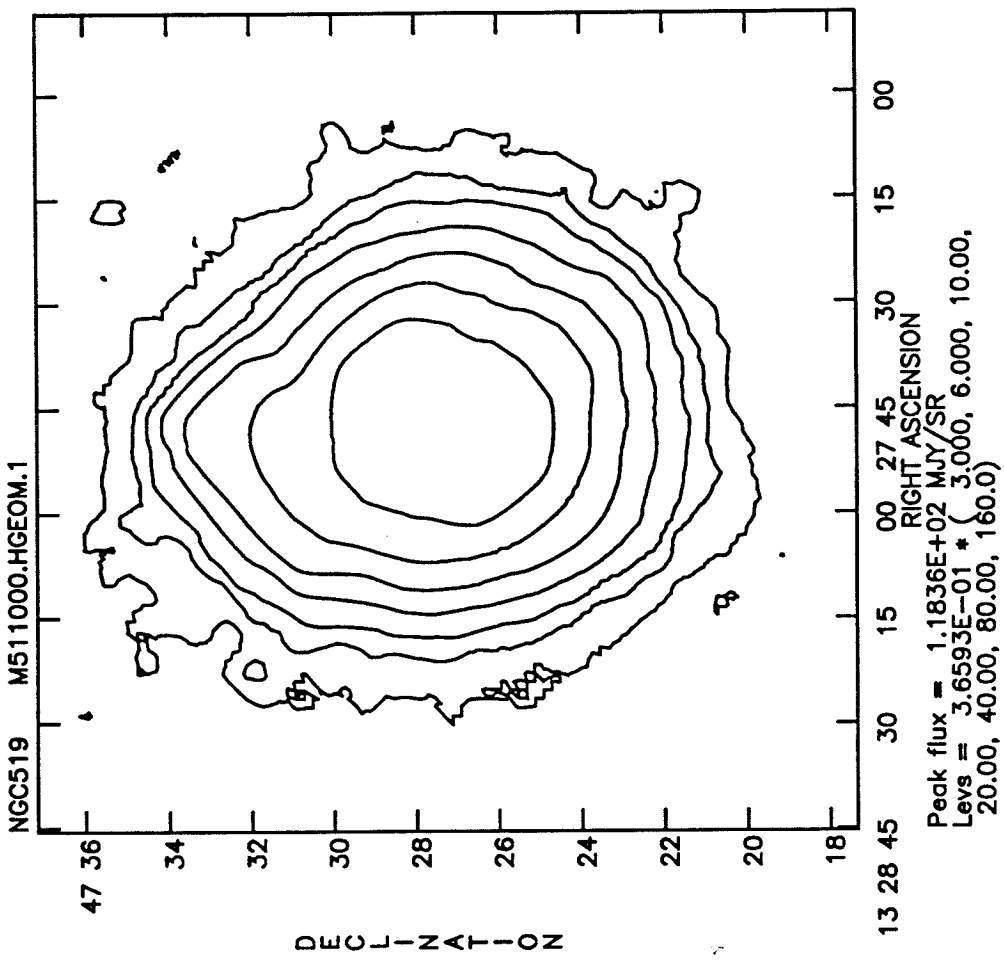
NGC519 M511000.HGEOM.1
DECLINATION
47 36
34
32
30
28
26
24
22
20
18
13 28 45
30
15
00 27 45
30
15
00
RIGHT ASCENSION
Peak flux = 1.1836E+02 MJY/SR
Levs = 3.6593E-01 * (3.000, 6.000, 10.00,
20.00, 40.00, 80.00, 160.0)

Figure 5*d*

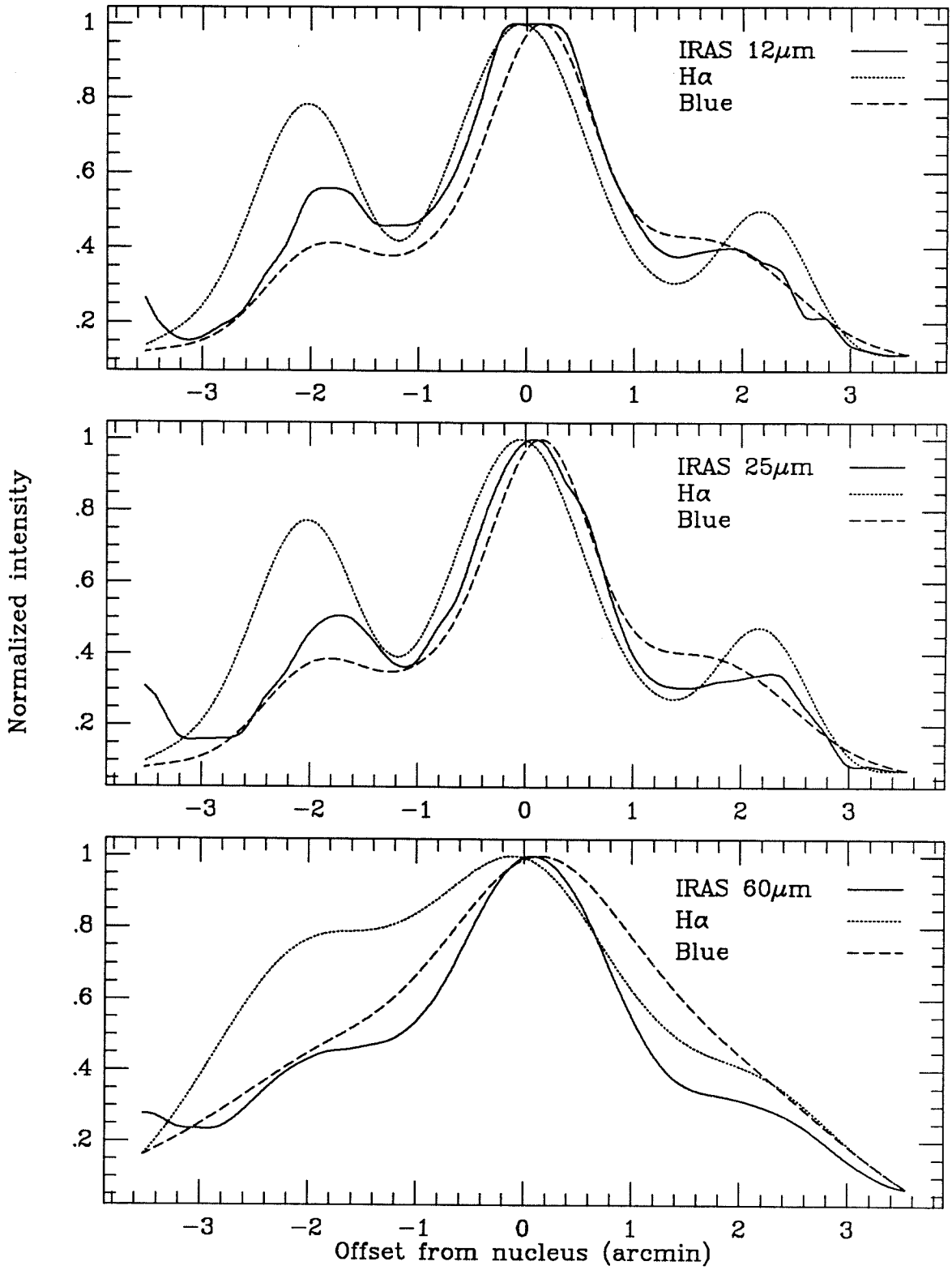
IRAS 12μm
Hα
Blue
IRAS 25μm
Hα
Blue
IRAS 60μm
Hα
Blue
Normalized intensity
Offset from nucleus (arcmin)

Figure 6

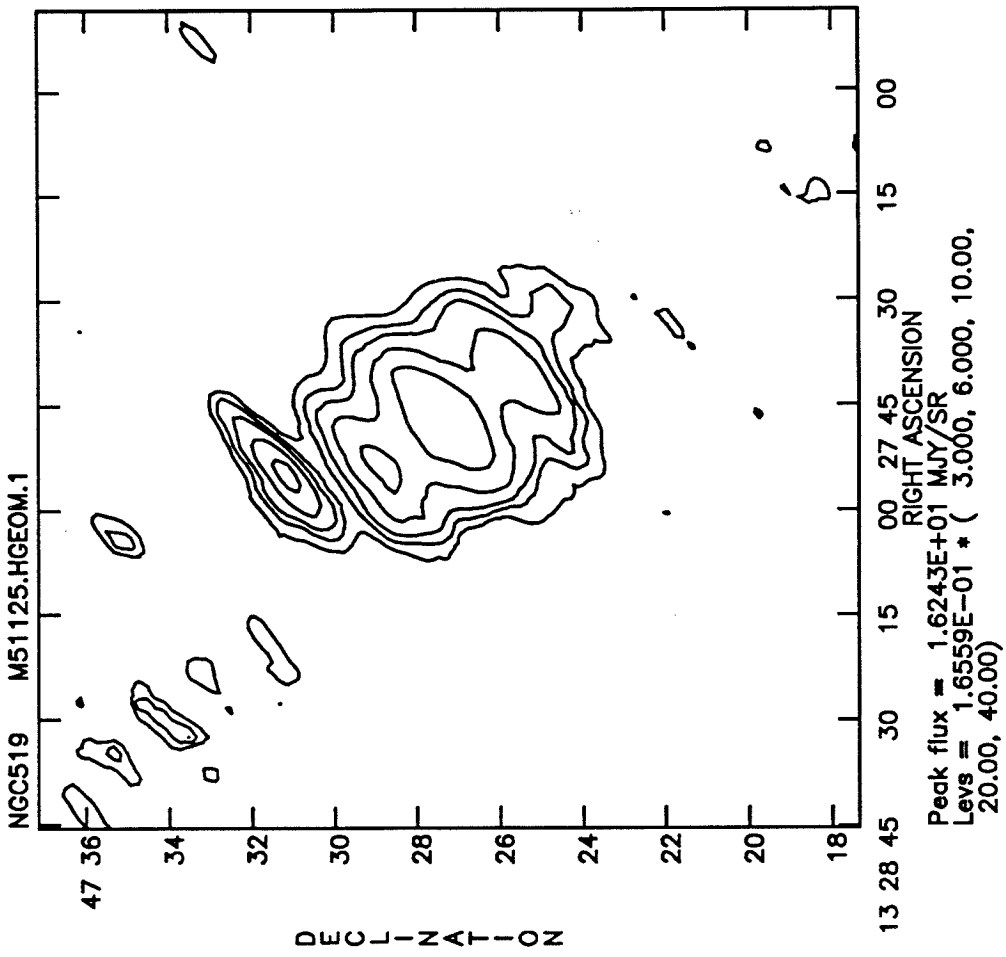
NGC519 M51125.HGEOM.1
DECL-NAT-ON
47 36
34
32
30
28
26
24
22
20
18
13 28 45
15
30
00
27 45
30
15
00
RIGHT ASCENSION
Peak flux = 1.6243E+01 MJY/SR
Levs = 1.6559E-01 * (3.000, 6.000, 10.00, 20.00, 40.00)

Figure 7*a*

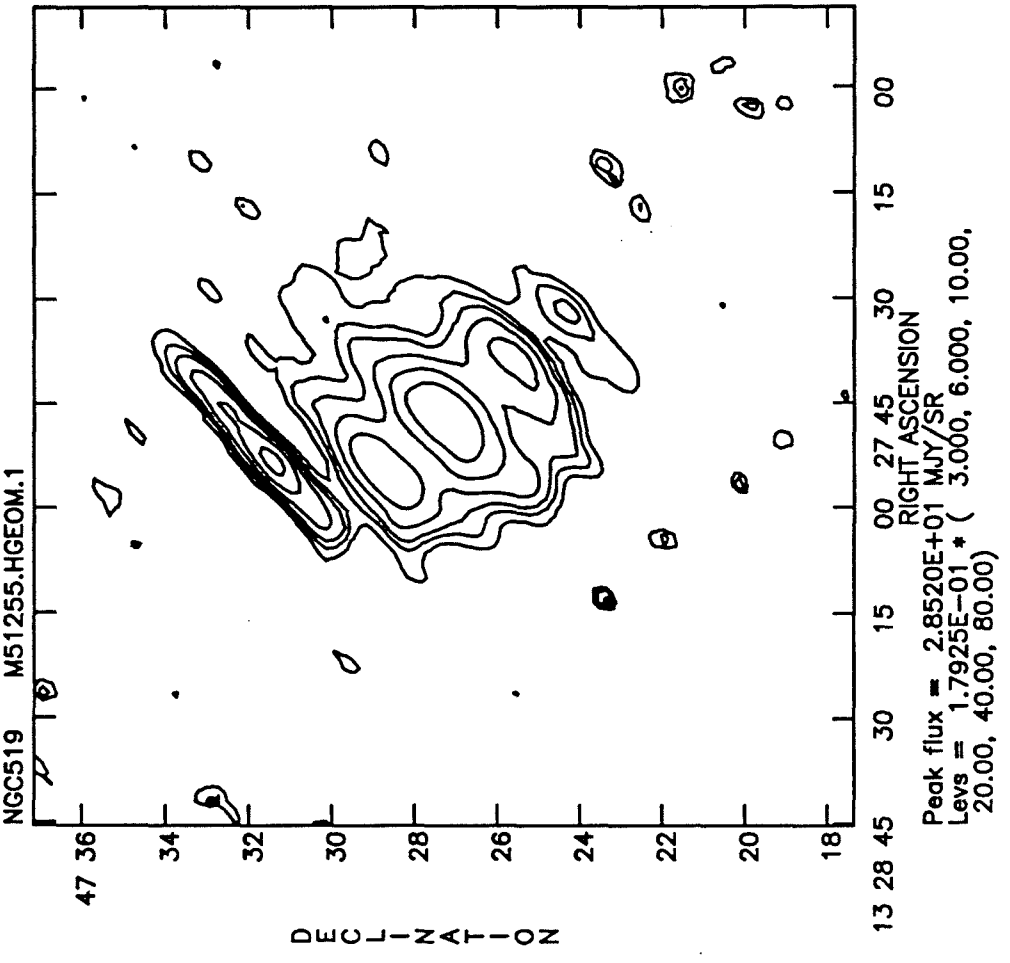
NGC519 M51255.HGEOM.1
47 36
34
32
30
28
26
24
22
20
18
DECLINATION
13 28 45
30
15
00 27 45
30
15
00
RIGHT ASCENSION
Peak flux = 2.8520E+01 MJY/SR
Levs = 1.7925E-01 * (3.000, 6.000, 10.00,
20.00, 40.00, 80.00)

Figure 7*b*

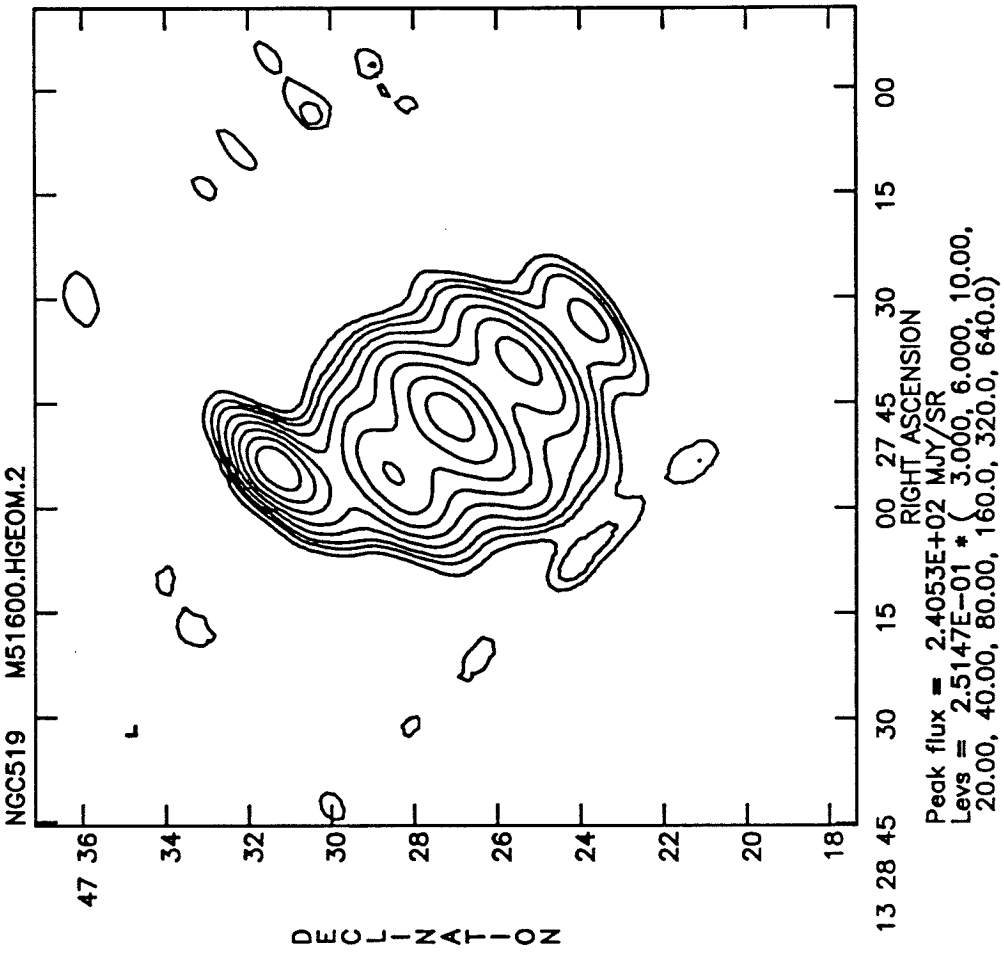
NGC519 M51600.HGEOM.2
DECLINATION
47 36
34
32
30
28
26
24
22
20
18
13 28 45
30
15
00 27 45
30
15
00
RIGHT ASCENSION
Peak flux = 2.4053E+02 MJY/SR
Levs = 2.5147E-01 * (3.000, 6.000, 10.00,
20.00, 40.00, 80.00, 160.0, 320.0, 640.0)

Figure 7*c*

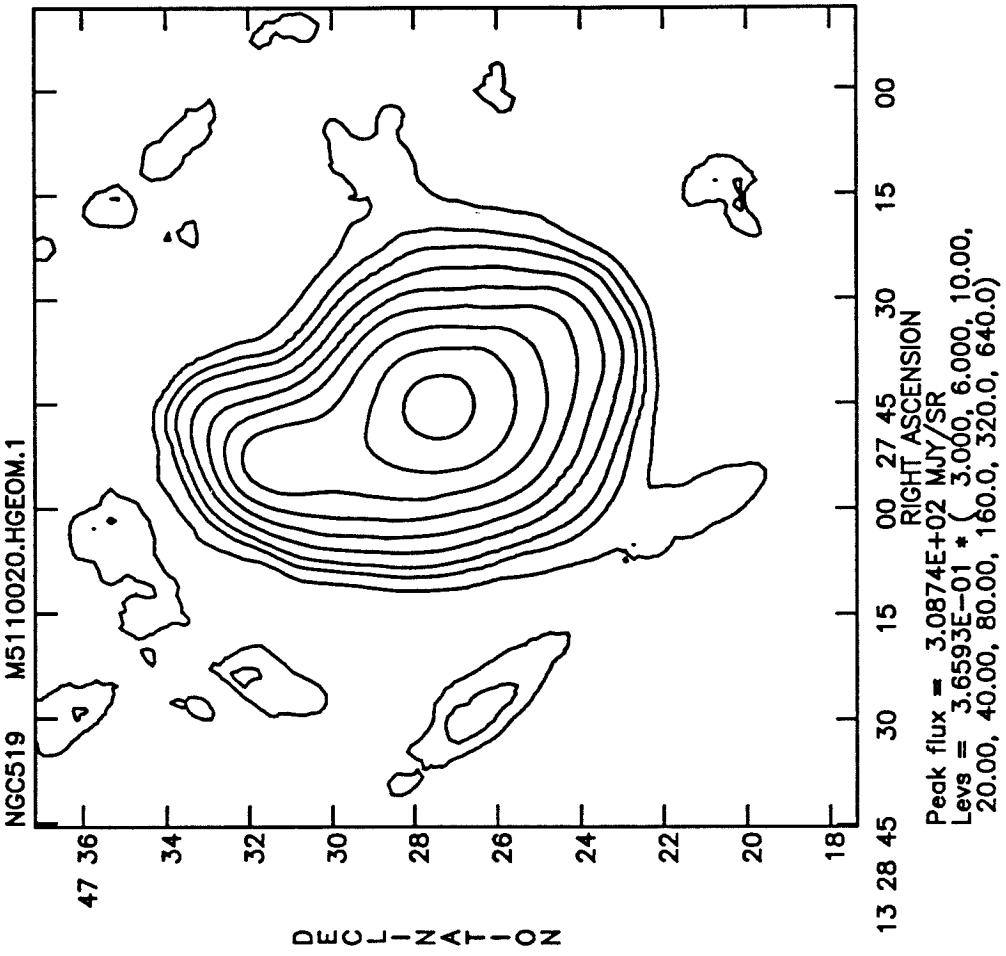
NGC519 M5110020.HGEOM.1
47 36
34
32
30
28
26
24
22
20
18
DECLINATION
13 28 45
30
15
00
27 45
30
15
00
RIGHT ASCENSION
Peak flux = 3.0874E+02 MJY/SR
Levs = 3.6593E-01 * (3.000, 6.000, 10.00,
20.00, 40.00, 80.00, 160.0, 320.0, 640.0)

Figure 7*d*

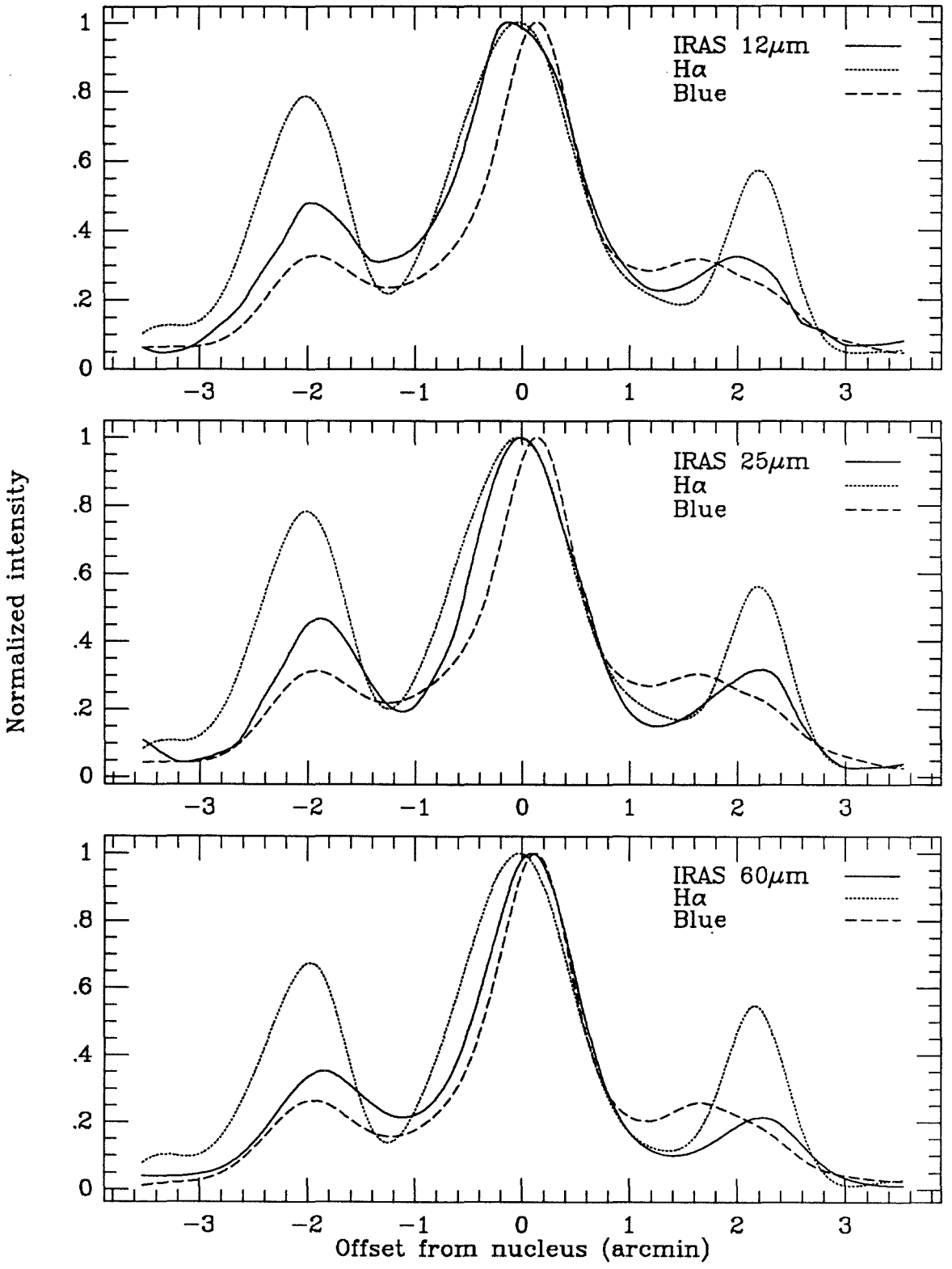
IRAS 12μm
Hα
Blue
IRAS 25μm
Hα
Blue
IRAS 60μm
Hα
Blue
Normalized intensity
Offset from nucleus (arcmin)
0
.2
.4
.6
.8
1
−3
−2
−1
0
1
2
3

Figure 8

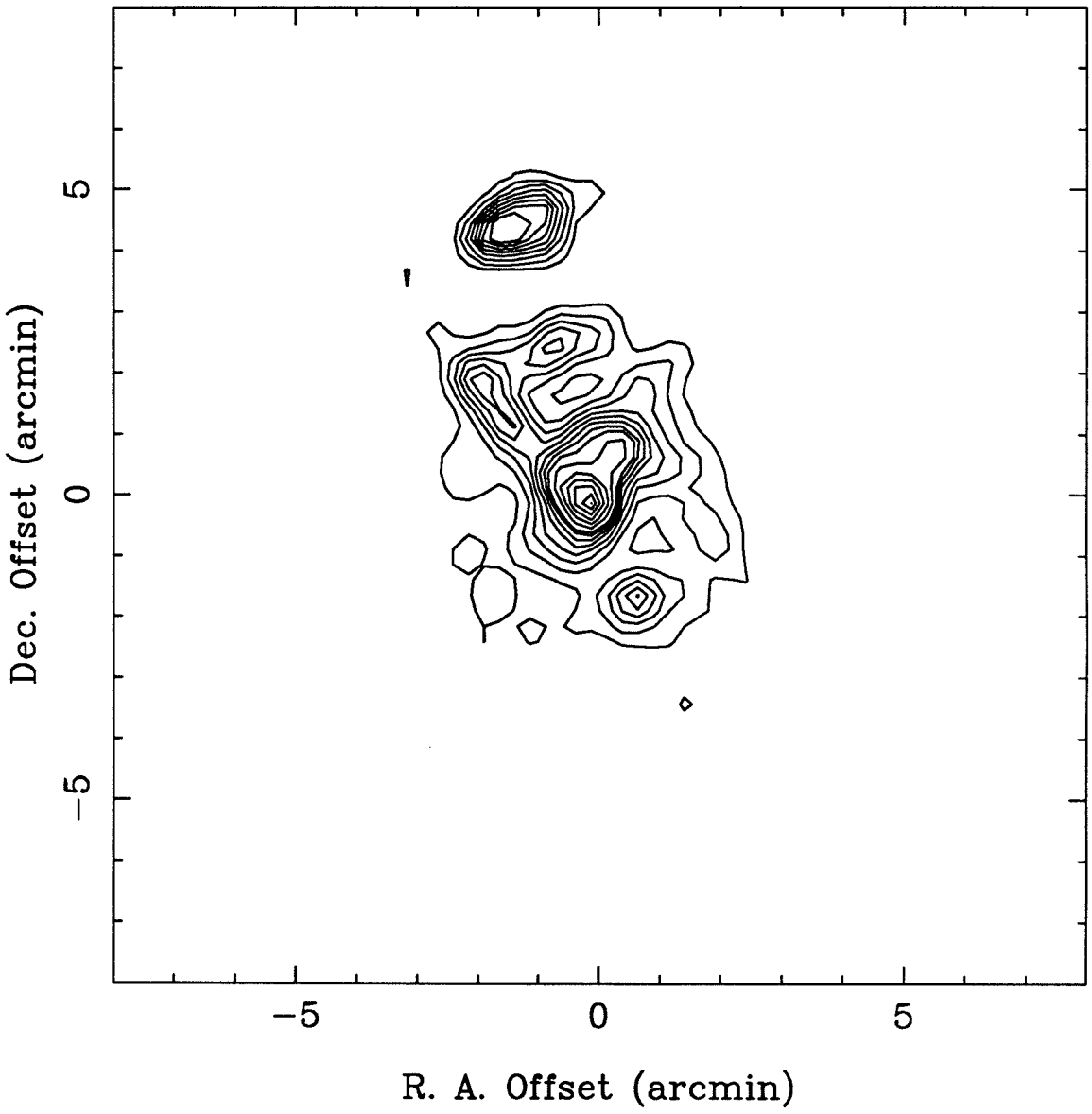

Figure 9

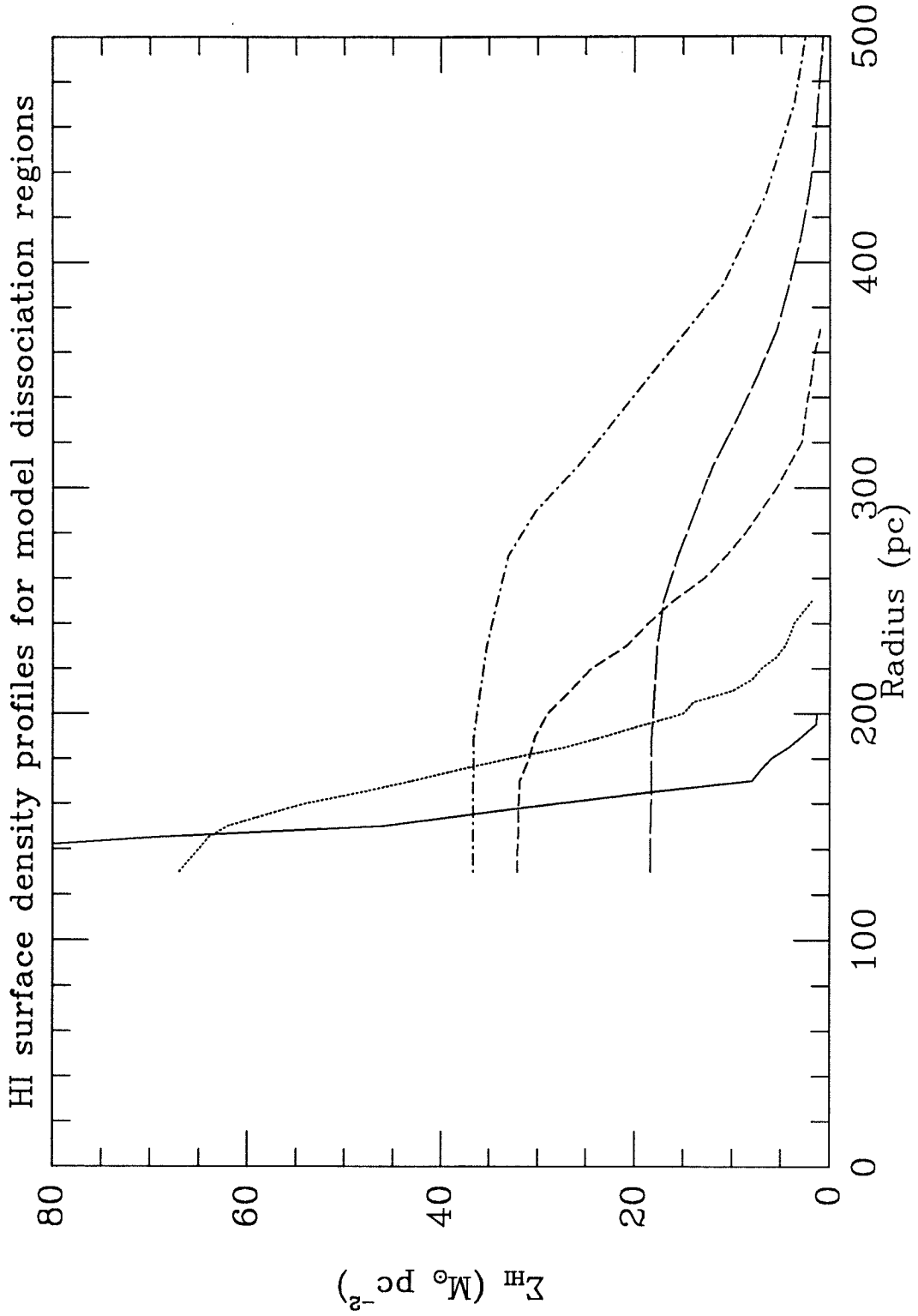
HI surface density profiles for model dissociation regions
Σ_{HI} ($M_\odot$ pc^{-2})
Radius (pc)
0
20
40
60
80
0
100
200
300
400
500

Figure 10

CHAPTER 5

Kinematics, Density Waves, and GMA Formation in M51

Abstract

New spectroscopic observations of the ionized gas (Hα and [NII] lines) and old-disk stars (Mg B band) are combined with published CO, HI and Hα data to study the kinematic response of these components to the spiral density wave. Evidence for radial streaming motions in the old-disk stars is presented. By using information from the K-band image of Wright *et al.* to trace the underlying mass distribution, we find that the amplitude of the radial motions for the minor-axis crossing of the arm at 85" from the nucleus is larger than predicted by linear density wave theory. The 4:1 resonance, which is at about this radius, may account for this large amplitude.

We present CO and HI rotation curves from the OVRO and VLA maps of M51 at 8" resolution. By comparing the CO rotation curve with an Hα rotation curve calculated from the new 8"-resolution Fabry-Perot data of Tilanus and Allen, we find that the ionized gas appears to be rotating faster than the molecular gas. We show that this effect is due to a conspiracy of beam-smoothing, tangential streaming motions, and the CO-Hα spatial offset. The molecular, neutral, and ionized gas components all show the tangential and radial streaming motions along the major and minor axis at the arm crossings as predicted by nonlinear density

wave models. However, the amplitude of the radial velocity shift for the arm at 85" from the nucleus, in analogy to the old-disk stars, is much greater than even nonlinear models predict. Interarm streaming is also clearly detected in the ionized gas, and in places in the molecular gas. Along the major axis, velocities from our spectra show small-scale differences from the predictions of the Hα rotation curve. Motions of the ionized gas out of the plane of the galaxy and random motions of the HII regions are the probable causes of the discrepancies.

Using kinematic and morphological information, we carry out an analysis of the stability of the gas on and off the arms. We first use the observed streaming motions to calculate an arm-interarm contrast of 3–5 for the molecular gas. We find that the surface density of the on-arm gas is somewhat above the critical value for instability based on the Toomre criterion, while the interarm gas is close to the point of instability. The characteristic mass associated with the instability on the arms is close to the typical Giant Molecular Association (GMA) mass of 3×10^7 $M_\odot$. There is sufficient time available while the gas is on the arms to form bound GMAs by gravitational instability or by collisional agglomeration of smaller clouds. Between the arms, there is probably insufficient time to build a GMA through either process. The minor, secondary density wave compression between the arms suggested by us in an earlier paper may be sufficient to cause mild short-lived instabilities in the gas or sufficient orbit crowding to explain the existence of the unbound interarm GMAs. Finally, we discuss problems with the conclusion that the on-arm GMAs are bound, virialized entities – in particular, the observed shear across them and

the requirement that they be destroyed rapidly (probably by star formation) – and discuss the case for their being unbound.

Subject headings: galaxies: interstellar matter – galaxies: internal motions – galaxies indiv: (M51), – stars: formation

I. Introduction

While many favor self-sustaining spiral density waves as the origin of spiral structure in galaxies, detailed comparisons of the kinematic response of galaxy components to density waves have been scarce. Observationally, still less is understood about how density waves organize the star-forming gas in galaxies and the consequences for star formation. Searches for the kinematic indications of density waves have focussed on gaseous components in galaxies with pronounced spiral structure (*e.g.*, M51, M81) because it is reasonable to expect that the peculiar kinematics predicted by density wave theory should be most obvious in the dissipative components of galaxies with strong density waves. Tully's (1974b) important Fabry-Perot study of M51 revealed on-arm tangential streaming and interarm radial streaming in the ionized gas as predicted by the theory. Visser's (1980) study of the kinematics of the neutral gas in M81 provided much support for non-linear density wave calculations (Shu, Milione, and Roberts 1973). More recently, Rydbeck, Hjalmarson, and Rydbeck (1985), Vogel, Kulkarni, and Scoville (1988, hereafter VKS) and Rand and Kulkarni (1990a, hereafter RK) demonstrated the existence of large velocity shifts in the star-forming molecular spiral arms of M51. These shifts (60-100 km s^{-1} in the plane of the galaxy) are much larger than predicted by even the nonlinear density wave studies ((Shu, Milione, and Roberts 1973; Roberts and Stewart 1987) and presumably indicate that the strength of the density wave in M51 is unusually large. Rydbeck, Hjalmarson, and Rydbeck (1985) and RK have also presented some kinematic and morphological evidence for minor density wave compressions in M51

between the main arms – a possibility first suggested by Shu, Milione, and Roberts (1973).

In studying the gaseous response to a density wave, a large uncertainty is the actual strength of the spiral gravitational perturbation in the massive old disk. A much less pronounced spiral pattern and much lower amplitude streaming motions are expected for the old-disk stars because of the relatively large velocity dispersion and the non-dissipative nature of stellar systems.

In this paper, we use information from the new K-band image of M51 by Wright *et al.* (1990) to trace the old disk light. This image shows a very smooth, low-level spiral pattern. Wright et al. state that the arm-interarm contrast in their image over the radii 70" $< R <$ 180" ranges from 1.2 to 2.1 in linear units, whereas the contrast found in an I-band image by Elmegreen, Elmegreen, and Seiden (1989) showed a range of 2.5 to 13 over the same range of radii, or typically a few times higher than at K. However, in the region of the galaxy of interest for this paper (near the western half of the minor axis), our own I-band image (obtained with the "Wide Field PFUEI" camera on the 1.5 m telescope of the Palomar Observatory) shows an arm-interarm contrast very similar to that at K, and agrees well with that measured by Elmegreen, Elmegreen, and Seiden. Hence, in the inner disk at least, it is not clear if the contrast at K is significantly reduced from that at I. Regardless of the issue of the I-band contrast, a further advantage of K-band is that the dust lanes, which are still visible at I, are not seen at K. Hence the extinction problem is much reduced.

The peculiar motions corresponding to this low-level spiral perturbation in the old disk should be much smaller than those of the gas and show a much smoother spatial variation. However, as far as these authors know, the existence of streaming motions in the old disk stars of M51 has not been demonstrated. This is understandable since the absorption lines from the old stars are much weaker than the gaseous emission lines, and the amplitude of the stellar streaming motions should be much lower than that of the gas streaming motions. If the parameters of the underlying gravitational perturbation can be directly measured, however, then they can be used to check for self-consistency between the density contrast and the stellar streaming motions. Linear density wave theory should be sufficient since the spiral pattern is smooth and of low amplitude.

A more recent focus of observational and theoretical work has been the effects of density waves on the distribution and state of the interstellar gas, and how such effects might be related to star formation. HI "superclouds" of mass $\sim 10^7$ $M_\odot$ have been observed along the arms of many nearby spirals (summarized in Elmegreen 1987a). These HI superclouds may form in a density wave compression by gravitational instabilities (Jog and Solomon 1984; Balbus and Cowie 1985; Elmegreen 1987b; Tomisaka 1987; Balbus 1990), or by agglomeration of smaller, self-gravitating clouds (Kwan and Valdes 1983, 1987; Roberts and Stewart 1987; Roberts, Adler, and Stewart 1988).

The existence of massive ($\sim 3 \times 10^7$ $M_\odot$) concentrations of *molecular* gas in the arms of M51 has been recently reported by VKS. These concentrations were

termed Giant Molecular Associations (GMAs). RK found more GMAs in the arms of M51 and also a few between the arms, and demonstrated from the 8"-resolution mosaic map that the on-arm GMAs have virial masses roughly equal to their masses based on their CO fluxes, while the interarm GMAs have virial masses several times their CO-flux-based masses. In RK, we assumed that the line widths used to calculate the virial masses were entirely due to random cloud motions within the beam. However, a fraction of the line width is due to the velocity gradient (streaming) across the GMA. This is not an issue for the interarm GMAs, most of which were resolved with little detectable streaming. A more careful virial analysis was carried out by Rand and Kulkarni (1990b). Observations at 2.5" resolution allowed two on-arm GMAs near the major axis to be resolved, and an accurate value for the tangential streaming velocity gradient to be measured. The observed gradient across a resolution element ($\sim$ 5 km s^{-1}) was found to be generally substantially less than the observed line width ($\sim$ 10 km s^{-1}), hence it was concluded that the line width is predominantly due to random motions. This allowed virial masses including contributions from both the random motions and the systematic streaming across the GMAs to be calculated. The result was still rough equality between the virial and CO-flux-based masses. The suggested formation mechanisms for the HI superclouds are also possible GMA formation mechanisms. A purpose of this paper is to address the question of whether or not the GMAs are truly bound, virialized objects.

Is the formation of these massive structures directly related to star formation? Kennicutt (1989, hereafter K89) recently used global data on the molecular, neutral and ionized gas in spirals in an attempt to connect star formation activity to the state of the gas. In particular, he has found evidence that significant star formation in galaxies only occurs above a certain gas surface density threshold which is apparently related to gravitational instabilities in the gas (essentially the Toomre criterion; see also Quirk 1972). Below this threshold, there is very little massive star formation, while above it, the star formation rate goes as a power of the surface density (a Schmidt law) with an exponent between 1 and 2. K89's analysis suggests that the star formation threshold depends on gravitational instabilities in the gas and is therefore really a massive cloud formation threshold. Hence, the fundamental physical process underlying his results may be the formation of massive clouds, which then leads to the nonlinear Schmidt law because the gas surface density is above the threshold. A simple explanation for density wave triggering in M51 would therefore be that the on-arm gas is unstable by this criterion while the interarm gas is stable. However, observational information on how density waves affect the stability of the gaseous component is lacking. Such information could allow an assessment of whether star formation could be triggered by density waves in this way. Alternatively, if massive star formation occurs at the interface of colliding clouds, then to first order the star formation rate should depend on the square of the cloud number density (Scoville, Sanders, and Clemens 1986). Hence, the density wave increases the star formation efficiency by increasing the cloud collision rate.

The first goal of this paper is to present as complete an observational analysis as is currently possible of the density wave in M51, and the response of the various components. From absorption-line spectroscopy, we search for streaming motions in the old-disk stars along the minor axis, and compare with the predictions of linear density wave theory, using the K-band image of Wright *et al.* (1990) to infer the mass distribution (§III). In §IV, from optical emission-line spectroscopy and CO and HI interferometric observations, we compare the kinematics of the molecular, neutral and ionized gas components along the major and minor axes with the predictions of current density wave models.

In §V, we use observations of the gas surface density and kinematics to test the two suggested mechanisms of arm and interarm GMA formation. In particular, we compute the instability criterion discussed in K89 for both the arm and interarm regions to find out whether the gas should be gravitationally unstable to collapse, and then calculate whether there is sufficient time for the GMAs to form by such instabilities while the gas is in the arms. We also estimate the time required to build GMAs by collisional agglomeration of smaller clouds. The possible connection between GMA formation and the triggering of star formation is briefly discussed. Finally, we address the issue of the boundedness of the on-arm GMAs and the problem of rapidly disrupting bound GMAs to explain their confinement to narrow spiral arms.

Throughout this paper, we assume Tully's (1974a) value of the inclination (20°) of M51, the position angle of the major axis (170°), and the systemic velocity

(V_{lsr} = 472 km s^{-1}). The distance to M51 is taken to be 9.6 Mpc (Sandage and Tammann 1975), so that 1" = 46.5 pc.

II. Observations

a) Optical Spectroscopy

The spectroscopic observations were carried out using the Double Spectrograph on the Hale 5-m telescope at the Palomar Observatory on the nights of May 23–25, 1989. All three nights were photometric, and seeing ranged from 1" to 2". Both sides of the spectrograph were equipped with Texas Instruments 800 × 800 pixel CCDs. The blue side was blazed at 5000 $\AA$ and covered the wavelength range 4900–5340 $\AA$, while the red side was blazed at 7100 $\AA$ and covered the range 6220–6875 $\AA$. The spectral and spatial resolutions were 0.56 $\AA$ and 0.82 $\AA$, and 0.8" and 0.56", on the blue and red sides, respectively.

Between each sky exposure arc lamp exposures were taken to obtain the wavelength calibration and incandescent lamp exposures were taken for the purpose of flat-fielding the data. The r.m.s. of the wavelength calibration was 0.03–0.05 $\AA$ on the blue side, and 0.01 $\AA$ on the red side.

Three one-hour exposures were taken with the slit oriented along the northern half of the major axis of M51 (P.A.=350°) and three exposures of the same duration with the slit oriented at P.A.=270°, close to the western half of the minor axis at P.A.=260° (see Figure 1). The length of the slit is 2'. One end of the slit was

placed near the nucleus for all exposures. Since the emission from M51 extended over the entire length of the slit, separate sky exposures had to be taken between each exposure of M51. Due to a problem of unknown cause, a sensible sky-line subtraction could not be carried out for the third minor-axis exposure; hence it is not used in this analysis.

The data were reduced with standard software from the FIGARO package. Accurate spatial alignment of the exposures was achieved by examining the wavelength-integrated emission profile along the slit of each exposure. The exposures were added after spatial and spectral alignment.

Velocities of the line-emitting gas were obtained using a line-profile fitting routine. Hα and the two NII lines at $\lambda\lambda$6548,6584 were simultaneously fitted, with the ratio of their wavelengths being held constant at the laboratory value. The SII lines at $\lambda\lambda$6717,6731 were also easily detected, but the signal-to-noise ratio of these lines was significantly worse than the Hα and NII lines, so that including them in the fit did not improve the uncertainties. Although both the Hα and NII lines were used in the fitting, we will often refer to the emission line velocities as "Hα velocities." The variation along the slit of fitted wavelengths of sky lines of various strengths provided reliable estimates of the combined uncertainty of the wavelength calibration and line fitting.

Of the absorption lines on the blue side, the strongest was of course the Mg band at $\lambda\lambda$5167,5172,5180, but many weaker FeII lines were also present. The

absorption lines in the disk of M51 were weak enough so that line fitting was unreliable, hence a cross-correlation routine was used to estimate velocities. The template spectrum used was a nuclear spectrum with an excellent signal-to-noise ratio in the absorption lines, and the absolute velocity of this spectrum was found with the line fitting routine. The cross-correlations covered the wavelength range 5020–5300$\AA$, thus avoiding the bright OIII emission line at λ5007. Uncertainties were estimated according to the method described in Tonry and Davis (1977).

For both emission and absorption lines it was necessary to spatially average spectra together before the velocity determinations to improve the uncertainties. The number of spectra averaged depended on the relative signal to noise at each position along the slit. For most of the data, averaging over 5 pixels proved sufficient; however, for the absorption lines beyond 1' from the nucleus, up to 20 pixels (12") had to be averaged together to yield useful uncertainties. For the major axis absorption line data, the resulting uncertainties were too large to allow any peculiar velocities to be determined. These major axis spectra will therefore not be discussed further.

b) The CO Data

The CO observations employed in this paper are described more fully in RK. To summarize, our mosaic cube of CO emission in M51, made with the Millimeter Interferometer of the Owens Valley Radio Observatory (OVRO), covers most of the optical disk with an angular resolution of 8" and spectral resolution of 5.2 km

s^{-1}. The cube is a mosaic of 30 fields, each with a primary beam of 1' (HPBW). The intensity-weighted velocity has been calculated at each 1.5" pixel using NRAO AIPS software to yield a map of the velocity field. Only velocities for pixels meeting a certain signal-to-noise threshold are included in the velocity map.

We also use maps of two of these fields at 2.5" resolution. These high resolution observations are discussed in Rand and Kulkarni (1990b). The two fields include the southern major-axis crossing of the molecular arm. The GMAs near this crossing were unresolved at 8" resolution, but have been resolved in the high-resolution map, allowing a more accurate determination of the tangential streaming velocity gradient across the arm.

c) The K-band Data

For our linear density wave analysis, we use information from the K-band image of Wright *et al.* (1990). We use the K-band light as a tracer of the distribution of stars in the massive old disk. Specifically, we employ the distributions along the directions of the slit in our spectroscopic observations (essentially the major and minor axes). We assume that the position of the K-band nucleus coincides with that of the optical nucleus given by Dressel and Condon (1976).

d) The HI Data

We use the VLA map of 21-cm emission in M51 by Rots *et al.* (1990) with 8" resolution to provide kinematic information on the neutral gas. The velocity

field is computed in the same way as the CO velocity field described above. Again, a velocity is calculated only for pixels in which there is sufficient signal-to-noise to calculate a reliable value.

e) The Fabry-Perot Data

We use new TAURUS-I Fabry-Perot data by Tilanus and Allen (1990) to calculate an $H\alpha$ rotation curve. The field of view of this data set is about 3'. The spatial resolution is 8", and the velocity resolution is about 12 km s^{-1}.

III. Kinematics of the Old Disk and Comparison with Density Wave Theory

Figure 2 shows the velocities derived from the absorption lines along the slit running west from the nucleus (P.A. 270°, close to the minor axis). Qualitatively, the profile shows evidence for two dips in radial velocity which bottom out at $R \approx 25$" and $R = 80 - 90$", in analogy to the gaseous response discussed below, although the dip at $R \approx 25$" is essentially defined by only one data point with a large error bar. The exact location of the second velocity minimum is not well determined, and, in fact, within the errors, the velocity could still be decreasing at the end of the slit. Figure 3 shows the intensity profile from the K-band image along the direction of the slit. From Figure 3, there is indeed a smooth, low-amplitude spiral arm centered at about $R = 85$", with an arm-width of about 30", which is roughly the width of the velocity trough. The extent of this K-band arm is also indicated in Figure 2. Hence we are seeing qualitatively the predicted radial velocity response from linear

density wave theory to the underlying potential as defined by the K-band light distribution, at least in the position and width of the radial velocity minimum.

Since the slit is not exactly aligned with the minor axis there will be a small contribution to the velocity profile of Figure 2 from the rotation curve. To test whether the velocity shift between $R = 30$" and $R = 90$" represents a significant deviation from the rotation curve, we fit a flat rotation curve to the final five points in Figure 2. The best-fit curve has a reduced chi-squared of 5. Therefore, the deviation from a flat profile is significant. Alternatively, the true rotation curve could be rising in this range of galactocentric radius. A rising rotation curve would need a slope of 116 km s^{-1} kpc^{-1} over the region $30" < R < 90"$ to produce the observed shift. If the P.A. of the minor axis were in error by 20° such that the slit was 30° from the minor axis, the required slope of the rotation curve would be 40 km s^{-1} kpc^{-1}. The rotation curves shown in the next subsection rule out such a rotation curve. Finally, the shift could be due to a warp in the disk. However, this explanation is unlikely since this shift is found at $R \approx 4$ kpc, whereas warps are generally found in the outer parts of galaxies.

We now calculate whether the amplitude of the velocity shift is consistent with the predictions of linear density wave theory using the K-band image to trace the old-disk mass. From the equations for the response to the density wave in the linear theory (Lin, Yuan, and Shu 1969), one can derive the following relationship

between the density enhancement and the amplitude of the radial velocity shift for a tight winding spiral:

$$u_R = \frac{\sigma_1}{\sigma} R \tan i \, (\Omega - \Omega_P), \tag{1}$$

where u_R is the amplitude of the radial velocity shift, σ_1 and σ are the surface density amplitude and the unperturbed surface density, R is the galactocentric radius, i is the pitch angle of the spiral pattern, Ω_P is the pattern speed of the spiral, and Ω is the angular rotation frequency. From Tully (1974b), we take $i = 18.5°$ and $\Omega_P = 37$ km s^{-1} kpc^{-1} (for a distance of 9.6 Mpc).

For the K-band arm centered at $R \approx 85$", $\frac{\sigma_1}{\sigma}$ reaches a maximum of about 75%, so $u_R \approx 20$ km s^{-1} is predicted. The expected radial velocity profile from linear theory is sinusoidal, with a wavelength of twice the extent of the K-band arm and centered on it. We therefore find the amplitude of the observed shift by fitting such a sinusoid to the final four data points of Figure 2. The observed shift in the plane of the galaxy found in this way is about 55 km s^{-1} $\pm$ 20 km s^{-1}. There is therefore a significant discrepancy between the observed and predicted shifts. The predicted shift of only 8 km s^{-1} in the plane of the sky is hard to reconcile with Figure 2. The position of the velocity minimum is not well determined from our data.

The failure of the linear theory for this arm has the following possible explanation. Using the fit to the density wave pattern by Tully (1974b), Elmegreen, Elmegreen, and Seiden (1989) determine that the position of the 4:1 resonance of the spiral pattern is at $R = 80$". At this resonance, Contopoulos and Grosbøl

(1986) find that for strong spirals, the stellar orbits become more non-circular and the spiral pattern begins to become washed out (as opposed to the linear theory, which predicts that spirals end at the corotation radius). Hence, from their orbit calculations, one expects larger radial streaming motions and a lower spiral pattern amplitude near the 4:1 resonance than predicted by the linear theory.

Parenthetically, we note that the spiral pattern can be seen in the K-band image to continue beyond this radius. This outer spiral structure is presumably due to the passage of the companion (Toomre and Toomre 1972, Tully 1974b, Elmegreen, Elmegreen, and Seiden 1989).

Although we have seen some kinematic evidence for streaming motions in the old disk, more sensitive data are clearly needed before any firm conclusions can be made about the stellar response to the density wave.

IV. Kinematics of the Gas and Comparison with Density Wave Models

a) The Rotation Curve

The rotation curves derived from our CO velocity field and the HI velocity field are shown in Figure 4. Also shown along with each of these curves in Figure 4 is the Hα rotation curve. Only points within 45° of the major axis have been included in the curves. All three velocity fields used to calculate the rotation curves contain only data above a certain signal-to-noise threshold. Consequently, all three curves

mainly represent velocities of gas on the arms, where the emission is strongest. We have independently solved for the kinematic center and find it to be close to the position of the nuclear radio source found by Ford *et al.* (1985). We also confirm the position angle of the major axis found by Tully (1974a).

The basic features of the three curves agree: both the CO and Hα curves rise steeply for 0" $< R <$ 25" (the central HI hole precludes a determination of the HI rotation curve in this region), and all three show a minimum at $R \approx$ 40" followed by an increase to a peak at $R \approx$ 75". Since only points within 45° of the major axis are included, the curves are very sensitive to tangential streaming motions. In this range of position angles, the gaseous spiral arms are centered at $R \approx$ 20" and $R \approx$ 60" (see Figure 1). Hence all three curves show the expected tangential velocity boost across the arms, with a velocity falloff between the arms. However, there is a significant discrepancy between the rotation curves over the range 45" $< R <$ 75". The CO velocities are lower than the Hα velocities by 20–40 km s^{-1} in this region. The HI velocities are also somewhat lower than the Hα velocities in this range.

To attempt to explain these discrepancies, we first reemphasize that these rotation curves mainly represent on-arm emission. We believe that one reason behind the large discrepancy between CO and Hα velocities is the spatial offset between the molecular and HII region spiral arms reported by VKS and RK. The magnitude of this offset is about 5-10", and the sense is that the HII regions are displaced downstream from the molecular arms. This offset is clear even though the resolution of the CO map is 8". Because of the tangential velocity boost across

the arms, then, the Hα emission, which is concentrated to the back of the arm, should show larger rotational velocities than the CO emission. However, with the resolution of *both* data sets being 8", this spatial offset is found to almost completely vanish. Since the tangential streaming velocity gradient across the arms is very steep ($\sim$ 100 km s^{-1} kpc^{-1} from §V), the smearing of the spatial offset should result in a difference in rotation curves at the position of the arms of about 35 km s^{-1}, assuming the offset has been completely smeared out.

Additional mixing of spatially distinct regions is expected in the rotation curve regardless of the spatial resolution because of the non-zero pitch angle of the arms. A "downstream" HII region from one segment of a spiral arm may lie at the same distance from the nucleus as "upstream" CO emission from further along the arm. Hence, gas at different spiral phases can appear at the same radius in the rotation curve, giving rise to a velocity difference because of the tangential streaming motion. For an Hα-CO spatial offset of 5"–10" and the pitch angle of the inner spiral pattern of M51 of 18.5° (Tully 1974b), Hα and CO emission from the same galactocentric radius will be separated by $15° - 30°$ in azimuthal angle.

Since the HI spiral arms are also offset downstream from the CO arms (RK, Tilanus and Allen 1989), one might expect the HI rotation curve to show better agreement with the Hα rotation curve. This turns out to be the case, although an average discrepancy of about 10 km s^{-1} still exists between the two curves over the range $45" < R < 75"$. From the above discussion, because the velocity gradient across the arms is steep, only a small offset is needed to produce such a gradient.

b) The Major Axis

For our spectroscopic observations, the first slit position was along the northern half of the major axis with one end at the nucleus. In Figure 5 we show velocities of the ionized gas along this segment of the major axis along with velocities of the CO and HI averaged over a 10° sector centered along the northern half of the major axis. Figure 5 also shows the position and extent of the molecular arm from the OVRO map, and the position of the dust lane. Since the basic rotation brings the gas towards the observer along this half of the major axis, higher rotational velocities correspond to lower V_{lsr}s. In gross detail, the Hα velocity profile is reminiscent of the Hα rotation curve discussed above. The peak-to-peak variations in the disk have an amplitude of about 60 km s^{-1} in the plane of the galaxy. The Hα velocities and the positions of the peaks and troughs agree very well with earlier spectroscopy by Goad, DeVeny and Goad (1979; see their Figures 3*a*-*c*). There are some small-scale differences, however, between our spectroscopic profile and the Hα rotation curve of Figure 4. Over the region 45" $< R <$ 65", the Hα V_{lsr}s are lower than expected from the rotation curve, while for 70" $< R <$ 80", they are higher than expected. One could obtain the impression from the spectral velocities alone that the maximum rotation velocity of the ionized gas occurred at about the position of the dust lane, $R \approx$ 55", displaced from the maximum CO and HI rotational velocities. However, the Fabry-Perot data give us confidence that this is not the case. We suspect that the reasons for these small-scale discrepancies are random motions of HII regions and acceleration of the ionized gas out of the plane of the galaxy. These two

effects are plausible since *a)* dense clouds with HII regions may well react differently from diffuse gas to a density wave (Bash and Peters 1976), and *b)* the young OB associations should be able to accelerate gas up out of the plane (for example, Chu and Kennicutt [1990] have reported high-velocity expanding shells in many of the giant HII regions of the Magellanic Clouds). Because of extinction (typically 2 mag for the giant HII regions; van der Hulst *et al.* 1988) we should preferentially see blueshifted rather than redshifted outflowing gas. These peculiar motions would be averaged out in the rotation curve. There are, in fact, HII regions approximately centered at the three positions – 50", 60" and 75" – where the discrepancies are greatest.

The CO and HI velocities also show a falloff from high V_{lsr}s to low V_{lsr}s between $R = 40$" and $R = 60$", as in the rotation curves, with the minimum V_{lsr} occurs at about $R = 70$", displaced from the position of the Hα minimum. The CO and HI velocities agree fairly well for this small segment of the spiral arm. However, this may not be surprising in light of the above discussion because the CO-HI offset in this particular region is practically non-existent (see Figure 1 of Rand, Kulkarni, and Rice 1990). For the inner arm at $R = 20$", the CO velocity trough is not as deep as the Hα trough. Since the trough is rather narrow in Hα, this discrepancy is probably due to beam-smoothing in the CO data.

Finally, we note that within $R = 10$" there is high-velocity ionized gas which has no molecular counterpart. This discrepancy was noted previously by Rydbeck, Hjalmarson, and Rydbeck (1985) from their single-dish CO data at 30" resolution

and the Hα spectroscopy of Goad, DeVeny, and Goad (1979). These latter authors discussed several possible origins for these peculiar velocities, including z-motions of the ionized gas. Since this paper addresses the disk kinematics, the nuclear region will not be discussed further.

b) The Minor Axis

Our second slit position ran west from the nucleus – in other words, 10° away from the kinematic minor axis as inferred by Tully (1974a). Figure 6 shows velocities along this cut through M51 in the same way as Figure 4.

Within $R = 10$", we see once again a high velocity Hα component which has no counterpart in CO. The fact that this discrepancy occurs along both the major and minor axis suggests that the peculiar Hα velocity component is not in the plane of the galaxy, but is more likely to arise from motion perpendicular to the disk. The same conclusion was reached by Goad, DeVeny, and Goad (1979) and Goad and Gallagher (1985). Alternatively, Tully (1974b) modelled the peculiar motions of the ionized gas in the nuclear region as gas streaming in elliptical orbits. Since we are focusing here on the density wave in the disk, we will not address the issue of the gas motions in the nuclear region further.

At the inner arm crossing ($R = 25$") both Hα and CO data show a dip in velocity followed by an increase. The depth of the trough in Hα is about 40 km s^{-1} in the plane of the galaxy. Between the two arms, both Hα and CO show a slow increase in velocity which turns into a decrease as the outer arm is approached. At

the outer arm crossing ($R = 85$") the Hα, CO and HI velocities agree very well and show a decrease followed by an increase as in the inner arm case. The amplitude of the decrease is 125 km s^{-1} and that of the subsequent increase is 25 km s^{-1} in the plane of the galaxy.

d) Comparison with Density Wave Models

We can compare our kinematic profiles with the predictions of nonlinear density wave models. Such models predict that, as a function of position across an arm starting at its inner edge, there should be an increase in the tangential velocity of the gas, and a decrease followed by an increase in radial velocity. These shifts are a consequence of the equation of continuity and angular momentum conservation as the gas responds to the spiral potential.

Figure 7 is taken from Roberts, Lowe, and Adler (1990) and shows the density, tangential velocity, and radial velocity profiles as a function of spiral phase for their simulation of the reaction of a galactic cloud population to a spiral potential. For tightly wound spirals, a cut through spiral phase is nearly equivalent to a cut through galactocentric radius. In this particular simulation the cloud system is allowed to dissipate energy through cloud collisions. The nonlinear response to the $\sim$ 10% spiral perturbation in their simulation is clear: the peak density contrast reaches about 6:1, and the amplitude of the streaming motions is about 40 km s^{-1}. This model predicts that the tangential velocity should increase in the region of peak compression of the molecular gas, and the maximum tangential velocity is

reached beyond the peak compression. This is exactly the behavior seen in Figure 5 for the molecular gas. The observed amplitude of the velocity shift is about 60 km s^{-1} in the plane of the galaxy, somewhat larger than in the simulations of Roberts, Lowe, and Adler (1990) and Roberts and Stewart (1987).

The predicted radial velocity behavior of Roberts, Lowe, and Adler (1990) is shown in the bottom panel of Figure 7. In simulations with dissipative collisions, the sharp radial velocity decrease at the molecular arm is a persistent feature and is characteristic of a large-scale galactic shock. This characteristic "steep drop followed by slow rise" profile can be seen in Figure 6 in the ionized gas response at $R = 25$" and the response of all three tracers at $R = 85$" (although the error bars are sometimes large for CO and HI at the second arm crossing). Hence, the agreement of the observed and predicted profiles is very good. The amplitude of the inner arm velocity shift in Hα, 40 km s^{-1} in the plane of the galaxy, is in good agreement with the simulation. The amplitude of the outer arm shift, however, is about 125 km s^{-1} – much larger than in the simulation. Beam smoothing of the CO velocity profile at $R = 25$" precludes a statement about whether the predicted characteristic response exists in the molecular gas there.

The reason for the very large radial velocity shift in the gas at $R = 85$" may be the same as the reason for the failure of the linear density wave theory for the stars. From a rough calculation, Contopoulos and Grosbøl (1986) expect the same nonlinear effects to occur at the 4:1 resonance for the gas orbits as for the stellar orbits – namely highly non-circular orbits and a washing out of the spiral pattern.

Interestingly, it is very close to this radius where we see a rather abrupt termination of the molecular spiral arms in our CO map on both sides of the galaxy (RK). The break on the west side can also be seen in the single-dish CO (2–1) map of Garcia-Burillo and Guélin (1990), so that it is not an artifact of incomplete coverage of the u-v plane in the interferometric data. The spiral pattern in the molecular gas therefore does wash out at this radius. It is quite possible, then, that the kinematics at this radius are significantly disturbed by the presence of the 4:1 resonance.

V. GMA Formation, Disruption and Star Formation

As mentioned in the Introduction, our CO map of M51 at 8" resolution shows many GMAs of typical mass 3×10^7 $M_\odot$. Two possible formation mechanisms discussed in the Introduction for GMAs and superclouds are large-scale gravitational instability in a clumpy, diffuse medium and collisional agglomeration of preexisting, self-gravitating clouds. The GMAs on the arms appear to be gravitationally bound, while the interarm GMAs are unbound. If the on-arm GMAs are bound, then since they are confined to narrow spiral arms, their formation and destruction timescales must be relatively short. One could imagine that interarm GMAs are the disrupted remnants of GMAs which formed on the arms. However, the interarm GMAs tend to be well separated from the main arms. If we could detect significantly disrupted GMAs as they moved off the arms, we would expect to see more of them at the "back" of the arms, where disruption would just be beginning, and fewer of them further into the interarm region as they become too disrupted to be observable with an interferometer. This is not the case, so we conclude that the interarm GMAs

are not remnants of on-arm GMAs, and that the disruption of on-arm GMAs must be rapid.

The goals of this section are *a)* to quantitatively determine whether the above-mentioned processes are viable mechanisms for building bound GMAs, *b)* to discuss how the triggering of star formation might be related to GMA formation, and *c)* to discuss the difficulties with the conclusion that they are bound, particularly the problem of their destruction.

a) Gravitational Stability Analysis

Our first goal is to test the viability of the instability theory for GMA formation by simply calculating whether the on-arm and interarm gas in M51 should be unstable to collapse by K89's criterion and to calculate the expected characteristic masses. In the next subsection, we calculate the collapse timescales in the arms and interarms, and compare these with the time required to build up GMAs by collisional agglomeration. These GMA building timescales are then compared with the time available for the growth of GMAs in the arm and interarm regions. The time available may be limited by shear forces or the amount of time the gas spends on the arms.

The threshold surface density for gravitational instability as given by K89 is essentially the simple Toomre (1964) stability criterion:

$$\Sigma_c = \alpha \frac{\kappa c}{3.36G} \qquad (2)$$

where Σ_c is the threshold surface density, κ is the epicyclic frequency and c is the gas velocity dispersion. The parameter α is a constant near unity (K89) which is included to account for the effects of two-fluid (gas and stars) instabilities. Jog and Solomon (1984) have demonstrated that the two-fluid system may be unstable even if each of the components, treated individually, is not. This increased tendency toward instability is accounted for by values of α below unity. Jog and Solomon give a more exact treatment of the two-fluid problem.

Naturally, since the on-arm gas has a higher surface density, it is much more likely to be unstable than the interarm gas. However, κ also changes between the arm and interarm regions because of the streaming motions induced by the density wave. For gas with orbital velocity v at galactocentric radius R,

$$\kappa = \sqrt{2}\frac{v}{R}(1 + \frac{R}{v}\frac{dv}{dR})^{1/2}. \qquad (3)$$

We first evaluate the stability criterion for M51 using the axisymmetrically averaged gas density and rotation curve. We use the parametrization of the molecular gas surface density by Lord (1987), $\Sigma_{H_2} = 210/R$ $M_\odot$ pc^{-2} (R in kpc), and a flat rotation curve from §2 of 200 km s^{-1}. We assume that $\alpha = 0.7$ (the value determined by K89). From our 2.5" resolution CO observations, we measured a one-dimensional velocity dispersion of 10 km s^{-1}. We therefore assume that $c = 10\sqrt{3} = 17$ km s^{-1}. One should keep in mind that errors of a factor of 2 may be introduced by these assumptions. We find that $\Sigma_c = 215/R$ $M_\odot$ pc^{-2}, so that the gas is roughly at the instability threshold throughout the disk.

However, this conclusion is modified by the existence of density waves. Balbus and Cowie (1985) demonstrate for a tight winding spiral that because mass and angular momentum are conserved as the gas passes through the zone of compression, the epicyclic frequency is related to the gas surface density by $\kappa^2 \propto \Omega\Sigma$, where Ω is the rotation frequency (see also Balbus 1990). As gas flows in and out of arms, the change in Ω is much less than the change in Σ, so that approximately, $\kappa^2 \propto \Sigma$. Because of tangential streaming, dv/dR is non-zero in equation (3). Therefore from measurements of the tangential streaming, we can compare the on-arm and axisymmetric values of κ and calculate the enhancement in surface density on the arms relative to the unperturbed value. Then, by mass conservation, as a fluid element passes in and out of the spiral arms, $\Sigma_i A_i$ is constant, where Σ_i and A_i are the surface density and surface area of fluid element i. Hence $\Sigma_{arm} A_{arm} = \Sigma_{int} A_{int} = 1/2\Sigma_0 A$, where the three subscripts refer to arm, interarm, and unperturbed quantities respectively, and $A = A_{arm} + A_{int}$. With these equations, it is easy to solve for the arm-interarm contrast in surface density.

We now reevaluate the stability criterion at a galactocentric radius of 2.7 kpc, where we have measurements of the tangential streaming motions. For the north side, the CO streaming motions indicate $dv/dR \approx 60$ km s^{-1} kpc^{-1} at this radius, so that κ is increased over its axisymmetric value by a factor of 1.4, and Σ is increased by 1.9. Hence, we deduce an arm-interarm contrast in surface density of 2.7. The corresponding arm-interarm contrast in κ is then 1.6.

From the high-resolution CO data, the tangential velocity gradient at the southern major-axis crossing is $dv/dR = 130$ km s^{-1} kpc^{-1} so that κ is increased over its axisymmetric value by a factor of 1.7. The arm-interarm contrast in Σ is therefore 4.7, and in κ, 2.2.

Note that although the increase in κ alone would make the gas in the arms more stable against collapse (equation [3] can be reexpressed to show that κ is proportional to the local angular momentum gradient, and it is angular momentum which stabilizes the gravitational perturbations), the increase in Σ is always greater than that in κ so that on-arm gas is always more gravitationally unstable than interarm gas. We reemphasize that these arm-interarm contrasts are only approximate because of the "tight-winding" approximation, which is valid for $cot\, i >> 1$, where i is the pitch angle of the spiral arms. For $i = 18.5°$ Tully (1974b), $cot\, i \approx 3$, so the approximation is only marginally valid.

With these numbers, and Lord's (1987) parametrization of the surface density, the threshold surface density on the arms at $R = 2.7$ kpc is $\Sigma_c = 110$ M$_\odot$ pc^{-2}, while the actual surface density is $\Sigma_{H_2} = 150$ M$_\odot$ pc^{-2}. Between the arms, $\Sigma_c = 70$ M$_\odot$ pc^{-2}, while $\Sigma_{H_2} = 55$ M$_\odot$ pc^{-2}. On the south side, $\Sigma_c = 130$ M$_\odot$ pc^{-2} and $\Sigma_{H_2} = 220$ M$_\odot$ pc^{-2} on the arms while $\Sigma_c = 60$ M$_\odot$ pc^{-2} and $\Sigma_{H_2} = 45$ M$_\odot$ pc^{-2} between the arms. Therefore, the on-arm gas may well be unstable by this criterion, while the interarm gas may be close to the threshold. From this analysis, then, large-scale gravitational instability remains a plausible mechanism for the triggering of GMA formation (and possibly star formation) by the density wave. The role

of the suggested secondary density-wave compression which may be responsible for the interarm GMAs might then be to push the surface density slightly above the threshold, leading to weaker instabilities than on the main arms.

The characteristic mass of the instabilities is the Jeans mass: $M_J = \pi c^4/G^2\Sigma$ (Elmegreen 1987a). Using the above parameters for $R = 2.7$ kpc, we calculate Jeans masses of $M_J = 7\times10^7$ $M_\odot$ on the arms and $M_J = 2.5\times10^8$ $M_\odot$ between the arms. Since the Jeans mass is very sensitive to the sound speed, the calculated masses are rather uncertain, especially in the interarms where we have no direct estimate of the sound speed. If the sound speed is lower by a factor of two in the interarms, then the characteristic interarm mass agrees well with the typical interarm GMA mass.

b) GMA Formation Timescales

In the previous subsection, we demonstrated that the gas on the arms may indeed be gravitationally unstable to collapse, possibly explaining the existence of bound GMAs and the enhancement in star formation efficiency. We also found that the interarm gas may be close to the point of marginal instability. However, we have not yet demonstrated that there is sufficient time available while the gas is on the arms to form bound GMAs by either gravitational instability or agglomeration and thus explain their concentration to the arms. Neither have we explained the unbound nature of the interarm GMAs. These are the goals of this subsection.

In the gravitational instability theory (*e.g.,* Toomre 1964; Balbus and Cowie 1985; Elmegreen 1990a), clouds collapse out of the gas and become self-gravitating on a timescale of about twice the Jeans timescale,

$$T_{grav} = 2T_J = c/(\pi G\Sigma) \tag{4}$$

(*e.g.,* Elmegreen 1990a). Using the parameters in the above discussion for $R = 2.7$ kpc, we find $T_{grav} = 7 \times 10^6$ yr on the arms and $T_{grav} = 2.6 \times 10^7$ yr between the arms.

Elmegreen (1990b) has calculated the time to build up a large cloud of a given mass from initially smaller, self-gravitating clouds. For an on-arm surface density of 180 $M_\odot$ pc^{-2} and a gas layer with a half thickness of 100 pc, and assuming the size spectrum of clouds has a power-law exponent equal to the Galactic value, a GMA can be built up on the arms through collisions as fast as by gravitational instability if the initial (interarm) mass spectrum extends up to $\sim 10^5$ $M_\odot$.

The time available for the growth of on-arm and interarm GMAs by either process may be limited by the time the gas spends on (or between) the arms or the shear timescale (Elmegreen 1988). In general, the shear due to differential rotation will tend to disrupt growing instabilities, but because of the tangential velocity boost in the gas on the arms caused by the density wave, the shear timescale can be much longer than the value for a flat rotation curve. The shear timescale is simply proportional to the inverse of the Oort A constant, and is the time required for two

fluid elements separated radially by dR to move apart in the tangential direction by dR:

$$T_{sh} = (-Rd\Omega/dR)^{-1} = (v(R)/R - dv(R)/dR)^{-1}. \quad (5)$$

Note that for solid-body rotation, the shear timescale is infinite, *i.e.,* there is no shear. At 2.7 kpc from the nucleus, as mentioned above, the velocity gradient due to the tangential streaming is $dv/dR = 60$ km s^{-1} kpc^{-1} at the northern major-axis crossing, and $dv/dR = 130$ km s^{-1} kpc^{-1} at the southern crossing. Therefore, while the shear timescale for a flat rotation curve of 190 km s^{-1} would be about 1.4×10^7 yr, with the tangential streaming, it is increased on the north side to 10^8 yr. Locally, then, the rotation curve is closer to the solid-body case because of the tangential streaming. On the south side, the streaming is great enough so that a condition of reverse shear exists, and the timescale remains relatively unchanged at about 1.7×10^7 yr.

The amount of time the gas spends on the arm is given by the fraction of time spent in the arm, $\frac{\alpha}{1+\alpha}$, times the time to flow from arm to arm, $\frac{2\pi}{m(\Omega-\Omega_p)}$, where $m = 2$ for a two-armed spiral:

$$T_{arm} = \frac{\pi\alpha}{(1+\alpha)(\frac{v}{R} - \Omega_p)} \quad (6)$$

where α is the arm-interarm contrast, and Ω_p is the pattern speed. Using Tully's (1974b) determination of the pattern speed in M51 scaled to our adopted distance of 9.6 Mpc ($\Omega_p = 38$ km s^{-1} kpc^{-1}), and the average arm-interarm contrast at

2.7 kpc of 3.7 from above, we find $T_{arm} = 10^8$ yr. Thus the gas spends about one rotation period in the arms at this radius. The time spent between the arms is

$$T_{interarm} = \frac{\pi}{(1+\alpha)(\frac{v}{R} - \Omega_p)} \tag{7}$$

or 2×10^7 yr.

The various timescales calculated above are reproduced in Table 1. There is sufficient time, then, to form GMAs by either process on the arms at this typical radius, although the gravitational instability timescale is several times shorter. It is possible that both processes are acting simultaneously on the arms: the self-gravity of the gas may force the growing agglomerations to merge more rapidly into even larger agglomerations (Elmegreen 1987a).

The timescale for a GMA to virialize depends on its energy dissipation rate. If the dissipation occurs primarily in collisions of clouds, then the dissipation timescale will be roughly $T_{diss} = R/fc$, where R is the typical cloud radius, f is the volume filling factor of the clouds, and c is the velocity dispersion (Elmegreen 1988). If the typical cloud has a mass (4×10^5 $M_\odot$) and radius (20 pc), characteristic of a typical Galactic GMC (Scoville and Sanders 1987) and the full-thickness of the gas layer is 150 pc, then the volume filling factor is about 0.1. The dissipation timescale is then $T_{diss} \approx 10^7$ yr, which is short compared to the shear and arm-flow-through timescales, so that the GMAs should be able to virialize while they are on the arms.

Between the arms, there is probably not enough time to build a GMA through either collisional agglomeration or gravitational collapse. Therefore, GMA formation should be generally inhibited between the arms. There are, however, GMAs observed between the arms, and we have presented evidence (RK) that they are formed by a weak, secondary compression of the density wave. If the interarm GMAs are formed in this way, then they are not "true" interarm GMAs since they owe their existence to a density wave compression, albeit a weak one. For weak compressions, the period of growth by either process will be more severely limited by shear and the shorter arm residence time than in the strong compression case. If the interarm GMAs are formed in this way, then the compression could be sufficient to bring the surface density somewhat over the threshold and cause mild gravitational instabilities. Alternatively, they could be transient features temporarily brought together by crowding of cloud orbits. The fact that they are unbound could then be understood as being due to the insufficient time available to form a bound GMA by either gravitational instability or agglomeration.

c) Star Formation

Star formation will follow only after the gas has dissipated enough energy to allow dense cores to form. In the gravitational instability scenario, continued fragmentation is expected to occur after the formation of the largest structures as a result of energy dissipation, eventually leading to the formation of dense cores. The dissipation is provided by collisions of small, diffuse clouds. The rate of energy loss therefore goes as the square of the gas density and occurs at an increased

rate on the arms (the dissipation rate within a bound GMA should be even higher than in on-arm gas between the GMAs). Hence, GMA formation and density wave triggering of star formation can be explained in this way, as would K89's generally observed nonlinear Schmidt law above the star formation threshold. Alternatively, if the dense cores form at the interface of colliding, self-gravitating clouds, then the star formation rate should be proportional to the square of the number density of such clouds, thus providing the mechanism for density wave triggering of star formation. Again, both GMA formation and the triggering of star formation would be consequences of one physical process, in this case cloud-cloud collisions.

d) Are the GMAs Really Bound?

So far, we have presented calculations and arguments to show how bound on-arm GMAs and unbound interarm GMAs might form. In this subsection, we address the issue of whether or not the GMAs are actually bound, and the difficulties associated with each conclusion.

If the GMAs are bound, then it is curious that the tangential and radial streaming motions observed across them are virtually the same as those across the arm material *between* the GMAs (see Figure 2 of VKS). Some of the tangential velocity shift in the GMAs could be due to rotation, but the signature of rotation is not seen in the radial velocity shift of GMAs near the minor axis. A cut across the minor axis GMA A3 (see RK) *along* the direction of the arm is shown in Figure

8. No large radial gradient is seen which would indicate significant rotation. The velocity shifts across the GMAs, then, are due to density-wave streaming.

If the gravitational binding energy of a GMA is indeed greater than the kinetic energy associated with the systematic shear across it (Rand and Kulkarni 1990b), then the shear energy should be dissipated or converted to random motions or rotation as the GMA forms. Otherwise, the shear would simply disrupt the GMA on a shear timescale. It is strange, then, that we would observe the GMAs after significant condensation has taken place but before the shear has been removed. Why don't we observe any GMAs at a later stage with relatively little shear? Are they disrupted rapidly enough by some other agent before the shear disappears? We believe that these are important problems with the finding from the virial theorem that the GMAs are bound.

We now consider the rapid disruption of bound GMAs, which is necessary to explain their confinement to narrow spiral arms.

It was shown in Rand and Kulkarni (1990b) that the GMAs are probably stable against disruption by tidal forces while on the arms. The tidal forces should increase when the GMAs move off the arms. However, it is not clear whether the GMAs will be tidally disrupted. The tides will increase both because the tangential streaming reverses itself (Figure 6), leading to a larger value of A, and because there will be some radial migration to lower R as the GMAs slowly drift through the arm region. Assuming the tangential streaming reverses sharply as the gas moves off the arms, such that the velocity gradient becomes $dv/dR = -60$ km s^{-1} kpc^{-1} (as

indicated by the regions of negative dv/dR in Figure 6), then the minimum density for tidal stability, $A\Omega/G$, is 5×10^{-23} g cm^{-3} at $R = 2.5$ kpc. The density of a 3×10^7 M$_\odot$ mass GMA with diameter 300 pc is about 10^{-22} g cm^{-3}. Hence, there is at best rough equality of the true and tidal densities at the back of the arms, so it is unclear whether the GMAs would become unstable to disruption by tides.

The other possible mechanism for disrupting bound GMAs is star formation. We can present some plausibility arguments that star formation can provide sufficient energy and momentum to disrupt GMAs. However, the arguments are by no means conclusive.

The typical binding energy of a GMA is $\sim 10^{53}$ erg. For a conservative true star formation efficiency of 1% (the value estimated for the central 50" of M51 by Thronson and Greenhouse 1988), a GMA should produce about 10^4 OB stars in its lifetime, assuming a Salpeter mass function. These OB stars will return energy to the ISM via winds and supernovae. Typical stellar wind parameters for Galactic OB stars are a mass loss rate per OB star of 3×10^{-6} M$_\odot$/yr and a wind velocity of 1000 km s^{-1} (*e.g.*, Bieging, Abbott, and Churchwell 1989). Therefore, the mechanical energy input in winds should be $\sim 3 \times 10^{54}$ erg. Supernovae from this many OB stars will release roughly an additional $\sim 10^{54}$ erg. Hence, there is sufficient energy in stellar winds and supernovae to disrupt a GMA, as long as the efficiency of coupling between the kinetic energy output and the bulk motion of the gas is not too low. The momentum associated with stellar winds is $\sim 3 \times 10^4$ M$_\odot$ km s^{-1} per OB star, and from supernovae $\sim 2 \times 10^4$ M$_\odot$ km s^{-1} per OB star, assuming 2 M$_\odot$

of ejecta at 10^4 km s^{-1}. The total momentum input is therefore $\sim 5 \times 10^8$ $M_\odot$ km s^{-1}. This is roughly equal to the momentum necessary to draw apart a GMA at a velocity of 10 km s^{-1}. Hence, these minimum energy and momentum requirements are crudely satisfied. If the fragments of the GMA are drawn apart at a velocity of 10 km s^{-1}, then significant disruption could occur in about 3×10^7 yr after star formation begins.

A major uncertainty is the efficiency with which the energy output of winds and supernovae is coupled to the bulk motion of the gas. Typical values in the literature are 1–3% for expansion into relatively dense media (Chevalier 1974, Spitzer 1978). However, these values are sensitive to the efficiency of the cooling processes, which may be more efficient if the medium is predominantly molecular, as is the case in M51 (Rand, Kulkarni, and Rice 1990).

The efficiency may be higher if the winds and supernovae are correlated in space and time. The OB associations which power the giant HII regions in M51 could create superbubbles and thus evacuate large regions around them. MacLow and McCray (1988) calculate that the kinetic energy of the cold shell surrounding a hot superbubble is 10–20% of the input energy from the supernovae. From the formulae given in MacLow and McCray (1988), we can estimate the diameter and expansion velocity of a superbubble shell in M51 in the "supernova phase" of its lifetime. Using simple scaling relations of Kennicutt, Edgar, and Hodge (1989), we find that an OB association responsible for a typical giant HII region on the inner arms (see van der Hulst *et al.* [1988] for HII region fluxes and extinctions) should

contain about 500 OB stars. For 500 supernovae in 10^7 yr, and an ambient medium with density 20 cm^{-3}, the diameter of the superbubble and the expansion velocity should be $\sim$ 300 pc and $\sim$ 10 km s^{-1}. Hence, the correlated power of winds and supernovae are relatively effective in disrupting the local ISM. Again, an uncertainty is the rate of radiative cooling when the ambient medium is predominantly molecular. A greater fraction of the input energy may be radiated away rather than being converted into bulk motion of the gas in this case because of the efficient molecular cooling.

It is therefore plausible, at least, that star formation provides sufficient input energy into to ISM to disrupt bound GMAs, although there are many uncertainties.

If the GMAs are *unbound*, then their disruption is not as problematic. As is presumably the case for the detected on-arm material between the GMAs, the shear and expansion of the underlying flow will eventually disrupt them into a diffuse enough state to be undetectable with the OVRO Millimeter Interferometer. No special agent, such as star formation, need be invoked for their disruption.

The fragmentary appearance of the molecular spiral arms suggests that the self-gravity of the gas is important, even if the fragments (GMAs) are not bound. In fact, this is precisely the case in the N-body simulations of Roberts, Adler, and Stewart (1990), who simulate the reaction of a cloud population to an imposed spiral potential. In their simulations in which the self-gravity and dissipative collisions are included, the arms do show a fragmentary appearance. The fragments, however, are

only temporary, loose associations of clouds, brought together by their collective self-gravity, and they disperse upon leaving the arms. It is not clear, however, that if a simulation were run with the very high gas surface density of M51, these associations would not be able to become bound. The surface density is an important parameter since the collision and dissipation rates depend on the square of the number density of clouds. The high surface density in M51 implies that instability rates and collision rates will be much faster than in a more normal spiral.

The upshot of this discussion is that it is difficult to state with any certainty whether or not the GMAs are bound, virialized entities. The virial theorem indicates boundedness, and the analysis in this section shows that it is plausible that bound GMAs may form on the arms by gravitational instability or collisional agglomeration. However, their subsequent disruption remains problematic. Simulations of the response of the cloudy ISM to the density wave, with parameters appropriate for M51, would help in determining whether massive structures with approximately equal virial and molecular masses can be produced in a density wave compression, and whether they are truly bound or can be disrupted when the flow expands and the orbits diverge.

Disruption of interarm GMAs is not as problematical since they never become bound. Shear and diverging orbits as the gas passes out of the minor compression should pull them apart.

VI. Conclusions

We have presented new kinematic observations of the response of the old-disk stars and various gas components to the density wave in M51, and we have compared our results with the predictions of linear and nonlinear density wave theory.

We have found some evidence for density-wave induced radial streaming motions in the old-disk stars. We find quantitative deviations from the predictions of linear density wave theory and support for the predicted nonlinear stellar response associated with the 4:1 resonance. Very sensitive data are needed for such absorption line kinematic studies and we expect that more detailed studies will be made possible with the advent of large telescopes in the near future.

We have found much evidence for large-amplitude streaming motions as predicted by density wave theory in the molecular, neutral, and ionized gas. We suspect that motions of the ionized gas out of the plane of M51 and random motions of HII regions are the cause of the detailed discrepancies in the kinematic profiles. The on-arm streaming motion profiles agree well with the predictions of nonlinear, density wave simulations with dissipative cloud-cloud collisions, although the amplitudes of the velocity shifts are often greater than in the simulations. Nonlinear effects associated with the 4:1 resonance may be the cause for the very large radial velocity shift at the minor-axis crossing of the molecular arm at 80" from the nucleus. At this same crossing, the molecular emission peak appears to be shifted upstream from the position of the potential minimum as inferred from the K-band image, in agreement with nonlinear hydrodynamic calculations.

Both gravitational instability and collisional agglomeration are viable mechanisms for producing bound GMAs on the arms. There are problems, however, with the conclusion that the on-arm GMAs are bound. The shear observed across them must somehow eventually be removed, otherwise it would disrupt them in a finite amount of time ($\sim 2 \times 10^7$ yr for the southern arm), so that they would not be truly bound. It is plausible that star formation can disrupt bound GMAs, especially if the stellar winds and supernovae are correlated in space and time, but there are many uncertainties. If the on-arm GMAs are actually unbound, then the shear and expansion of the underlying flow will naturally disrupt them. This is presumably the case for the unbound interarm GMAs. An auxiliary result of our GMA formation analysis is that the arm-interarm contrast in the molecular gas as inferred from the tangential streaming motions is 3–5.

Acknowledgements

We thank John Thorstensen for very helpful discussions and assistance in the cross-correlation analysis of the absorption line spectra. We thank Gillian Wright for providing intensity profiles from the UKIRT K-band image of M51, and Arnold Rots for providing us with the HI data. Remo Tilanus is thanked for providing us with the velocity field from his Fabry-Perot data.

Table 1. Timescales

Timescale	Arm	Interarm
T_{grav}	7×10^6	3×10^7
T_{shear}	1×10^8 1.7×10^7	7×10^6
T_{arm}	1×10^8	–
$T_{interarm}$	–	2×10^7

NOTE TO TABLE 1: All timescales are in years. Where two entries are given, the first refers to the northern major axis crossing, and the second to the southern crossing.

References

Balbus, S. A. 1990, in *The Interstellar Medium in Galaxies*, eds. H. A. Thronson and J. M. Shull (Dordrecht:Kluwer), p. 305.

Balbus, S. A., and Cowie, L. L. 1985, *Ap. J.*, **297**, 61.

Bash, F. N., and Peters, W. L., *Ap. J.*, **205**, 786.

Bieging, J. H., Abbott, D. C, and Churchwell, E. B. 1989, *Ap. J.*, **340**, 518.

Chevalier, R. A. 1974, *Ap. J.*, **188**, 501.

Chu, Y.-H., and Kennicutt, R. C. 1990, in *The Magellanic Clouds and Their Dynamical Interaction with the Milky Way*, eds. R. F. Haynes and D. K. Milne (Dordrecht: Kluwer), in press.

Contopoulos, G., and Grosbøl, P. 1986, *Astr. Ap.*, **155**, 11.

Dressel, L. L., Condon, J. J. 1976, *Ap. J. Suppl.*, **31**, 187.

Elmegreen, B. G. 1987a in *I.A.U. Symposium No. 115, Star Forming Regions*, ed. M. Peimbert and J. Jugaku (Dordrecht: Reidel), p. 457-481.

Elmegreen, B. G. 1987b, *Ap. J.*, **312**, 626.

Elmegreen, B. G. 1988, in *Comets to Cosmology*, ed. A. Lawrence (Berlin: Springer Verlag), p. 186.

Elmegreen, B. G. 1990a, in *The Evolution of the Interstellar Medium*, ed. L. Blitz, Astronomical Society of the Pacific Publishers, in press.

Elmegreen, B. G. 1990b, preprint.

Elmegreen, B. G., Elmegreen, D. M., and Seiden, P. E. 1989, *Ap. J.*, **343**, 602.

Ford, H. C., Crane, P. C., Jacoby, G. H., Lawrie, D. G., and van der Hulst, J. M. 1985, *Ap. J*, **293**, 132.

Goad, J. W., and Gallagher J. S. 1985, *Ap. J.*, **297**, 98.

Goad, J. W., DeVeny, J. B., and Goad, L. E. 1979, *Ap. J. Suppl.*, **39**, 439.

Garcia-Burillo, S. and Guélin, M. 1990, preprint.

Jog, C. J., and Solomon, P. M. 1984, *Ap. J.*, **276**, 127.

Kennicutt, R. C. 1989, *Ap. J.*, **344**, 685 (K89).

Kennicutt, R. C., Edger, B. K., and Hodge, P. W. 1989, *Ap. J.*, **339**, 761.

Kwan, J., and Valdes, F. 1983, *Ap. J.*, **271**, 604.

Kwan, J., and Valdes, F. 1987, *Ap. J.*, **315**, 92.

Lin, C. C., Yuan, C., and Shu, F. H. 1969, *Ap. J.*, **155**, 721.

Lord, S. D. 1987, Ph.D. Thesis, Univ. of Massachusetts.

MacLow, M. and McCray, R. 1988, *Ap. J.*, **324**, 776.

Quirk, W. J. 1972, *Ap. J. (Letters)*, **176**, L9.

Rand, R. J., and Kulkarni, S. R. 1990a, *Ap. J. (Letters)*, **349**, L43 (RK).

Rand, R. J., and Kulkarni, S. R. 1990b, in preparation.

Rand, R. J., Kulkarni, S. R., and Rice, W. 1990, *submitted to Ap. J.*

Roberts, W. W., Adler, D. S., and Stewart, G. R. 1988, in *Applied Mathematics, Fluid Mechanics, Astrophysics*, eds. D. J. Benney, F. H. Shu, and C. Yuan (Singapore: World Scientific), p. 373.

Roberts, W. W., Lowe, S. A., and Adler, D. S. 1990, in *Galactic Models*, eds. J. R. Buchler, S. T. Gottesman, and J. H. Hunter (New York Academy of Sciences), p. 130.

Roberts, W. W., and Stewart, G. R. 1987, *Ap. J.*, **314**, 10.

Rots, A. H., Bosma, A., van der Hulst, J. M., Athanassoula, E., and Crane, P. C. 1990, *A. J.*, **100**, 387.

Rydbeck, G., Hjalmarson, A., and Rydbeck, O. E. H. 1985, *Astr. Ap.*, **144**, 282.

Sandage, A., and Tammann, G. A. 1975, *Ap. J.*, **196**, 313.

Scoville, N. Z., and Sanders, D. B. 1987, in *Interstellar Processes*, ed. D. Hollenbach and A. Thronson (Dordrecht: Reidel), p. 21.

Scoville, N.Z., Sanders, D.B., and Clemens, D.P. 1986, *Ap. J. (Letters)*, **310**, L77.

Shu, F. H., Milione, V., and Roberts, W. W. 1973, *Ap. J.*, **183**, 819.

Spitzer, L. J. 1978, *Physical Processes in the Interstellar Medium* (New York: Wiley)

Thronson, H. A., and Greenhouse, M. A. 1988, *Ap. J.*, **327**, 671.

Tilanus, R. P. J., and Allen, R. J. 1989, *Ap. J. (Letters)*, **339**, L57.

Tilanus, R. P. J., and Allen, R. J. 1990, *submitted to Astr. Ap.*

Tomisaka, K. 1987, *Pub. A. S. Japan*, **39**, 109.

Tonry, J., and Davis, M., *A. J.*, **84**, 1511.

Toomre, A. 1964, *Ap. J.*, **139**, 1217.

Toomre, A., and Toomre, J. 1972, *Ap. J.*, **178**, 623.

Tully, R. B. 1974a, *Ap. J. Suppl.*, **27**, 437.

Tully, R. B. 1974b, *Ap. J. Suppl.*, **27**, 449.

van der Hulst, J. M., Kennicutt, R. C., Crane, P. C., and Rots, A. H. 1988, *Astr. Ap.*, **195**, 38.

Visser, H. C. D. 1980, *Astr. Ap.*, **88**, 159.

Vogel, S. N., Kulkarni, S. R., and Scoville, N. Z. 1988, *Nature*, **334**, 402 (VKS).

Wright, G. S., Casali, M. M., Walther, D. M., and McLean, I. S. 1990, preprint.

Figure Captions

FIG. 1. An Hα CCD image of M51 indicating the positions of the slit for the spectroscopic observations.

FIG. 2. Velocity profile along the slit running west from the nucleus (10° away from the minor axis) for the old-disk stars. The origin is at R. A. = $13^h\ 27^m\ 46.4^s$, Dec. 47° 27' 13" (1950). The arrows indicate the rough extent of the outer K-band arm. Increasing V_{lsr} corresponds to increasing radial velocity. Density wave theory predicts radial velocity dips followed by rises at the positions of the arms.

FIG. 3. Cut through the K-band image of Wright *et al.* (1990) along the extent of the minor-axis slit. The cut has been smoothed to 3" resolution.

FIG. 4. *a)* Inner disk rotation curve for CO (open circles) and Hα (closed circles), and *b)* inner disk rotation curve for HI (open squares) and Hα (closed circles). The molecular velocities are taken from the 8"-resolution map of CO emission by Rand and Kulkarni (1990b). The neutral gas velocities are from the 8" HI map of Rots *et al.* (1990). The Hα velocities are from the Fabry-Perot data of Tilanus and Allen (1990).

FIG. 5. Velocity profile along the slit running along the northern half of the major axis for the ionized gas (solid circles), molecular gas (open circles) and neutral gas (open squares). The origin is at R. A. = $13^h\ 27^m\ 46.3^s$, Dec. 47° 27' 12" (1950). The solid arrows show the extent of the molecular arm. The dashed arrow shows the position of the dust lane. Increasing V_{lsr} corresponds to decreasing tangential

velocity. The tangential velocity increase across the arms and the decrease between the arms are in the sense predicted by density wave theory.

FIG. 6. Velocity profile along the slit running west from the nucleus (10° away from the minor axis) for the ionized, molecular and neutral gas. The origin is as in Figure 2. The symbols are as in Figure 5. Increasing V_{lsr} corresponds to increasing radial velocity. The radial velocity dips and rises at the positions of the arms are in the sense predicted by density wave theory.

FIG. 7. A reproduction of Figure 3 of Roberts, Lowe, and Adler (1990) showing as a function of spiral phase (essentially radius for a tight-winding spiral), from top to bottom, the density contrast, velocity profile parallel to the arms (essentially the tangential velocity), and velocity profile perpendicular to the arms (essentially the radial velocity) in their simulation of the response of a dissipative cloud population to a spiral density wave. Reprinted by permission of the New York Academy of Sciences.

FIG. 8. Cut across the minor axis GMA A3 along the direction of the arm (essentially the tangential direction). The lack of a large gradient indicates that there is no detectable rotation in the GMA.

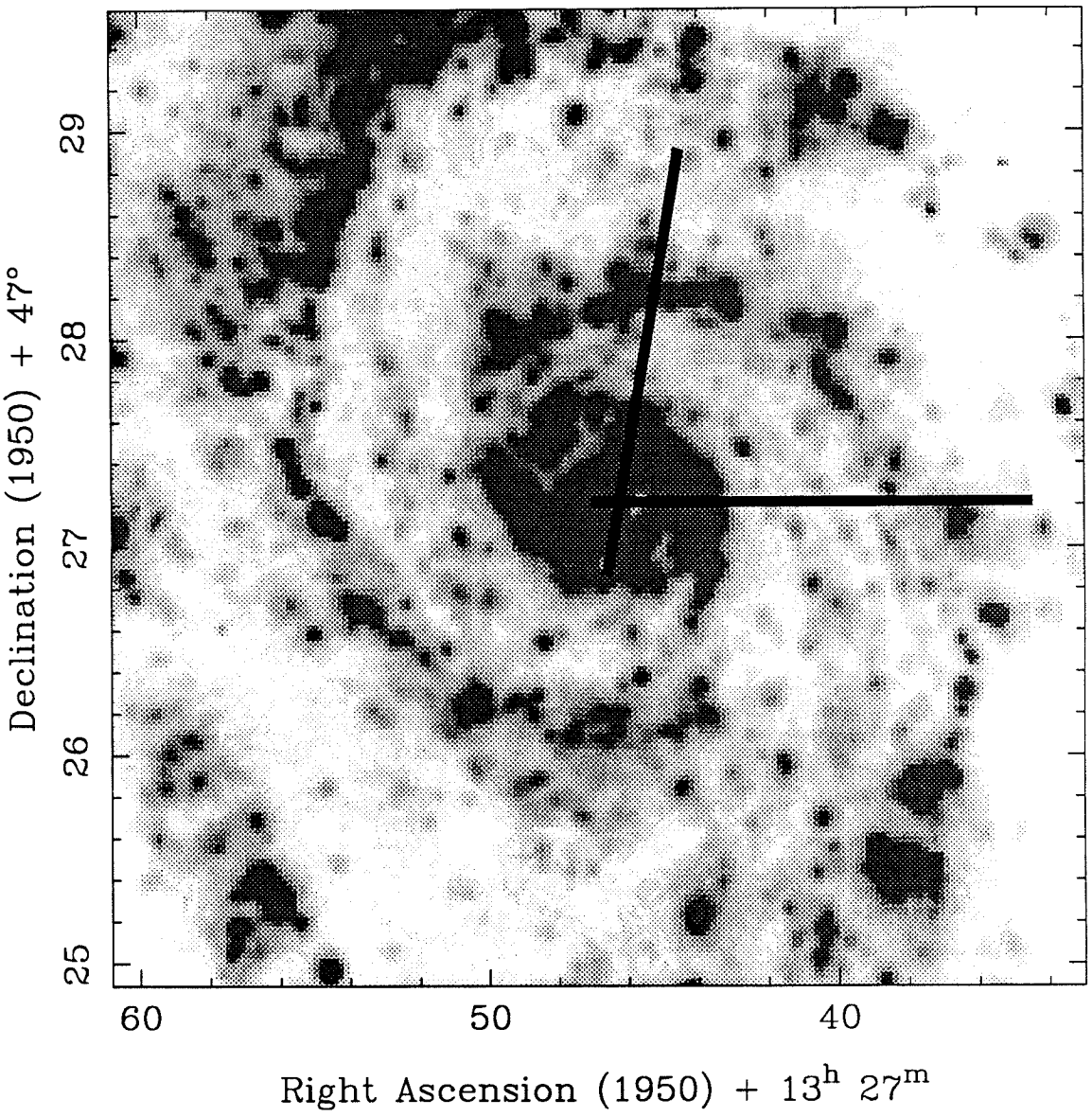
Declination (1950) + 47°
29
28
27
26
25
60
50
40
Right Ascension (1950) + 13h 27m

Figure 1

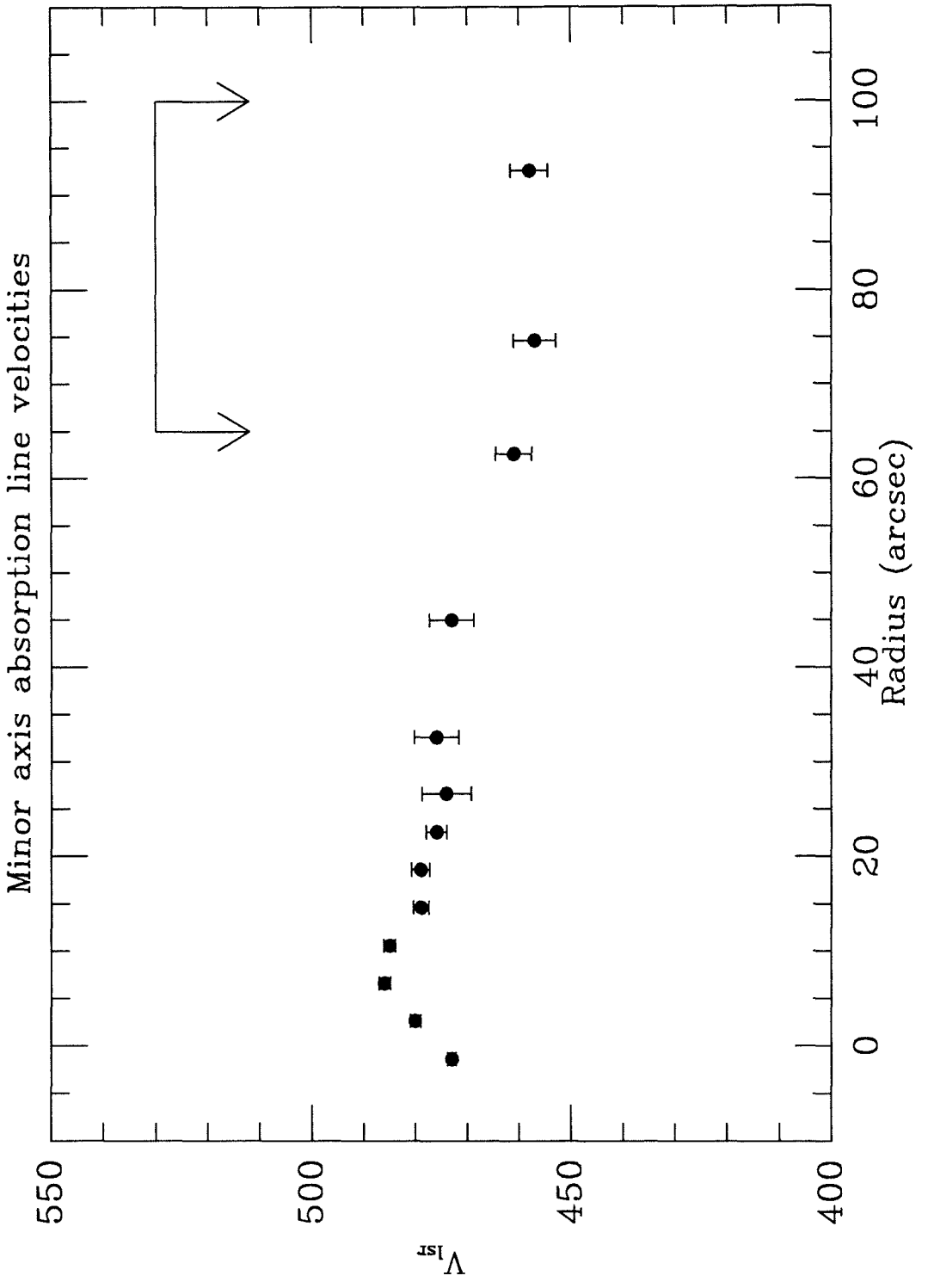
Minor axis absorption line velocities
V_{lsr}
550
500
450
400
0
20
40
60
80
100
Radius (arcsec)

Figure 2

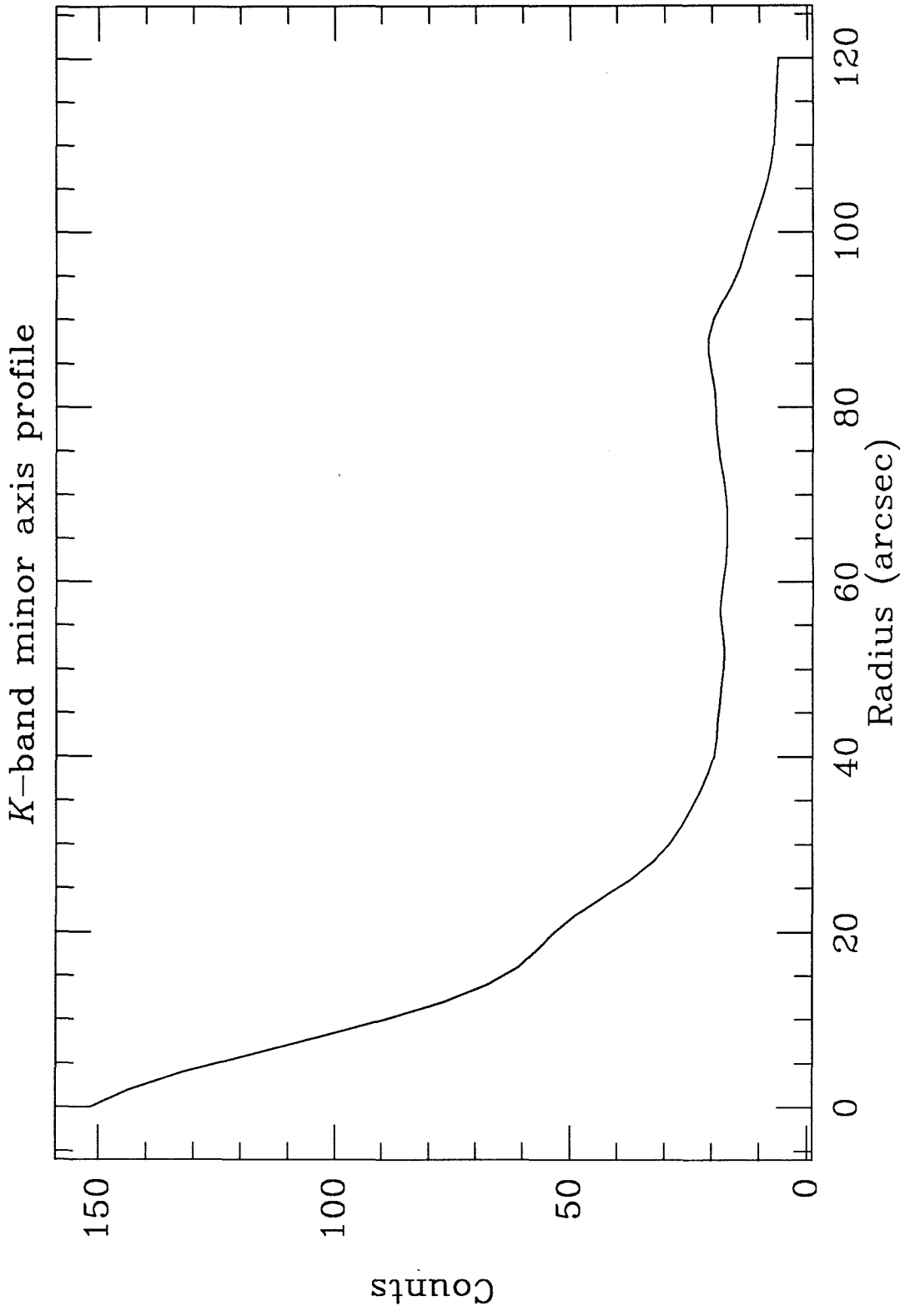
K−band minor axis profile
Counts
0
50
100
150
0
20
40
60
80
100
120
Radius (arcsec)

Figure 3

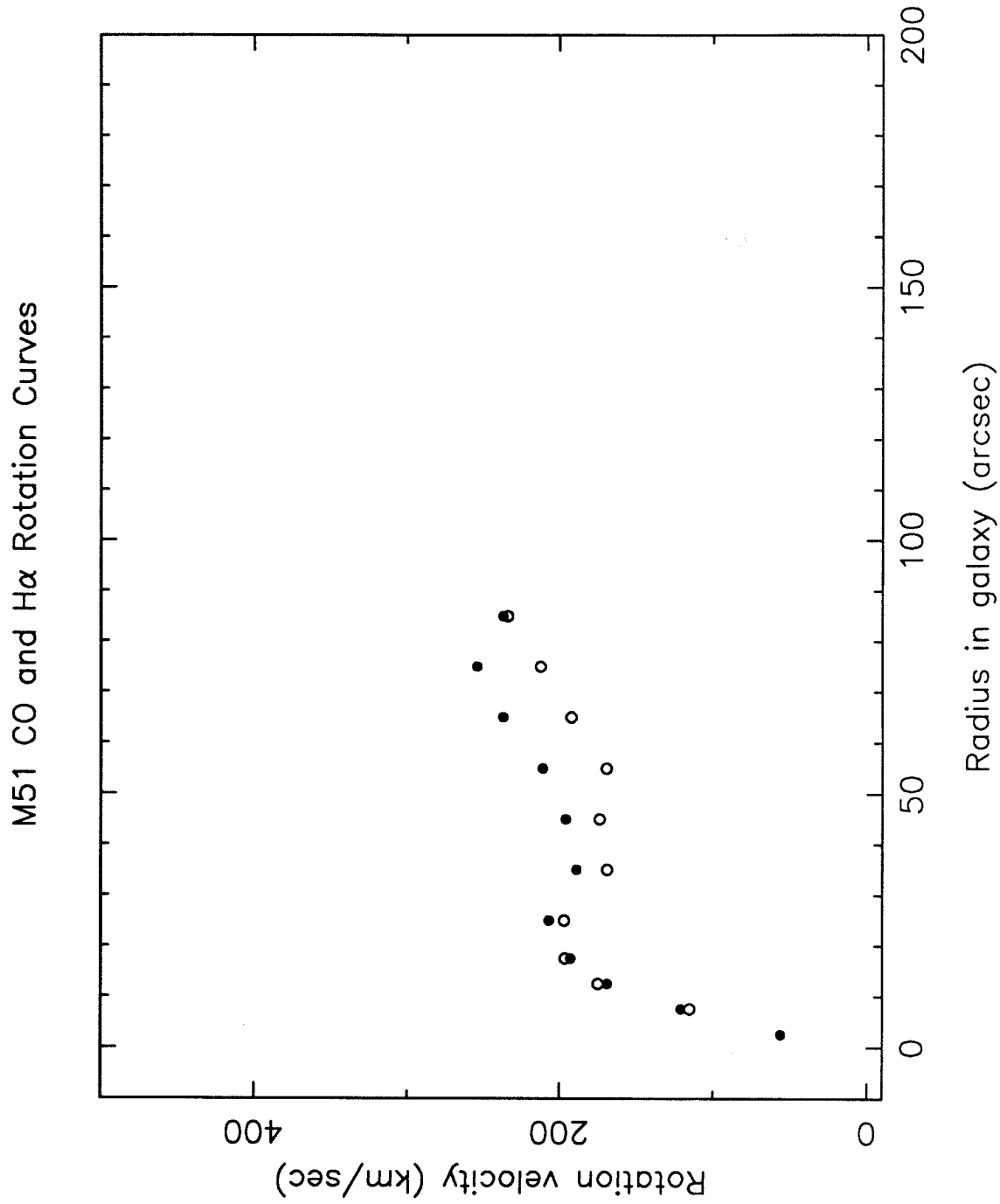
M51 CO and Hα Rotation Curves
Rotation velocity (km/sec)
0
200
400
Radius in galaxy (arcsec)
0
50
100
150
200

Figure 4*a*

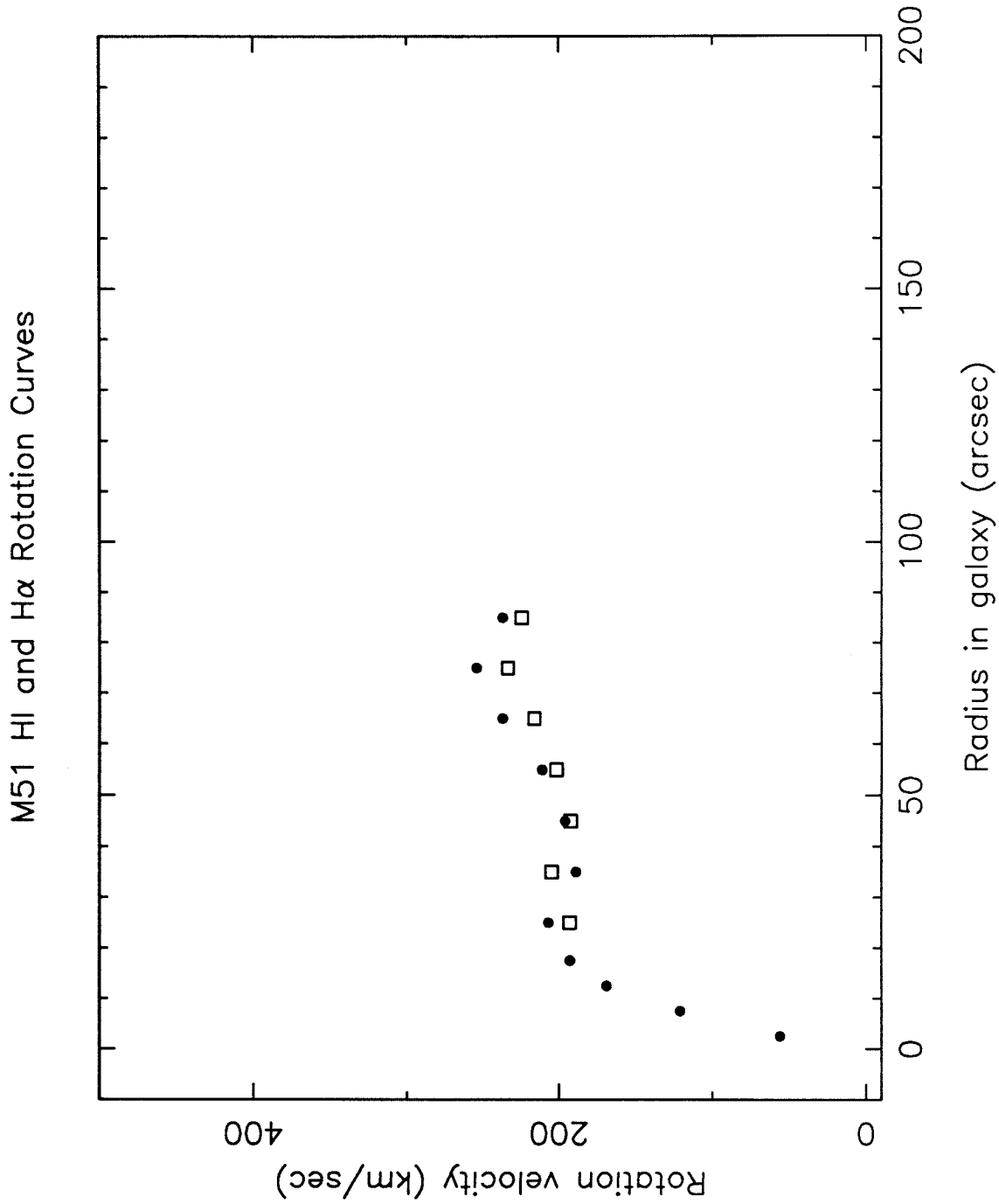
M51 HI and Hα Rotation Curves
Rotation velocity (km/sec)
0
200
400
Radius in galaxy (arcsec)
0
50
100
150
200

Figure 4*b*

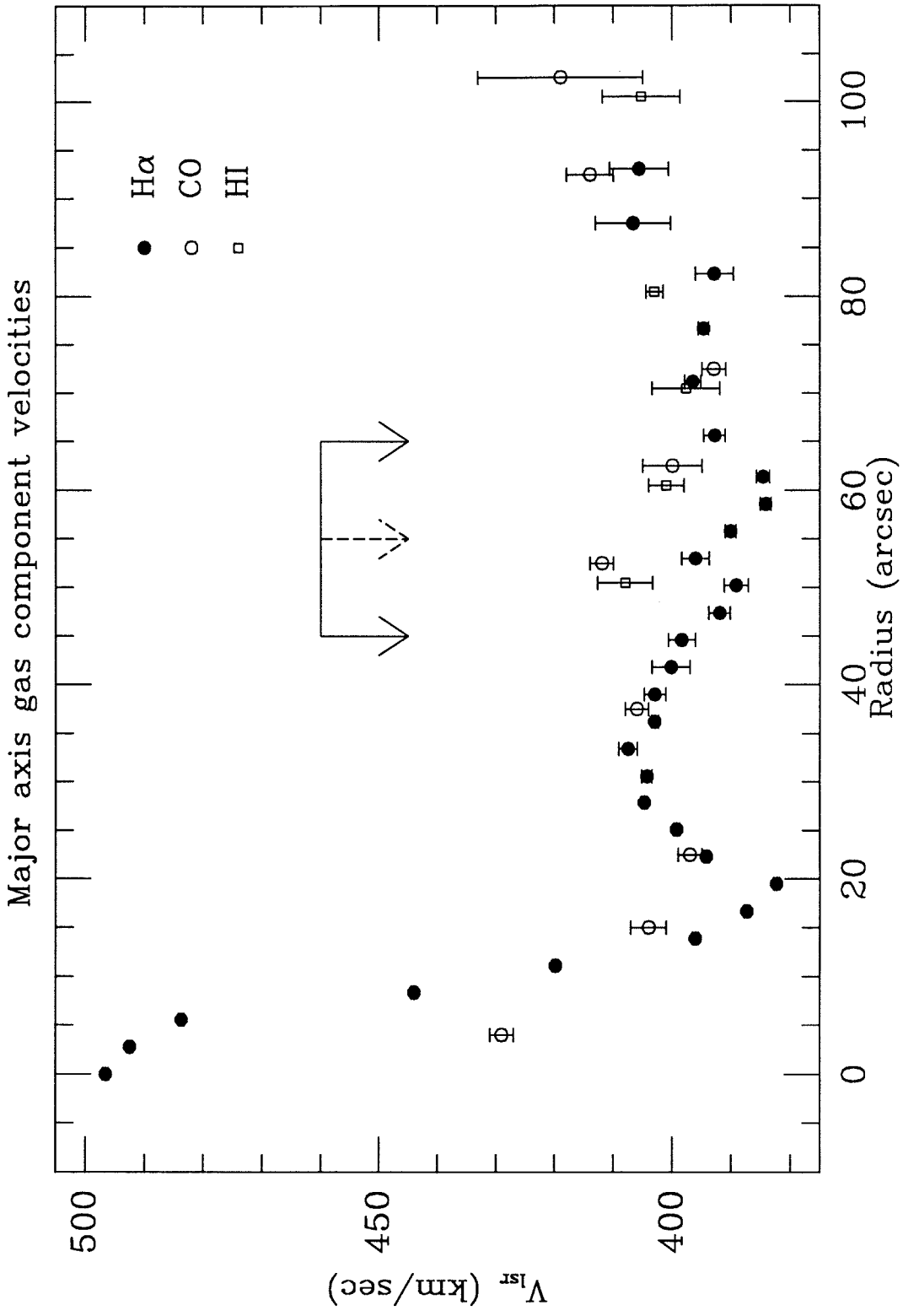
Major axis gas component velocities
Hα
CO
HI
V_{lsr} (km/sec)
500
450
400
0
20
40
60
80
100
Radius (arcsec)

Figure 5

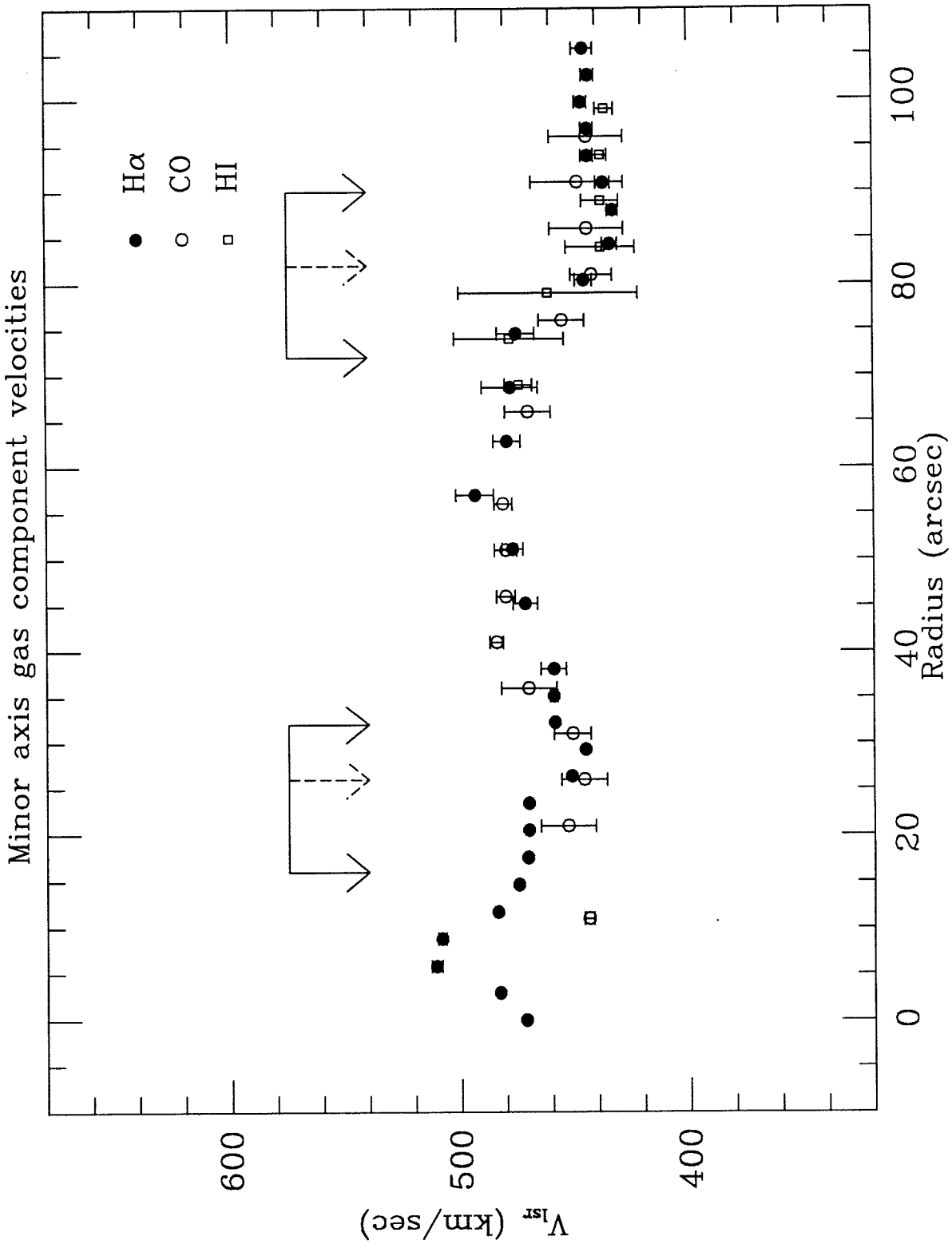
Minor axis gas component velocities
Hα
CO
HI
V_{lsr} (km/sec)
600
500
400
0
20
40
60
80
100
Radius (arcsec)

Figure 6

Simulated profiles of cloud number density and velocity components *vs.* spiral phase.

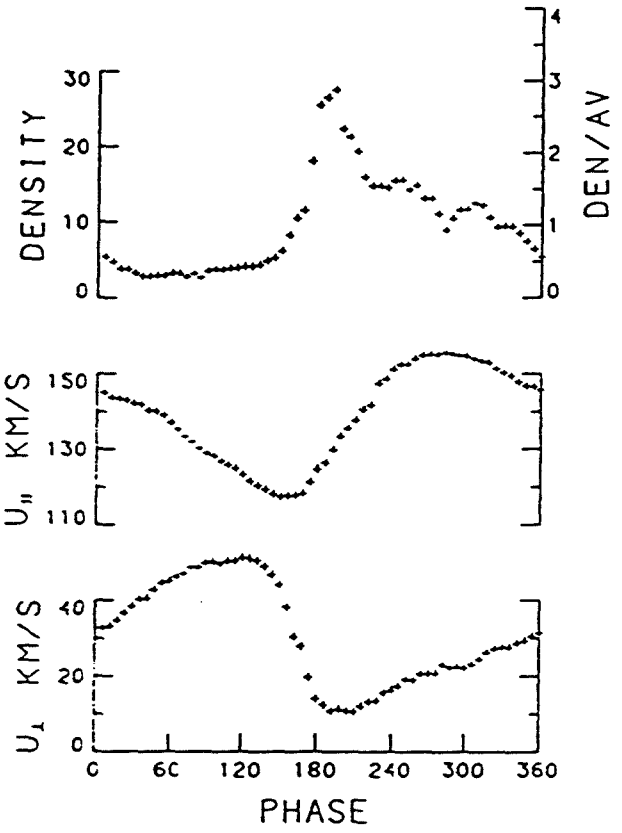

Figure 7

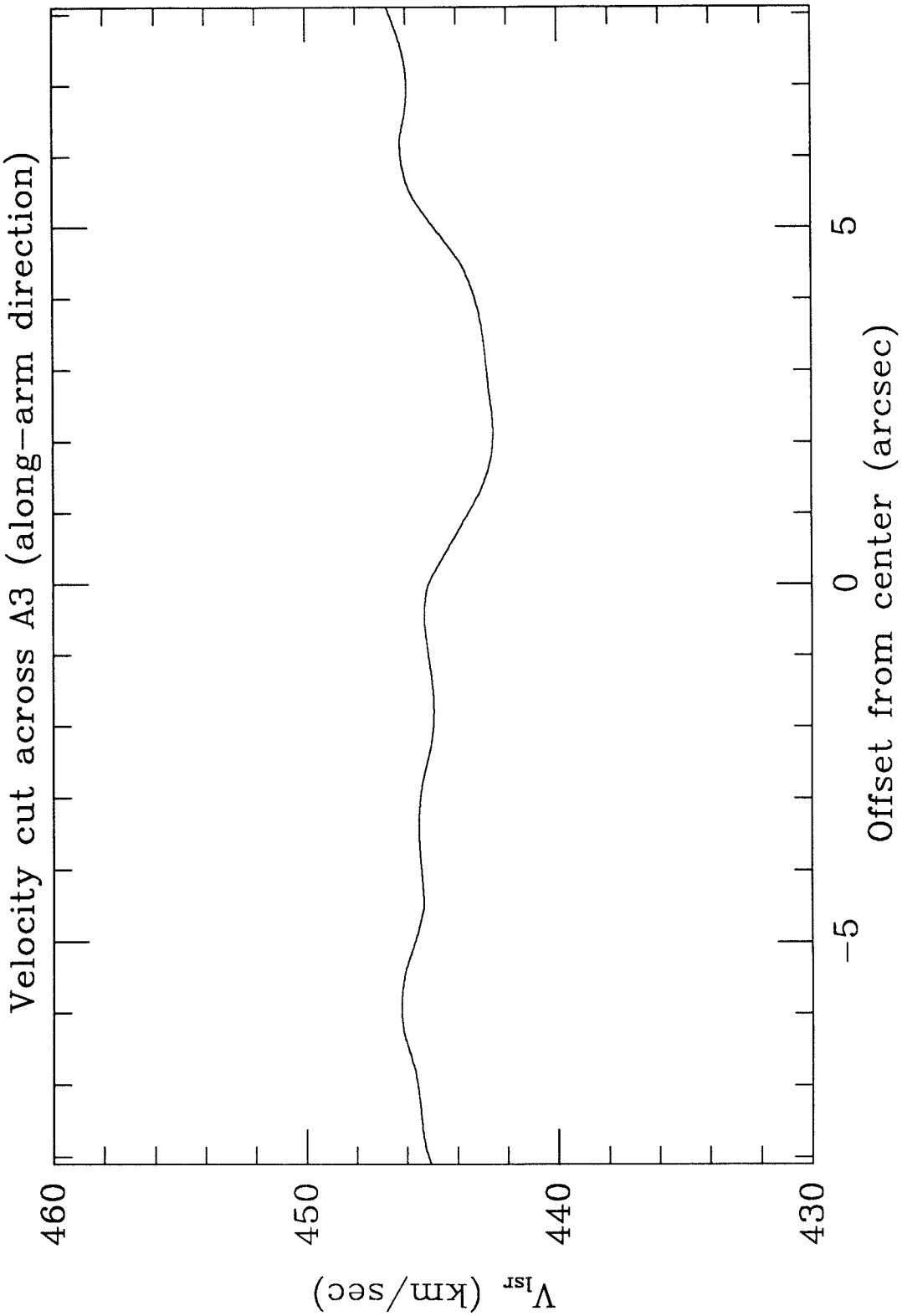
Velocity cut across A3 (along−arm direction)
460
450
440
430
V_{lsr} (km/sec)
−5
0
5
Offset from center (arcsec)

Figure 8